INSTITUTO NACIONAL DE MATEMÁTICA PURA E APLICADA

GAS-SOLID COMBUSTION IN INSULATED POROUS MEDIA

Autor: Grigori Chapiro

Orientador: Prof. Dr. Dan Marchesin

Co-orientadores: Dr. Alexei A. Mailybaev

Prof. Dr. Johannes Bruining

March 30, 2009

Abstract

There is a renewed interest in using combustion for medium viscosity oil recovery. In-situ combustion involves the injection of air, pure oxygen or air enriched with oxygen or nitrogen to enable the combustion of oil and other consecutive reactions within the reservoir formation leading to the release of heat. Heat is conducted ahead of the combustion front, reduces the oil viscosity and leads to in situ distillation (upgrading). Carbon dioxide created during combustion can also assist the recovery by increasing pressure and by mixing with the oil, thus reducing its viscosity and enhancing flow.

To perform computations with the model we need data on the combustion process, which is described in terms of chemical and transport aspects. Data on the combustion process must be converted to a form that can be used in the modeling. We describe in detail how this can be done.

In this work one dimensional gas-solid combustion is studied with the combustion rate described by the first order mass action law combined with the Arrhenius' law. We consider a thermally insulated cylindrical porous rock containing solid fuel. Standard simplifications are made in order to formulate the physical model, for example, the gas thermal capacity is considered small.

The reactive flow of air in porous rock containing solid fuel is governed by a system of balance laws for gas mass, oxygen mass and enthalpy. We are interested in examining the Riemann solutions for the parabolic partial differential equations governing the system, which support a combustion traveling wave. The Riemann problem for adiabatic forward combustion between gas and solid fuel is solved and the combustion wave profile is obtained.

In order to solve the Riemann problem we use an asymptotic expansion to construct a first order approximation of the traveling wave for a given combustion wave speed. Thus we obtain the internal structure of the combustion traveling wave. The results are validated with numerical simulations using a time-step adaptive, hybrid finite difference scheme.

Key words: *porous media, combustion wave, traveling wave, singular perturbation, finite difference scheme.*

i

Resumo

Há um renovado interesse na utilização da técnica de combustão para recuperação de óleo de viscosidade média. A combustão in-situ consiste na injeção de ar, oxigênio puro, ou ar enriquecido com oxigênio ou nitrogênio no reservatório. Assim, gera-se combustão e outras reações químicas, além da libertação de calor. O calor é transportado para a frente da zona de combustão, reduzindo a viscosidade do óleo, produzindo destilação de componentes leves do óleo. O dióxido de carbono criado durante a combustão ajuda na recuperação através do aumento da pressão no reservatório e, ao dissolver-se no óleo, reduzindo sua viscosidade.

Para trabalhar com o modelo precisamos de dados sobre o processo de combustão descrito em termos químicos. É necessário converter estes dados para uma forma que permita seu uso na modelagem do processo. Neste texto descrevemos detalhadamente como isso é feito.

Estudamos um modelo de combustão gás-sólido sob escoamento unidimensional, com a taxa de reação descrita pela lei da ação das massas de primeira ordem, combinada com a lei de Arrhenius. Consideramos um cilindro longo de rocha porosa contendo o combustível sólido; o cilindro é isolado termicamente pelos lados. Para formular o modelo físico, outras simplificações comuns são feitas, por exemplo a capacidade térmica do gás é desconsiderada frente à capacidade térmica da rocha porosa.

O fluxo no meio poroso é governado por um sistema de leis de balanço relativas à massa de combustível, massa de gás, massa de oxigênio e entalpia. Queremos estudar soluções de Riemann para as equações diferenciais parciais que governam o sistema. O problema de Riemann para o problema de combustão gás-sólido foi resolvido neste trabalho e o perfil da onda viajante de combustão foi obtido.

Para resolver o problema Riemann, usamos uma expansão assintótica até a primeira ordem para obter uma aproximação da onda viajante. Assim, obtivemos a estrutura interna da onda de combustão. Os resultados foram validados através da simulação numérica, usando um método de diferenças finitas híbrido adequado às peculiaridades do sistema de equações diferencias parciais.

Palavras chave: *Meios porosos, ondas de combustão, ondas viajantes, perturbação singular, esquemas de diferenças finitas*

Acknowledgements

Many people contributed in the past four years to the completion of this thesis. I am very thankful to everyone and sincerely sorry for all those who are not cited here explicitly.

First of all I would like to thank my advisor Prof. Dan Marchesin for the support during all my time at IMPA, for the research problems he shared with me and for the guiding sentence: "The only useless knowledge is the one you do not possess".

I thank my co-advisor Dr. Alexei Mailybaev for the hours of discussions and for all the valuable advise and suggestions he gave me. I thank my co-advisor Prof. Johannes Bruining for explaining me the Chemistry that I would never understand without him.

I thank Professors André Nachbin, Aparecido J. de Souza, Carlos Tomei and Jorge Zubelli for participating of the thesis committee. Special thanks to Prof. Aparecido J. de Souza for our collaborative work, his suggestions and careful reading of this text. Special thanks go to my friend Gustavo Hime for developing the PDE simulator "NITRO" and for helping me with C programming.

I thank my girlfriend Sara, my parents and my little brother for the patience, support and for accepting that I dedicated much less time to them during the past years than they deserve. I thank my roommates Iuri, Jairo, Villa, Renatão, Flavinho and Silvio.

I thank all my friends and colleagues at IMPA. I would like to thank separately the people I met in the Fluid laboratory, my friends from the Visgraf laboratory, our small volleyball community for our regular Friday sport breaks and the snooker group for the after lunch amusement.

Special thanks to my friends from room 405, Duilio, Jhon, Almir and Maria. In the last years I spent more time with you than in anywhere else. Special thanks also go to my friends Jean, Elias, Geisa, Dimas, Emilio, Ives and Julio Daniel for our long conversations about subjects far from mathematics.

I would like to thank all my professors at IMPA for everything I learned during these years and IMPA's staff for the excellent and incomparable support.

Finally, I thank the CAPES and ANP-PRH32 for the financial support during these years.

Contents

List of Figures

Chapter 1

Introduction

Frequent high oil prices have renewed interest in heavy oil recovery techniques such as in situ combustion (ISC). This technique involves the injection of pure oxygen or air, or air enriched with oxygen or nitrogen to enable combustion of oil and other consecutive reactions within the reservoir formation leading to the release of heat. Heat is conducted ahead of the combustion front, reduces the oil viscosity and leads to in situ distillation (upgrading). Carbon dioxide created during combustion can also assist the recovery by increasing pressure and by mixing with the oil reducing its viscosity and enhancing flow, see [9, 37].

Another thermal recovery technique is steam injection. It is of interest to compare the advantages and disadvantages of these two thermal recovery techniques. Steam is formed by passing treated water through a boiler system which comprises a considerable energy cost. ISC avoids these heat-related costs, but requires compressors for the injected air. ISC has other benefits relative to steam injection. For example, steam generation produces CO_2 at the surface, representing a significant environmental impact, and heat is lost during its transport to the formation. ISC produces CO_2 downhole, which will be partially sequestered in the formation, see [37].

The primary limitation of ISC is that the combustion front is hard to control. This difficulty supports the research interest in this subject in different areas such as Engineering, Physics, Computer Science and Mathematics.

We summarize the literature on chemical processes occurring during ISC. We use the schematic division of the ISC processes shown in Figure 1.1, see [24]. Following upstream the flow (right to left or from the production to the injection well) we can separate the light hydrocarbons (HC) zone, the steam zone, the cracking zone, the coke formation zone and the

coke combustion zone.
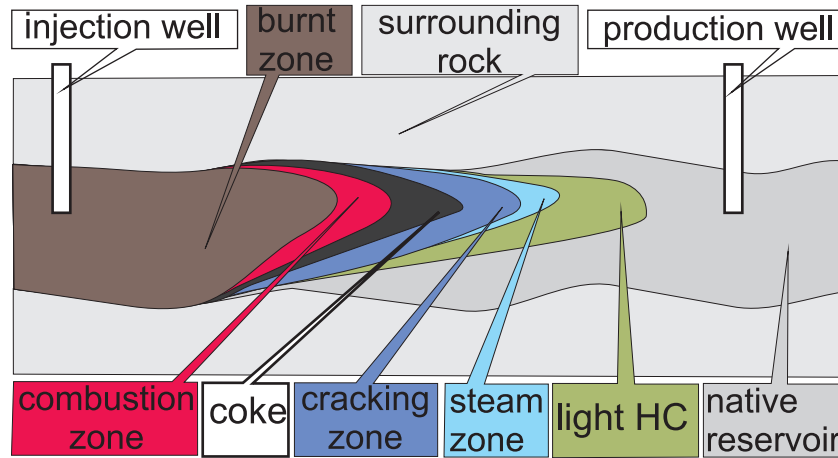
Figure 1.1: Schematic representation of ISC process.

According to [1] there are three overlapping processes caused by temperature elevation due to heat transfer downstream the reaction zone. The first process is distillation (evaporation) of light oil components, which occurs at lower temperatures. Next, we separate the "visbreaking" stage that occurs at mild temperatures and breaks the initial oil into low volatile components and a "visbroken" oil (with smaller viscosity and specific gravity). Finally, the severe cracking (coking) reaction transforms the visbroken oil into coke and some lighter components.

Condensation of all light oil that has been produced elsewhere occurs inside the light hydrocarbon zone. In some cases, oxygen can break through the coke zone and come into contact with the light hydrocarbons where the reaction is described by the "Low Temperature Oxidation" (LTO) mechanism, see [27].

In addition to initial water in the reservoir, which evaporates due to high temperature, steam is formed from the combustion products. This water condenses inside the steam zone downstream of the combustion process. Heat released during condensation elevates the reservoir temperature and increases the evaporation of light oil components.

Continuing upstream we find the cracking zone, where visbreaking and coking stages [1] occur and the coke zone that has only formation of coke, which is consumed during the combustion reaction. The processes occurring inside the cracking zone influence the distribution of coke inside the reservoir. This distribution is related to surface tensions between rock, viscous oil and gas coexisting before the combustion. Because of the high temperature, inside the coke and cracking zones there is no significant quantity of water and light components of oil.

Inside the combustion zone the residual coke reacts with the injected oxygen. The microporous structure of coke and related parameters, such as reactive area of coke particles and transport of oxygen into the pores, are important to describe this process, see [8] and [35]. There is abundant literature, for example [22, 44], focusing on the reaction kinematics for general materials containing carbon. However, the reaction rates for general carbon containing materials can vary by up to some orders of magnitude. The situation for petroleum coke is more clear. We explain in detail the reaction happening inside this zone in Chapter 8. The combustion zone is typically tens of feet wide and the temperature of the combustion front is usually around 430-540^oC.

In this work, we model ISC in a $1D$ configuration. There are reasons to do so, besides simplicity. One of them is that due to gravitation the oxygen tends to occupy the top part of the reservoir, thus we can consider a thin layer containing most of the oxygen. To complete the model we can take into account heat losses to other layers of the porous media. These losses have no significant effect on the combustion zone because it is thin and the reaction is fast, but they will influence the thermal wave that trails the combustion wave.

In this text we study only the processes happening inside the combustion zone. We assume that the porous medium is filled with petroleum coke and the only chemical reaction occurring is the coke oxidation (combustion).

The combustion wave at the reservoir side can be controlled by the lack of oxygen or by low temperature. Most of the literature studies the phenomenon controlled by low temperature, which is more common in practice. This case is not so amenable to analysis as oxygen controlled case. The techniques used to study the combustion wave controlled by low temperature are very different from presented here. For example, in [11] an approximate solution was obtained, it is a slowly varying transient wave. In this text we address the fuel and oxygen controlled case.

For the model described in Chapter 2 there are two possible types of motion for the combustion wave. In co-flow combustion the ignition takes place at the injection end of the cylinder and propagates in the same direction as the injected gas. The analysis of this situation is made in Chapter 4. From the Engineering point of view this method is more practical, see Figure 1.1.

The second possibility is counter-flow combustion, for which the ignition occurs on the production end of the cylinder and the combustion wave moves in the opposite direction to the injected gas. The advantage of this technique is temperature increase near the production well, where it can increase the recovery. We do not study this technique here, however one can find

details in [21, 40].

This work is organized as follows. In Chapter 2 we introduce two physical models describing the ISC process. First we present the physical model in terms of mass balances [2] and explain its limitations. Next, we formalize a model in terms of molar balance, which is better in many respects. The equations for both models have the same dimensionless form.

In Chapter 3 we apply the geometrical singular perturbation method developed in [31] in order to obtain an approximation of the heteroclinic orbit joining two equilibria of certain ordinary differential equations that describe the profile of the combustion wave. The case of our interest corresponds to a system of ODEs where one of the flux functions is much smaller than the remaining ones.

In Chapter 4 we review briefly the literature on combustion waves in porous media. The Riemann problem for the system describing the physical model with reaction rate given by the Arrhenius' law is formulated. Next, we use the singular perturbation method developed in Chapter 3 in order to obtain the combustion wave profile in the form of an asymptotic series expansion. We obtain the zero-order approximation and validate it by analyzing the first order correction. In this chapter we present strong evidence of the existence of such traveling wave solution.

In Chapter 5 we give a physical interpretation to the zero-order approximation obtained in Chapter 4. We present a simplification of the physical model [2]. In this simplification, all diffusive and conductive terms are neglected. We obtain the exact traveling wave solution for the combustion wave of this non-diffusive system. It turns out that the combustion wave profile of such system coincides with the zero-order approximation of the diffusive model obtained in Chapter 4.

In Chapter 6 we show that the the classical Crank-Nicolson scheme is not indicated to simulate the physical model [2]. We develop a hybrid finite difference scheme to circumvent this difficulty and simulate this system numerically. The numerical results confirm the combustion wave profile obtained in Chapter 4 by means of the singular perturbation technique.

In Chapter 7 we introduce a simpler model for the ISC process. This model possesses some properties of the physical model [2]. For example, the wave sequence in the Riemann solution possesses three contact waves for both models. However, it is more amenable to analysis and it can be simulated using the classical Crank-Nicolson finite difference scheme. We obtain the combustion traveling wave profile for this simpler model using the singular perturbation technique and validate it by numerical simulations. Next we present some heuristic calculations

for this simpler model and discuss the stability of the combustion wave obtained using the singular perturbation method.

Finally, in Chapter 8 one can find an introduction to chemistry of coke combustion with a brief literature review and a description of the reaction kinetics.

Chapter 2

Physical formulation

In this chapter we formulate physical models used to study combustion fronts in in-situ combustion and compare them to models in the literature. First of all we restrict our efforts to one dimensional models. Some works formulate mathematical theory on the interaction between the combustion zone and other zones as represented in Figure 1.1. For example, in [11] the interaction of combustion and steam zone is discussed. However this work ignores the existence of the cracking zone and the chemical processes that occur. In [12] the interaction of combustion and cracking zones is considered. Here we will discuss only the behavior of the combustion zone.

Let us introduce certain physical hypotheses common to all models discussed in this text. We consider a thin cylindrical tube filled with porous medium containing coke, schematically represented on Figure 2.1. As we are interested in the combustion zone, it is assumed that there is no liquid phase in the porous medium and that the only chemical reaction is the oxidation of coke.

In formulating the conservation equations we make the following assumptions: the pore space and the solid matrix are in thermal equilibrium so that a one-temperature model is used for the energy balance; heat transfer by radiation, energy source terms due to pressure increase, and work from surface and body forces are all negligible; the ideal gas law is the equation of state for the gas phase; thermodynamic and transport properties, such as conductivity, diffusivity, heat capacity of the solid, heat of reaction, etc., all remain constant. We also neglect heat loss to the surrounding rock formation. We assume that gas heat capacity is negligible with respect to the rock heat capacity. The heat loss will be taken to be zero as we study only the adiabatic case. We assume that pressure changes within any wave are negligible compared to
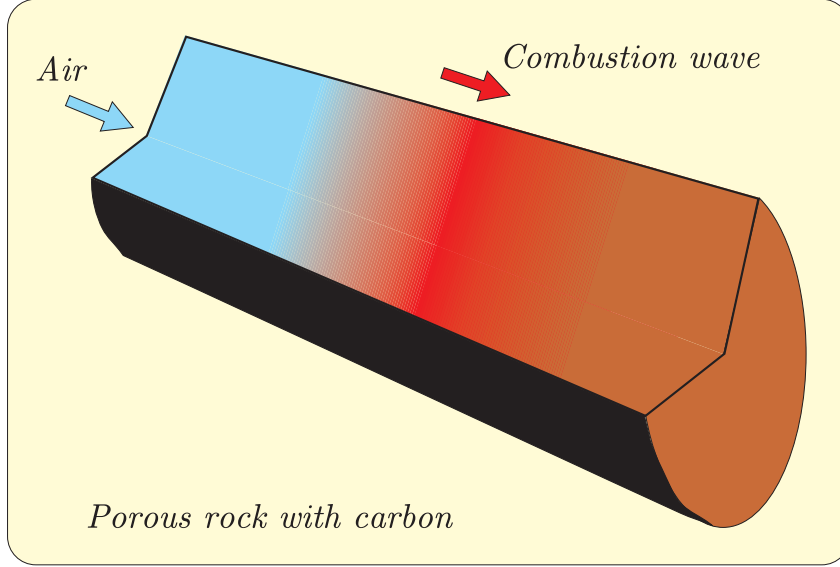
Figure 2.1: Schematic representation of the one-dimensional model for ISC.

the pressure drop across the system, so that in the ideal gas law and in other physical properties the pressure can be approximated by a constant. Next we introduce and discuss some models used in this work.

2.1 Mathematical model

The original model, which is formulated in terms of mass conservation, can be found in [2]. Here we present the simplified version of this model used in [46]. We assume that air is injected at the leftmost part of a porous rock cylinder containing solid fuel, so that all wave propagation is one dimensional. Balance equations are written for the total energy, the total gas mass, the oxygen mass and the fuel mass. For the latter, we define the fuel density per total volume ρ_f and introduce the extent of conversion depth, $\eta(\tilde{x}, \tilde{t}) = 1 - \rho_f(\tilde{x}, \tilde{t})/\rho_f^o$ (ρ_f^o is the initial fuel concentration), such that $\eta = 0$ corresponds to complete availability of fuel (denoted by superscript o) and $\eta = 1$ to the complete lack of fuel (the latter may occur because the fuel was never present or because it was completely consumed). The primary dependent variables are the temperature, $\tilde{T}(\tilde{x}, \tilde{t})$, the oxygen concentration in terms of mass fraction, $\tilde{Y}(\tilde{x}, \tilde{t})$ and the fuel conversion depth $\eta(\tilde{x}, \tilde{t})$. The gas density $\rho_g(\tilde{T}, \tilde{p})$ is expressed by the ideal gas equation of state in terms of temperature, gas composition and total gas pressure $\tilde{p}(\tilde{x}, \tilde{t})$.

The dimensional form (indicated by the superscript tilde) of the energy balance, the oxygen mass balance, the gaseous phase mass balance and the combustion kinetics equations are:

$$(1-\phi)\frac{\partial(c_s\rho_s\tilde{T})}{\partial\tilde{t}} + \frac{\partial(c_g\rho_g\tilde{v}\tilde{T})}{\partial\tilde{x}} = \tilde{\lambda}\frac{\partial^2\tilde{T}}{\partial\tilde{x}^2} + Q\rho_f^o W, \tag{2.1}$$

$$\phi\frac{\partial(\rho_g\tilde{Y})}{\partial\tilde{t}} + \frac{\partial(\rho_g\tilde{v}\tilde{Y})}{\partial\tilde{x}} = D_M\frac{\partial}{\partial\tilde{x}}\left(\rho_g\frac{\partial\tilde{Y}}{\partial\tilde{x}}\right) - \tilde{\mu}\rho_f^o W, \tag{2.2}$$

$$\phi\frac{\partial(\rho_g)}{\partial\tilde{t}} + \frac{\partial(\rho_g\tilde{v})}{\partial\tilde{x}} = \tilde{\mu}_g\rho_f^o W, \tag{2.3}$$

$$\frac{\partial\eta}{\partial\tilde{t}} = W, \tag{2.4}$$

where W is the reaction rate. The four equations (2.1)-(2.4) correspond to the three primary unknowns $\tilde{T}$, $\tilde{Y}$, η and the secondary unknown $\tilde{v}$, which is the volumetric flow rate of the gas phase. In the above, c_g, c_s denote the average specific heat capacity of gas or solid at constant pressure, ρ_g, ρ_s are the volumetric densities of gas or solid, $\tilde{\lambda}$ is the effective thermal conductivity, Q is the heat released due to reaction (per unit mass of solid). Other constants are explained in Table 2.1. Changes in the porosity ϕ are considered to be negligible so that ϕ is constant. D_M is an effective diffusion coefficient in the gas phase ($D_M = \phi D$, where D is the molecular diffusion coefficient), while $\tilde{\mu} = \tilde{\gamma}M_o/M_f$ and $\tilde{\mu}_{gp} = \tilde{\gamma}_{gp}M_{gp}/M_f$ are mass-weighted stoichiometric coefficients for oxygen and for combustion gaseous products, respectively. M_o, M_f and M_{gp} are the molecular weight of oxygen, fuel and gaseous products, respectively. The net gas mass production is determined from $\tilde{\mu}_g = \tilde{\mu}_{gp} - \tilde{\mu}$, so that positive or negative sign for $\tilde{\mu}_g$ correspond to net gaseous phase mass production or consumption, respectively. We will assume $\tilde{\mu}_g > 0$. For the rate of reaction, we use the first order law of mass action and Arrhenius' Law:

$$W = k_c e^{-E/R\tilde{T}}\tilde{Y}(1-\eta), \tag{2.5}$$

with activation energy E and pre-exponential factor k_c given by:

$$k_c = k_0\frac{a_s p_0}{R\tilde{T}_0}, \tag{2.6}$$

where a_s is the specific surface area of the coke particles (see Table 2.1 for the typical values of k_0, a_s, p_0, R and $\tilde{T}_0$), more details on the Chemistry of coke combustion are found in Chapter 8.

We use the ideal gas equation of state in terms of density:

$$\tilde{p}M_g = \rho_g R\tilde{T}, \tag{2.7}$$

8

Table 2.1: Typical values of dimensional parameters. *Source:* [2].

Physical quantity	Symbol	Value	Unit
heat release due to reaction	Q	39542	kJ/kg
activation energy	E	$7.35 \cdot 10^4$	kJ/kmole
universal gas constant	R	8.314	kJ/kmole-K
pre-exponential factor[2]	k_o	0.00224	kW-m/Pa-kmole
initial reservoir temperature	$\tilde{T}_o$	373.15	K
initial total gas pressure[2] (1 atm)	p_o	101325	Pa
inlet oxygen mass concentration	$\tilde{Y}^i$	1.0	(kg/kg)
effective molecular diffusion coefficient	D_M	$2.014 \cdot 10^{-6}$	m^2/s
effective thermal conductivity	$\tilde{\lambda}$	$8.654 \cdot 10^{-4}$	kW/m-K
volumetric heat capacity of the gas	$c_g \rho_g^i$	1.2339	kJ/m^3-K
initial fuel concentration	ρ_f^o	19.2182	kg/m^3
volumetric heat capacity of the matrix	$(1-\phi)c_s\rho_s$	$2.012 \cdot 10^3$	kJ/m^3-K
mass of oxygen/unit mass of fuel	$\tilde{\mu}$	3.018	(kg/kg)
net mass production of gas/unit mass of fuel	$\tilde{\mu}_g$	1.000	(kg/kg)
molecular weight of gaseous products[1]	M_g	0.044	kg/mole
molecular weight of coke	M_f	0.235	kg/mole
gaseous products density[1]	ρ_g^i	1.98	kg/m^3
coke particles specific surface area	a_s	$1.41 \cdot 10^5$	m^2/m^3
porosity of the medium	ϕ	0.3	m^3/m^3

where R is the universal gas constant, while M_g is the effective molecular weight of the gas phase. Notice that M_g and ρ_g depend on the molecular weight of the gas, i.e. $M_g = M_g(Y)$ and $\rho_g = \rho_g(Y)$ as the only reaction occurring is the oxidation of coke. In the models analyzed in Chapters 4, 5 and 7 we neglect the effect of changes in these variables resulting from composition changes due to the reaction, and we approximate M_g by constant so that ρ_g does not depend on Y. Notice that if we replace the system (2.1)-(2.4) in terms of molar densities instead of mass densities the equation (2.7) becomes exact. We discuss it in detail in Section 2.3. All the dimensional constants used in this section are given in Table 2.1. In [2] the injected gas was pure oxygen $\tilde{Y}^i = 1$.

---

[1]These values where taken for CO_2 gas at 1 *atm* pressure.
[2]In [2] the pressure was given in [*atm*], the value of k_0 was 227 [$kW \cdot m/atm \cdot kmole$].

2.2 The nondimensionalization

The nondimensionalization of the problem is performed as follows. One introduces characteristic value for the speed v^*, from which we define the reference length[1] $l^* = \alpha_s/v^*$ and time $t^* = l^*/v^*$. Following [2], we define scaled effective thermal diffusivity $\alpha_s = \tilde{\lambda}/((1 - \phi)c_s\rho_s)$ $[m^2/s]$. These quantities are defined in such way that the coefficient of the diffusion term in the energy conservation equation is one. In short, the nondimensional variables are:

$$v = \frac{\tilde{v}}{v^*}; \quad \theta = \frac{\tilde{T}}{\tilde{T}_0}; \quad t = \frac{\tilde{t}}{t^*} = \frac{\tilde{t}v^{*2}}{\alpha_s}; \quad x = \frac{\tilde{x}}{l^*} = \frac{\tilde{x}v^*}{\alpha_s}; \quad Y = \frac{\tilde{Y}}{\tilde{Y}^i}; \quad \eta = 1 - \frac{\rho_f}{\rho_f^0}; \quad \rho = \frac{\rho_g}{\rho_g^i}. \tag{2.8}$$

where $\tilde{T}_0$ is the prevailing reservoir temperature, $\tilde{Y}^i$ is the injected oxygen fraction in the total gas mass, ρ_f^0 is the initial fuel concentration and ρ_g^i is the produced gas concentration. The variables with tilde are physical: $\tilde{T}$ is temperature in [K], $\tilde{Y}$ is oxygen fraction in the total gas and $\tilde{v}$, $\tilde{t}$, $\tilde{x}$ are the gas speed [m/s], time [s] and length [m]. Substituting (2.8) into (2.1)-(2.4) with some simple manipulations we obtain:

$$\frac{\partial \theta}{\partial t} + \frac{c_g\rho_g^i}{(1 - \phi)c_s\rho_s}\frac{\partial(\rho v\theta)}{\partial x} = \frac{\partial^2\theta}{\partial x^2} + \frac{Q\rho_f^o}{(1 - \phi)c_s\rho_s\tilde{T}_0}t^*W, \tag{2.9}$$

$$\phi\frac{\partial(Y\rho)}{\partial t} + \frac{\partial(\rho vY)}{\partial x} = \frac{D_Mt^*}{(l^*)^2}\frac{\partial}{\partial x}\left(\rho\frac{\partial Y}{\partial x}\right) - \frac{\tilde{\mu}\rho_f^o}{\rho_g^i\tilde{Y}_i}t^*W, \tag{2.10}$$

$$\phi\frac{\partial\rho}{\partial t} + \frac{\partial(\rho v)}{\partial x} = \frac{\tilde{\mu}_g\rho_f^o}{\rho_g^i}t^*W, \tag{2.11}$$

$$\frac{\partial\eta}{\partial t} = t^*W, \tag{2.12}$$

Using (2.8) with (2.5) we obtain the nondimensional reaction rate Φ:

$$\Phi = t^*W = k_c\tilde{Y}_it^* Y(1 - \eta)e^{-(E/R\tilde{T}_0)/\theta}. \tag{2.13}$$

Finally, applying (2.8) for T and ρ_g in (2.7), where we approximate the pressure by a constant $(p_0 = 1\,[atm])$, we obtain the dimensionless ideal gas equation:

$$\rho\theta = \frac{p_0M_g}{R\rho_g^i\tilde{T}_0}. \tag{2.14}$$

We collect all the nondimensional constants of (2.9)-(2.14), obtaining:

$$a = \frac{c_g\rho_g^i}{(1 - \phi)c_s\rho_s}, \quad q = \frac{Q\rho_f^o}{(1 - \phi)c_s\rho_s\tilde{T}_0}, \quad L_e = \frac{(l^*)^2}{D_Mt^*} = \frac{\alpha_s}{D_M}, \quad \mu = \frac{\tilde{\mu}\rho_f^o}{\rho_g^i\tilde{Y}_i}, \quad \mu_g = \frac{\tilde{\mu}_g\rho_f^o}{\rho_g^i},$$

$$b = p_0M_g/(R\rho_g^i\tilde{T}_0), \quad \gamma = E/R\tilde{T}_0, \quad \alpha = k_ct^*\tilde{Y}_i. \tag{2.15}$$

---

[1]Notice that the name characteristic length will be used later to denote the length of the combustion wave.

Table 2.2: Values of dimensionless parameters given in (2.15) corresponding to Table 2.1.

Physical quantity	Symbol	Value
Volumetric heat capacity ratio of the filtrating gas	a	$6.13 \cdot 10^{-4}$
Heat transfered to porous medium due to the reaction	q	1.012
Lewis number (ratio of thermal and molecular diffusion)	L_e	0.21
Stoichiometric coefficient for oxygen	μ	29.29
Net stoichiometric coefficient for gas production	μ_g	9.71
Scaled ideal gas constant	b	0.73
Arrhenius number (dimensionless activation energy)	γ	23.69
Reaction coefficient[1]	α	828.15

The values of these quantities are shown in Table 2.2; they are calculated using Table 2.1. Using (2.15) we rewrite (2.1)-(2.4) and (2.7) in nondimensional form:

$$\frac{\partial \theta}{\partial t} + \frac{\partial (a\rho v \theta)}{\partial x} = \frac{\partial^2 \theta}{\partial x^2} + q\Phi, \tag{2.16}$$

$$\phi \frac{\partial (Y\rho)}{\partial t} + \frac{\partial (\rho v Y)}{\partial x} = \frac{1}{L_e} \frac{\partial}{\partial x}\left(\rho \frac{\partial Y}{\partial x}\right) - \mu\Phi, \tag{2.17}$$

$$\phi \frac{\partial \rho}{\partial t} + \frac{\partial (\rho v)}{\partial x} = \mu_g \Phi, \tag{2.18}$$

$$\frac{\partial \eta}{\partial t} = \Phi, \tag{2.19}$$

$$\rho\theta = b. \tag{2.20}$$

The equations (2.16)-(2.18) were obtained in [2] exactly in this form. Equation (2.19) was written in [2] in a similar form but equation (2.20) was written in [46] with b replaced incorrectly by 1. The nondimensional reaction rate $\Phi(\theta, Y, \eta)$ is:

$$\Phi = \alpha Y (1 - \eta) e^{-\frac{\gamma}{\theta}}. \tag{2.21}$$

The nomenclature and typical values of the nondimensional parameters given in (2.15) are found in Table 2.2.

The basic dependent variables are the temperature, $\theta(x,t)$, the oxygen mass concentration $Y(x,t)$ and the fuel conversion depth $\eta(x,t)$ (recall that $\eta = 0$ corresponds to complete avail-

---

[1]This reaction coefficient corresponds to injection gas speed $v^i = 200 \ m/day$. In [2] injection speeds in the range $0 < v^i < 500 \ m/day$ are considered.

ability of fuel and $\eta = 1$ to the complete lack of fuel). Eq. (2.20) allows expressing the gas density ρ in terms of temperature. The Darcy velocity v is the volumetric flow of gas per unit area. The physical domain of the variables (θ, Y, η, v) is given by:

$$\theta \geq 0, \quad 0 \leq Y \leq 1, \quad 0 \leq \eta \leq 1, \quad v > 0. \tag{2.22}$$

In order to find the time evolution of the system (2.16)-(2.21) we extract ρ from (2.20) and substitute it into (2.16)-(2.19), obtaining:

$$\frac{\partial \theta}{\partial t} + ab\frac{\partial v}{\partial x} = \frac{\partial^2 \theta}{\partial x^2} + q\Phi, \tag{2.23}$$

$$\phi b\frac{\partial (Y/\theta)}{\partial t} + b\frac{\partial (vY/\theta)}{\partial x} = \frac{b}{L_e}\frac{\partial}{\partial x}\left(\frac{1}{\theta}\frac{\partial Y}{\partial x}\right) - \mu\Phi, \tag{2.24}$$

$$\phi b\frac{\partial}{\partial t}\frac{1}{\theta} + b\frac{\partial (v/\theta)}{\partial x} = \mu_g\Phi, \tag{2.25}$$

$$\frac{\partial \eta}{\partial t} = \Phi. \tag{2.26}$$

Remark 2.1 (Extra difficulty) *One notices that the system (2.23)-(2.26) presents an extra peculiarity. The variable v does not appear inside any derivative in time. It follows that when we are solving a Cauchy problem for this system, we cannot define the value for the variable v except at a single point for $t = 0$.*

2.3   Improving the model

As we explained before, the equation (2.20) (as it is obtained from (2.7)) is only approximately valid because during the chemical reaction the molar densities of different gas components vary. When the reaction can be regarded as being $C + O_2 \rightarrow CO_2$, the total number of moles in the gas does not change during the reaction. Thus the ideal gas equation of state for the mixture in terms of gas molar density ρ_g^m now is exact:

$$\tilde{p} = \rho_g^m R\tilde{T}. \tag{2.27}$$

Notice that stoichiometric coefficients corresponding to moles of generated gas and to moles of consumed oxygen are equal to one, thus there is no net molar generation of gas during the reaction. We rewrite the system (2.1)-(2.4) in terms of molar densities of gas $\rho_g^m = \rho_g M_g^{-1}$ and of fuel $\rho_f^m = \rho_f^o M_f^{-1}$:

$$(1 - \phi)\frac{\partial (c_s\rho_s\tilde{T})}{\partial \tilde{t}} + \frac{\partial (\tilde{c}_g\rho_g^m\tilde{v}\tilde{T})}{\partial \tilde{x}} = \tilde{\lambda}\frac{\partial^2 \tilde{T}}{\partial \tilde{x}^2} + Q\rho_f^m M_f W, \quad \left[\frac{J}{m^3 s}\right], \tag{2.28}$$

$$\phi \frac{\partial(\rho_g^m \tilde{Y})}{\partial \tilde{t}} + \frac{\partial(\rho_g^m \tilde{v} \tilde{Y})}{\partial \tilde{x}} = D_M \frac{\partial}{\partial \tilde{x}} \left(\rho_g^m \frac{\partial \tilde{Y}}{\partial \tilde{x}} \right) - \hat{\mu} \rho_f^m W, \quad \left[\frac{mole}{m^3 s} \right], \tag{2.29}$$

$$\phi \frac{\partial \rho_g^m}{\partial \tilde{t}} + \frac{\partial(\rho_g^m M_g \tilde{v})}{\partial \tilde{x}} = 0, \quad \left[\frac{mole}{m^3 s} \right], \tag{2.30}$$

$$\frac{\partial \eta}{\partial \tilde{t}} = W, \quad \left[\frac{1}{s} \right], \tag{2.31}$$

where we have introduced the stoichiometric coefficient $\hat{\mu} = \tilde{\mu} M_f / M_g$ and specific heat capacity of gas $\tilde{c}_g = c_g M_g$ in terms of moles. The reaction rate is governed by the Arrhenius' law (2.5). One has to notice that when we used the equation (2.20) to eliminate the variable ρ from the system (2.16)-(2.19) to obtain system (2.23)-(2.26) we introduced an error due to the fact that the equation (2.7) in terms of mass is only an approximation of the equation of state for mixtures of ideal gases. This error is avoided by using the exact ideal gas law in terms of molar density (2.27).

The term $\tilde{c}_g \rho_g^m$ in (2.28) is the average heat capacity of the gases in the mixture at constant pressure. As O_2 and CO_2 are linear molecules they have the same number of degrees of freedom and their molar heat capacity (at constant pressure) is practically the same. Therefore, as O_2 reacts and is replaced by the same number of moles of CO_2, the average molar heat capacity of the mixture stays (practically) constant. That was not the case in (2.1) where the specific heat of the mixture was written in terms of mass rather than in terms of moles.

As for the physical mass conservation model (2.1)-(2.5) we nondimensionalize (2.27)-(2.31) using (2.8), obtaining the system in dimensionless form (2.16)-(2.20) with dimensionless constants given by (2.15) except that $\mu_g = 0$.

There is no formal differences between the approximate physical model written in terms of mass densities or the exact model written in terms of molar densities.

2.4   Other values of dimensionless parameters

In [46] the values for dimensionless constants used were different, see Table 2.3. These values can be obtained from the data presented in Table 2.4 instead of Table 2.1.

13

Table 2.3: Values of dimensionless parameters (2.15) used in [46].

Physical quantity	Symbol	Value
Volumetric heat capacity ratio of the filtrating gas	a	$6.13 \cdot 10^{-4}$
Heat transfered to porous medium due to the reaction	q	1.0121
Lewis number (ratio of thermal and molecular diffusion)	L_e	0.214
Stoichiometric coefficient for oxygen	μ	205.8
Net stoichiometric coefficient for gas production	μ_g	68.19
Scaled ideal gas constant	b	1.0
Arrhenius number (dimensionless activation energy)	γ	23.69
Reaction coefficient	α	0.027

Table 2.4: Values of dimensional parameters compatible with the values of dimensionless parameters used in [46] and given in Table 2.3.

Physical quantity	Symbol	Value	Unit
inlet oxygen mass concentration	$\tilde{Y}^i$	1.0	(kg/kg)
molecular weight of gaseous products	M_g	0.0086	kg/mole
gaseous products density	ρ_g^i	0.2818	kg/m^3
coke particles specific surface area	a_s	1000	m^2/m^3
gas injection speed	v^i	2950	[m/day]

Chapter 3

Geometrical singular perturbation

3.1 Introduction

Many different works describe and use singular perturbation methods in order to study multiple scale and stiff problems [23, 30, 31, 50]. In this chapter we follow the singular perturbation theory presented in [31]. However, here we will apply this theory in order to obtain stable heteroclinic orbits of the dynamical system given by the system of ODEs, which were not studied in [31]. This chapter use slightly different notation as we describe later. Consider an autonomous system of ODEs for $\mathbf{x} \in \mathbb{R}^n$ and $y \in \mathbb{R}$:

$$\begin{cases} \dfrac{d\mathbf{x}}{dt} = \mathbf{f}(\mathbf{x}, y) \\ \dfrac{dy}{dt} = \epsilon g(\mathbf{x}, y), \end{cases} \tag{3.1}$$

where $\mathbf{f} = (f^1, \ldots, f^n)^T$ and g are smooth (C^1) functions of $\mathbf{x}$ and y, and ϵ is a small positive parameter (bold indicates vectors). The parameter ϵ implies that the change of y is small when compared to the change of $\mathbf{x}$. Let us assume that (3.1) has two isolated equilibria named $(-)$ and $(+)$:

$$\mathbf{f}(\mathbf{x}^-, y^-) = \mathbf{f}(\mathbf{x}^+, y^+) = 0 \quad \text{and} \quad g(\mathbf{x}^-, y^-) = g(\mathbf{x}^+, y^+) = 0. \tag{3.2}$$

Let us assume the existence of an heteroclinic orbit $\mathbf{x}(t), y(t)$ of system (3.1), which connects $(\mathbf{x}^-, y^-)$ at $t = -\infty$ to $(\mathbf{x}^+, y^+)$ at $t = +\infty$. We are interested in finding tjhis orbit. We consider the case $y^- \neq y^+$ when the slow component $y(t)$ undergoes a finite change. It is convenient to introduce the slow time $\hat{t} = \epsilon t$ and using the notation $\dot{\mathbf{x}} = d\mathbf{x}/d\hat{t}$, one rewrites

the system (3.1) as

$$\begin{cases} \epsilon\dot{\mathbf{x}} = \mathbf{f}(\mathbf{x}, y) \\ \dot{y} = g(\mathbf{x}, y). \end{cases} \tag{3.3}$$

Geometric aspects of such singularly perturbed equation were studied in [23, 31]. Quantitative study in the case of three equations was done in [18, 19].

3.2 Quasi-stationary limit

Let us denote by $(\mathbf{x}^0(\hat{t}), y^0(\hat{t}))$ the quasi-stationary limit $\epsilon \to 0$ of the heteroclinic solution $(\mathbf{x}(\hat{t}), y(\hat{t}))$. By taking $\epsilon = 0$ in system (3.3), we obtain

$$\mathbf{f}(\mathbf{x}^0, y^0) = 0, \tag{3.4}$$

$$\dot{y}^0 = g(\mathbf{x}^0, y^0). \tag{3.5}$$

Notice that (3.4) is a system of n scalar algebraic equations with $n + 1$ unknowns. We assume that this system defines a curve $\mathbf{\Gamma}_0$ in the space $(\mathbf{x}, y)$, which connects the equilibria $(-)$ and $(+)$, see Fig. 3.1a. We also assume that

$$\det \mathbf{f_x} \neq 0 \ \text{ on } \mathbf{\Gamma}_0, \tag{3.6}$$

where $\mathbf{f_x} = [\partial\mathbf{f}/\partial\mathbf{x}]$ is the Jacobian matrix of the function $\mathbf{f}(\mathbf{x}, y)$ for fixed y. By the implicit function theorem, equation (3.4) has a solution $\mathbf{x}^0 = \boldsymbol{\varphi}(y^0)$ such that the curve $\mathbf{\Gamma}_0$ is parametrized as $(\boldsymbol{\varphi}(y^0), y^0)$ for y^0 between y^- and y^+. Of course, $\boldsymbol{\varphi}(y^\pm) = \mathbf{x}^\pm$.
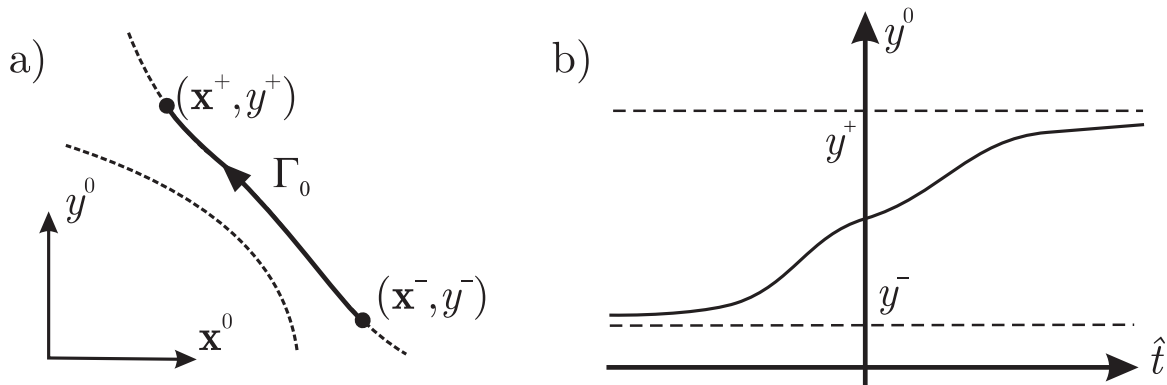
Figure 3.1: Heteroclinic orbit in quasi-stationary approximation: a) dependence of $\mathbf{x}^0$ on y^0, b) dependence of y^0 on $\hat{t}$.

16

By substituting $\boldsymbol{\varphi}(y^0)$ into Eq. (3.5), we obtain a scalar ODE for y^0:

$$\dot{y}^0 = g(\mathbf{x}^0(y^0), y^0). \tag{3.7}$$

According to (3.2), $g(\boldsymbol{\varphi}(y^0), y^0) = 0$ at $y^0 = y^\pm$. Hence, there exists a solution $y^0(\hat{t})$ such that $y^0 \to y^\pm$ as $\hat{t} \to \pm\infty$ if and only if

$$(y^+ - y^-)g(\mathbf{x}^0, y^0) > 0 \;\; \text{along} \;\; \boldsymbol{\Gamma}_0, \;\; \text{except at} \;\; (\mathbf{x}, y)^\pm, \tag{3.8}$$

of course $g(\mathbf{x}, y)^\pm = 0$. This solution is a monotone function of $\hat{t}$, see Fig. 3.1b. The function $y^0(\hat{t})$ is a heteroclinic orbit of scalar ODE (3.7). Since the heteroclinic orbit of an autonomous system is invariant under translations in time, equation (3.7) can be solved with the initial condition

$$y^0(0) = \check{y}^0, \tag{3.9}$$

where $\check{y}^0$ is an arbitrary number between y^- and y^+. Thus we recover the asymptotic heteroclinic solution as follows in terms of the slow time $\hat{t} = \epsilon t$.

The above discussion can be used as proof of the following proposition.

Proposition 3.1 *Let us assume that the equation* $\mathbf{f}(\mathbf{x}^0, y^0) = 0$ *determines a curve* $\boldsymbol{\Gamma}_0 = (\boldsymbol{\varphi}(y^0), y^0)$ *connecting the equilibria* $(\mathbf{x}^-, y^-)$ *to* $(\mathbf{x}^+, y^+)$*, satisfying the hypotheses (3.6), (3.8). Then the asymptotic heteroclinic solution of system (3.1) in the quasi-stationary limit* $\epsilon \to 0$ *is given by* $(\mathbf{x}^0(\hat{t}) = \boldsymbol{\varphi}(y^0(\hat{t})), y^0(\hat{t}))$*, where* $y^0(\hat{t})$ *is a solution of equation (3.7) with initial condition (3.9).*

3.3 Asymptotic series expansion

The approximate solution given by Prop. 3.1 is sufficient for many purposes. For example, if ϵ is very small, then the higher order approximations contain little useful information. However, in order to obtain more accuracy or estimate the error of approximation, one has to find higher order correction terms. Let us look for a solution of system (3.3) as an asymptotic power series in ϵ:

$$\mathbf{x}(\hat{t}) = \mathbf{x}^0(\hat{t}) + \epsilon\mathbf{x}^1(\hat{t}) + \epsilon^2\mathbf{x}^2(\hat{t}) + \cdots, \;\; y(\hat{t}) = y^0(\hat{t}) + \epsilon y^1(\hat{t}) + \epsilon^2 y^2(\hat{t}) + \cdots. \tag{3.10}$$

By substituting the expansions (3.10) into the functions $\mathbf{f}(\mathbf{x}, y)$ and $g(\mathbf{x}, y)$, after expanding them in a power series in ϵ, we obtain

$$\mathbf{f}(\mathbf{x}, y) = \mathbf{f}^0 + \epsilon\mathbf{f}_\mathbf{x}\mathbf{x}^1 + \epsilon\mathbf{f}_y y^1 + \cdots, \;\; g(\mathbf{x}, y) = g^0 + \epsilon\mathbf{g}_\mathbf{x}\mathbf{x}^1 + \epsilon g_y y^1 + \cdots. \tag{3.11}$$

Here $\mathbf{f}^0 = \mathbf{f}(\mathbf{x}^0, y^0)$, $g^0 = g(\mathbf{x}^0, y^0)$ and

$$\mathbf{f_x} = \begin{bmatrix} \frac{\partial f^1}{\partial x_1} & \cdots & \frac{\partial f^1}{\partial x_n} \\ \vdots & \ddots & \vdots \\ \frac{\partial f^n}{\partial x_1} & \cdots & \frac{\partial f^n}{\partial x_n} \end{bmatrix}, \ \mathbf{f}_y = \begin{bmatrix} \frac{\partial f^1}{\partial y} \\ \vdots \\ \frac{\partial f^n}{\partial y} \end{bmatrix}, \ \mathbf{g_x} = \begin{bmatrix} \frac{\partial g}{\partial x_1} & \cdots & \frac{\partial g}{\partial x_n} \end{bmatrix}, \ g_y = \begin{bmatrix} \frac{\partial g}{\partial y} \end{bmatrix}, \tag{3.12}$$

are functions of $\hat{t}$ evaluated at $(\mathbf{x}^0(\hat{t}), y^0(\hat{t}))$. Substituting (3.10)–(3.11) into (3.3), we obtain

$$\begin{cases} \epsilon(\dot{\mathbf{x}}^0 + \epsilon\dot{\mathbf{x}}^1 + \cdots) = \mathbf{f}^0 + \epsilon\mathbf{f_x}\mathbf{x}^1 + \epsilon\mathbf{f}_y y^1 + \cdots \\ \dot{y}^0 + \epsilon\dot{y}^1 + \cdots = g^0 + \epsilon\mathbf{g_x}\mathbf{x}^1 + \epsilon g_y y^1 + \cdots . \end{cases} \tag{3.13}$$

Since, for any ϵ, $\mathbf{x}(\hat{t}) \to x^{\pm}$ and $y(\hat{t}) \to y^{\pm}$ as $\hat{t} \to \pm\infty$, the components of the expansions (3.10) must satisfy the following conditions for all $k = 1, 2, \ldots$:

$$\mathbf{x}^0 \to x^{\pm}, \ y^0 \to y^{\pm}, \ \mathbf{x}^k \to 0, \ y^k \to 0 \ \text{ as } \ \hat{t} \to \pm\infty. \tag{3.14}$$

Equating terms with the same power of ϵ, we obtain a series of equations for the unknown functions $\mathbf{x}^0(\hat{t}), \mathbf{x}^1(\hat{t}), \ldots$ and $y^0(\hat{t}), y^1(\hat{t}), \ldots$. For the zero-th order terms we recover equations (3.4) and (3.5); thus, $\mathbf{x}^0(\hat{t})$ and $y^0(\hat{t})$ are given by Prop. 3.1.

For the first order terms in ϵ, (3.13) yields:

$$\begin{aligned} \dot{\mathbf{x}}^0 &= \mathbf{f_x}\mathbf{x}^1 + \mathbf{f}_y y^1, \\ \dot{y}^1 &= \mathbf{g_x}\mathbf{x}^1 + g_y y^1. \end{aligned} \tag{3.15}$$

The solution of this system is given in the following proposition.

Proposition 3.2 *Let us assume the hypotheses of Prop. 3.1[1]. Then the first order terms $\mathbf{x}^1(\hat{t})$ and $y^1(\hat{t})$ in the asymptotic expansion (3.10) have the form*

$$\mathbf{x}^1(\hat{t}) = \mathbf{f_x}^{-1}(\hat{t})\big(\dot{\mathbf{x}}^0(\hat{t}) - \mathbf{f}_y(\hat{t})y^1(\hat{t})\big), \tag{3.16}$$

$$y^1(\hat{t}) = g^0(\hat{t}) \int_0^{\hat{t}} B(\tau)d\tau, \quad B(\hat{t}) = \mathbf{g_x}(\hat{t})\mathbf{f_x}^{-2}(\hat{t})\mathbf{f}_y(\hat{t}). \tag{3.17}$$

Proof: Let us write (3.15) as:

$$\dot{\mathbf{x}}^0 - \mathbf{f}_y y^1 = \mathbf{f_x}\mathbf{x}^1, \tag{3.18}$$

$$\dot{y}^1 = \mathbf{g_x}\mathbf{x}^1 + g_y y^1. \tag{3.19}$$

---

[1]in particular it means that the function $g^0(\hat{t})$ is monotone for large $|\hat{t}|$.

Then (3.16) follows from (3.18) from multiplication by the inverse of the matrix $\mathbf{f_x}$ (which is nonsingular by the assumptions of Prop. 3.1). Using (3.4), (3.5) and the chain rule one obtains

$$\dot{\mathbf{x}}^0 = -\mathbf{f_x}^{-1}\mathbf{f}_y\dot{y}^0 = -\mathbf{f_x}^{-1}\mathbf{f}_y g^0. \tag{3.20}$$

Substituting this expression into (3.16) and using the result in (3.19) one gets

$$\dot{y}^1 = -\mathbf{g_x}\mathbf{f_x}^{-1}(\mathbf{f_x}^{-1}\mathbf{f}_y\, g^0 + \mathbf{f}_y y^1) + g_y y^1. \tag{3.21}$$

Now using (3.20) with the chain rule, we find the expression

$$\dot{g}^0 = \mathbf{g_x}\dot{\mathbf{x}}^0 + g_y\dot{y}^0 = -\mathbf{g_x}\mathbf{f_x}^{-1}\mathbf{f}_y g^0 + g_y g^0, \tag{3.22}$$

which can be used in (3.21) to get

$$\frac{d}{d\hat{t}}\left(\frac{y^1}{g^0}\right) = -B, \tag{3.23}$$

where B is defined in (3.17). Solving (3.23) one obtains

$$y^1 = cg^0(\hat{t}) + g^0(\hat{t})\int_0^{\hat{t}} B(\tau)d\tau, \tag{3.24}$$

where c is an arbitrary constant. The term cg^0 corresponds to the time-translations of the heteroclinic orbit. Thus, we can take $c = 0$, yielding (3.17).

Now we have to prove that $\mathbf{x}^1$ and y^1 given by (3.16) and (3.17) satisfy the conditions (3.14). As $\mathbf{f_x}$ is nonsingular, $B = \mathbf{g_x}\mathbf{f_x}^{-2}\mathbf{f}_y$ is a smooth (C^1) function of $\hat{t}$ with finite limits as $\hat{t} \to \pm\infty$. Thus, B is bounded: $|B(\hat{t})| < B_{max}$ for some B_{max}. Then y^1 satisfies the inequalities

$$|y^1(\hat{t})| = \left|g^0(\hat{t})\int_0^{\hat{t}} B(\tau)d\tau\right| \leq B_{max}\left|g^0(\hat{t})\hat{t}\right| \leq B_{max}\left(\left|g^0(\hat{t})T\right| + \left|g^0(\hat{t})(\hat{t} - T)\right|\right) \leq$$

$$\leq B_{max}\left(\left|g^0(\hat{t})T\right| + \left|\int_T^{\hat{t}} g^0(\tau)d\tau\right|\right) \leq B_{max}\left(\left|g^0(\hat{t})T\right| + \left|y^0(\hat{t}) - y^0(T)\right|\right), \tag{3.25}$$

where $\hat{t}$ and T are arbitrary (large) numbers belonging to the region where $g^0(\hat{t})$ is monotone by the hypothesis of the proposition. Here we also used the relation $\dot{y}^0 = g^0$. Now keeping T fixed and taking the limit $\hat{t} \to \pm\infty$ in (3.25), we obtain $\lim_{\hat{t}\to\pm\infty}|y^1(\hat{t})| \leq B_{max}|y^\pm - y^0(T)|$. Since $y^0(T) \to y^\pm$ as $T \to \pm\infty$, then $y^1 \to 0$ as $\hat{t} \to \pm\infty$. By using this property in (3.16), it is straightforward to show that $\mathbf{x}^1 \to 0$ as $\hat{t} \to \pm\infty$.

$\square$

Similarly, under the same assumptions, one could find formulae for higher order correction terms in the expansions (3.10).

Remark 3.1 *The hypothesis of monotonicity of $g^0(\hat{t})$ for large $\hat{t}$ in Prop. 3.2 is very natural: it is equivalent to the monotonicity of the function $g(\boldsymbol{\varphi}(y), y)$ in the neighborhood of $y^{\pm}$. It holds, for example, if $g(\boldsymbol{\varphi}(y), y)$ has nonzero derivative (of any order) with respect to y at $y^{\pm}$. In this work, we deal with the (exotic) non-hyperbolic case where all the derivatives of $g(\boldsymbol{\varphi}(y), y)$ vanish at y^{+}. However, the monotonicity condition is satisfied.*

Chapter 4

Coflow combustion

4.1 Introduction

A large number of studies on the structure of the combustion front have been reported since the 1950s, see [2, 4, 5, 7, 10, 32, 40], for instance. However, these studies present two peculiarities. First, they do not take into account other waves that occur in the combustion problem. As there are interactions between the combustion wave and these other waves, the solution of the Riemann problem taking into account all possible waves is relevant. Secondly, the combustion wave at the reservoir side (see Figure 2.1) can be controlled by the lack of oxygen or by low temperature. The works cited above study the more common temperature controlled case, which is not so amenable to analysis as the oxygen controlled case. The techniques used to study the combustion wave controlled by low temperature are very different from those presented here. For example, in [11] the approximate solution is a transient wave, i.e., this wave has a profile which changes very slowly. In this text we address the oxygen controlled case. A first step in this direction was taken in [46] for flow in reservoirs at relatively high temperatures: we now summarize the main results in [46].

Under the assumption that the combustion front governed by (2.23)-(2.26) moves forward exhausting all oxygen and fuel, i.e., the combustion reaction is fuel deficient behind the front and oxygen deficient ahead of it, the following theorem was proved in [46]: *assuming that the combustion front has a traveling wave profile, given the injection and the reservoir conditions, then the constant states and the speeds of all waves in the wave sequence defining the Riemann solution are uniquely determined.*

The theorem quoted above is scientifically incomplete, since it does not address the existence

of the traveling wave profile for the combustion wave: this is the main issue of this chapter. We performed numerical simulations for the model, obtained the traveling wave profile and compared it to the quasi–stationary approximation calculated semi-analytically. In this sense, this text completes the results of [46].

In Chapter 2 we presented the physical model (2.1)-(2.4), (2.7) in terms of masses and improved it by constructing analogous model (2.28)-(2.31), (2.27) in terms of molar masses. Both models generate the same dimensionless system of equations (2.23)-(2.26). From the mathematical point of view the difference between these two models is that the scaled stoichiometric coefficient μ is equal to 0 for the model in terms of molar masses. In order to maintain the generality we keep μ for our analysis in this chapter and also in Chapters 5 and 6.

4.2   The combustion wave

We consider the forward combustion wave with speed $V > 0$. Physically, there is no combustion ahead or behind this front, i.e, the reaction rate Φ must vanish. We consider that there is lack of fuel behind the combustion front, which is translated by condition (4.1); ahead of the combustion front, we consider oxygen deficiency as given by condition (4.2):

$$Y^b = 1, \quad \eta^b = 1, \quad v^b > 0, \tag{4.1}$$

$$\theta^u = 1, \quad Y^u = 0, \quad \eta^u = 0, \quad v^u > 0. \tag{4.2}$$

The superscripts b and u stand for *burned* and *unburned*. Of course, the reaction rate defined in (2.21) vanishes for the boundary conditions (4.1)–(4.2).

The combustion front is modeled as a steady traveling wave of system (2.23)–(2.26) with propagation speed V. The states along such a traveling wave depend only on the moving coordinate $\xi = x - Vt$, i.e, $\theta(x,t) = \hat{\theta}(\xi)$, $Y(x,t) = \hat{Y}(\xi)$ and $\eta(x,t) = \hat{\eta}(\xi)$. Then Eqs. (2.23)–(2.26) are transformed into (4.3)-(4.6), with hats omitted (for simplicity we use $b = 1$):

$$\frac{d}{d\xi}(av - V\theta) = \frac{d^2\theta}{d\xi^2} - q\frac{d}{d\xi}(V\eta), \tag{4.3}$$

$$\frac{d}{d\xi}\left(\frac{1}{\theta}(v - \phi V)Y\right) = \frac{1}{L_e}\frac{d}{d\xi}\left(\frac{1}{\theta}\frac{dY}{d\xi}\right) + \mu\frac{d}{d\xi}(V\eta), \tag{4.4}$$

$$\frac{d}{d\xi}\left(\frac{1}{\theta}(v - \phi V)\right) = -\mu_g\frac{d}{d\xi}(V\eta), \tag{4.5}$$

$$\frac{d}{d\xi}(V\eta) = -\Phi(\theta, Y, \eta), \tag{4.6}$$

where Eq. (2.20) was used to eliminate ρ. Integrating the equations (4.3)-(4.5) from ξ to $+\infty$ we obtain:

$$\frac{d\theta}{d\xi} - qV\eta - av + V\theta = -qV\eta^u - av^u + V\theta^u; \tag{4.7}$$

$$\frac{1}{L_e\theta}\frac{dY}{d\xi} + \mu V\eta - \frac{v - \phi V}{\theta}Y = \mu V\eta^u - \frac{v^u - \phi V}{\theta^u}Y^u; \tag{4.8}$$

$$\frac{v - \phi V}{\theta} + \mu_g V\eta = \frac{v^u - \phi V}{\theta^u} + \mu_g V\eta^u. \tag{4.9}$$

A traveling wave modeling the combustion front is an orbit of system (4.6),(4.7)-(4.9), connecting the burned state (4.1) to the unburned state (4.2). Using the fact that the burned and the unburned states must be equilibria of the system (4.3)-(4.6) we obtain:

$$\frac{d\theta}{d\xi} - qV\eta - av + V\theta = -av^u + V; \tag{4.10}$$

$$\frac{1}{L_e\theta}\frac{dY}{d\xi} + \mu V\eta - \frac{v - \phi V}{\theta}Y = 0; \tag{4.11}$$

$$\frac{v - \phi V}{\theta} + \mu_g V\eta = v^u - \phi V. \tag{4.12}$$

We can use (4.12) to obtain the volumetric flow rate v of the gas phase:

$$v = \phi V + \theta(v^u - \phi V) - V\theta\mu_g\eta. \tag{4.13}$$

Substituting (4.13) in (4.10) we obtain:

$$\frac{d\theta}{d\xi} = a(\phi V + \theta(v^u - \phi V) - V\theta\mu_g\eta) - (av^u - V) + qV\eta - V\theta. \tag{4.14}$$

Now we use (4.12) in (4.11) to obtain:

$$\frac{1}{L_e\theta}\frac{dY}{d\xi} = Y(v^u - \phi V - \mu_g V\eta) - \mu V\eta. \tag{4.15}$$

Using the condition (4.1) and manipulating the equations (4.13)–(4.15) we obtain the following expressions for the combustion wave speed V, the scaled temperature θ^b and the gas speed v^b:

$$V = \frac{v^u}{(\mu + \mu_g + \phi)}, \quad \theta^b = \frac{1 + q - a(\mu + \mu_g)}{1 - a\mu} \quad \text{and} \quad v^b = \phi V + \theta^b V\mu. \tag{4.16}$$

These relations coincide with the Rankine–Hugoniot shock conditions for system (2.23)–(2.26) with left and right states defined by (4.1)–(4.2): they show that the injection gas speed v^u, the production gas speed v^b and the combustion wave speed V are proportional, and that the

23

nondimensional temperature behind the combustion front does not depend on the injected gas speed.

Using the relations (4.16), we derive from (4.14), (4.15) and (4.6) the traveling wave system of ordinary differential equations that models the combustion front:

$$\frac{d\theta}{d\xi} = f^\theta \equiv V\big(a(\theta(\mu + \mu_g - \mu_g\eta) - \mu - \mu_g) + 1 + q\eta - \theta\big), \tag{4.17}$$

$$\frac{dY}{d\xi} = f^Y \equiv VL_e\theta\big((\mu + \mu_g - \mu_g\eta)Y - \mu\eta\big), \tag{4.18}$$

$$\frac{d\eta}{d\xi} = f^\eta \equiv -\frac{1}{V}\Phi(\theta, Y, \eta), \tag{4.19}$$

where the notation f^θ, f^Y, and f^η will be used later.

4.2.1 Parameter analysis

As we have shown in Chapter 3, in order to apply the singular perturbation method to solve system (4.17)–(4.19), the right-hand sides of equations (4.17)–(4.19) have to satisfy the relations:

$$f^\eta \ll f^\theta, \quad f^\eta \ll f^Y. \tag{4.20}$$

We define the parameter ϵ as:

$$\epsilon = \frac{\alpha}{V}\exp\left(\frac{-\gamma}{\theta^b}\right). \tag{4.21}$$

Thus the inequality $f^\eta < \epsilon$ is always satisfied. Among all the parameter that appear in the problem the reservoir temperature T^{res} and gas injection speed v^i are more likely to vary. In Table 2.1 the reservoir temperature was fixed $T^{res} = \tilde{T}_0$, however it typically varies between $273K$ and $1000K$ [37], the typical value for v^i is between $200\ [m/day]$ and $500\ [mday]$, see [2].

We compare the value of the parameter ϵ with the largest terms in f^θ, f^Y using the values of Table 2.2 and 2.3. The regions in parameter space $T^{res} \times v^i$ that correspond to first and second inequality of (4.20) are plotted respectively with dark and light colors. Figure 4.1 corresponds to parameter values used in [2] summarized in Tables 2.1 and 2.2. Figure 4.2 corresponds to parameter values used in [46] summarized in Tables 2.3 and 2.4.

4.2.2 Combustion wave profile

In Chapter 3 we proved several results on singular perturbation theory that will be used here. The difference between the application to combustion waves in this section and the theory
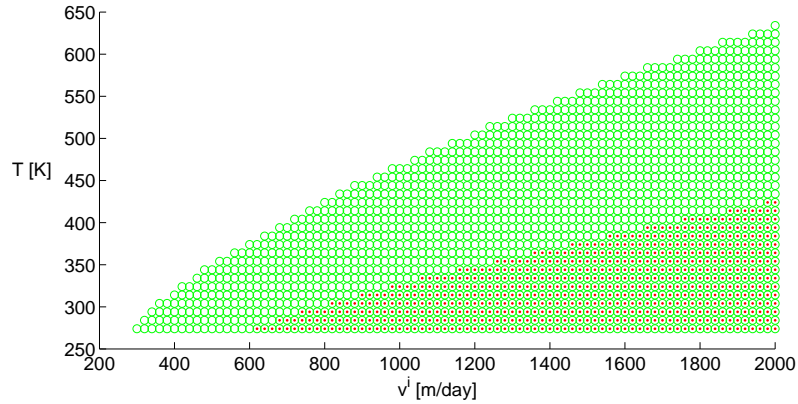
Figure 4.1: Regions in parameter space $T^{res} \times v^i$ corresponding to small epsilon. The region that satisfies the first inequality of (4.20) is printed in dark gray. The region that satisfies the second inequality of (4.20) is printed in light gray. Here we use the parameter values from Tables 2.1 and 2.2.
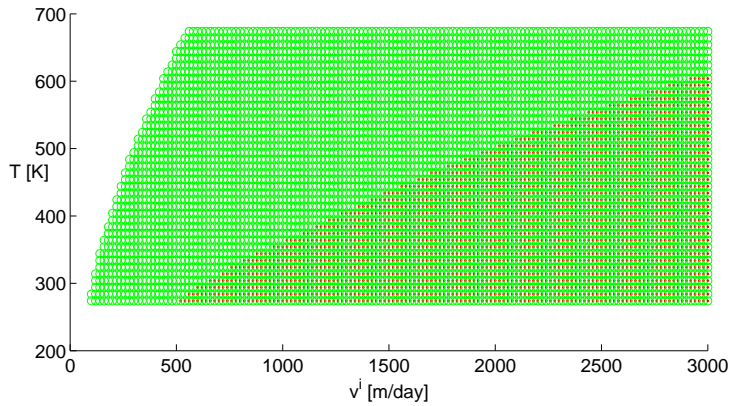
Figure 4.2: Regions in parameter space $T^{res} \times v^i$ corresponding to small epsilon. The region that satisfies the first inequality of (4.20) is printed in dark gray. The region that satisfies the second inequality of (4.20) is printed in light gray. Here we use the parameter values from Tables 2.3 and 2.4.

described in Chapter 3 is that here we have decided to maintain the small parameter ϵ hidden inside the field component f^η. This change of notation does not affect any result. Another notational difference is that in system (7.1) we have used (x_1, x_2, y), $(f^1, f^2, \epsilon g)$, and t instead of (θ, Y, η), (f^θ, f^Y, f^η) and ξ in (4.17)-(4.19).

The quasi-stationary combustion wave

According to (3.4), for a fixed value of V the quasi-stationary approximation of the system (4.17)-(4.19) is obtained by neglecting $d\theta/d\xi$ and $dY/d\xi$, yielding:

$$\theta^0(\eta^0) = \frac{1 + q\eta^0 - a(\mu + \mu_g)}{1 - a(\mu + \mu_g - \mu_g\eta^0)}, \qquad Y^0(\eta^0) = \frac{\mu\eta^0}{\mu + \mu_g - \mu_g\eta^0}. \tag{4.22}$$

The quasi-stationary approximation of the heteroclinic orbit parameterized by η^0 is:

$$\mathbf{\Gamma}_0 = \left(\theta^0(\eta^0), \ Y^0(\eta^0), \ \eta^0\right). \tag{4.23}$$

We want $\mathbf{\Gamma}_0$ to be a connected curve joining the equilibria of the vector field in (4.17)–(4.19). Thus we need the denominators in (4.22) not to vanish for any $\eta^0 \in [0, 1]$; this is true for the parameter values given in Table 2.3.

In order to obtain the approximate solution of system (4.17)-(4.19), we have to find η^0 in terms of ξ in (4.23). For this purpose, we substitute expressions in (4.22) for θ^0 and Y^0 into (4.19) and solve the resulting ODE for $\eta^0(\xi)$ with arbitrary initial data $\eta^0(\xi = 0)$ taken in the interval $(\eta^u, \eta^b) = (0, 1)$.

$$\begin{cases} \dfrac{d\eta^0}{d\xi} = f^\eta(\mathbf{\Gamma}_0) \equiv -\dfrac{\alpha}{V} \dfrac{\mu\eta^0(1 - \eta^0)}{\mu + \mu_g - \mu_g\eta^0} \, exp\left(-\gamma \, \dfrac{1 - a(\mu + \mu_g - \mu_g\eta^0)}{1 + q\eta^0 - a(\mu + \mu_g)}\right) \\ \eta^0(0) = 0.5 \end{cases} \tag{4.24}$$

Once the problem parameters are specified, this initial value problem can be solved (at least numerically). The numerical solutions for the parameter values from Tables 2.3 and 2.2 are shown in Figures 4.3 and 4.4 respectively.

First order approximation for combustion waves

We use the notation $\partial_\theta f^\theta(\xi), \partial_Y f^\theta(\xi), \partial_\eta f^\theta(\xi), \partial_\theta f^Y(\xi), \ldots$ for the partial derivatives evaluated along the quasi-stationary solution $(\theta^0(\xi), Y^0(\xi), \eta^0(\xi))$. These derivatives can be easily calculated, see [14]. Let us look at the first order approximation of the solution as a perturbation of
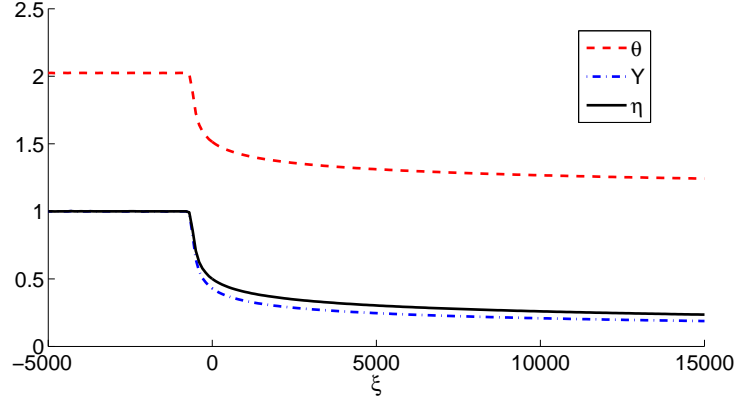
Figure 4.3: Zero-order approximation of the traveling wave. We used dimensionless parameter values from Table 2.2.

the quasi-stationary one.

$$\theta(\xi) = \theta^0(\xi) + \theta^1(\xi), \quad Y(\xi) = Y^0(\xi) + Y^1(\xi), \quad \eta(\xi) = \eta^0(\xi) + \eta^1(\xi). \tag{4.25}$$

The equations for the first order corrections θ^1, Y^1, η^1 obtained from the system (4.17)-(4.19) take the form:

$$\dot{\theta}^0 = (\partial_\theta f^\theta)\theta^1 + (\partial_Y f^\theta)Y^1 + (\partial_\eta f^\theta)\eta^1, \tag{4.26}$$

$$\dot{Y}^0 = (\partial_\theta f^Y)\theta^1 + (\partial_Y f^Y)Y^1 + (\partial_\eta f^Y)\eta^1, \tag{4.27}$$

$$\dot{\eta}^1 = (\partial_\theta f^\eta)\theta^1 + (\partial_Y f^\eta)Y^1 + (\partial_\eta f^\eta)\eta^1, \tag{4.28}$$

(see (3.15) in Chapter 3, where the equations (4.26), (4.27) correspond to (3.18), and (4.28) corresponds to (3.19)). Using (4.22) one obtains $\partial_Y f^\theta = \partial_\theta f^Y = 0$. Thus (4.26), (4.27) can be rewritten as:

$$\begin{bmatrix} \theta^1 \\ Y^1 \end{bmatrix} = \begin{bmatrix} (\partial_\theta f^\theta)^{-1} & 0 \\ 0 & (\partial_Y f^Y)^{-1} \end{bmatrix} \left(\begin{bmatrix} \dot{\theta}^0 \\ \dot{Y}^0 \end{bmatrix} - \begin{bmatrix} \partial_\eta f^\theta \\ \partial_\eta f^Y \end{bmatrix} \eta^1 \right). \tag{4.29}$$

Using (4.22) and (4.24) in (4.29) we obtain explicitly θ^1 and Y^1 as linear functions of η^1. Now substituting θ^1 and Y^1 into Eq. (4.28) we obtain the ODE for $\eta^1(\xi)$. As it is shown in Prop. 3.2, the solution of the resulting ODE has the form:

$$\eta^1(\xi) = f^\eta \int_0^\xi B(\tau)d\tau, \quad B = - \begin{bmatrix} \partial_\theta f^\eta & \partial_Y f^\eta \end{bmatrix} \begin{bmatrix} \partial_\theta f^\theta & \partial_Y f^\theta \\ \partial_\theta f^Y & \partial_Y f^Y \end{bmatrix}^{-2} \begin{bmatrix} \partial_\eta f^\theta \\ \partial_\eta f^Y \end{bmatrix}. \tag{4.30}$$

(a)

(b)
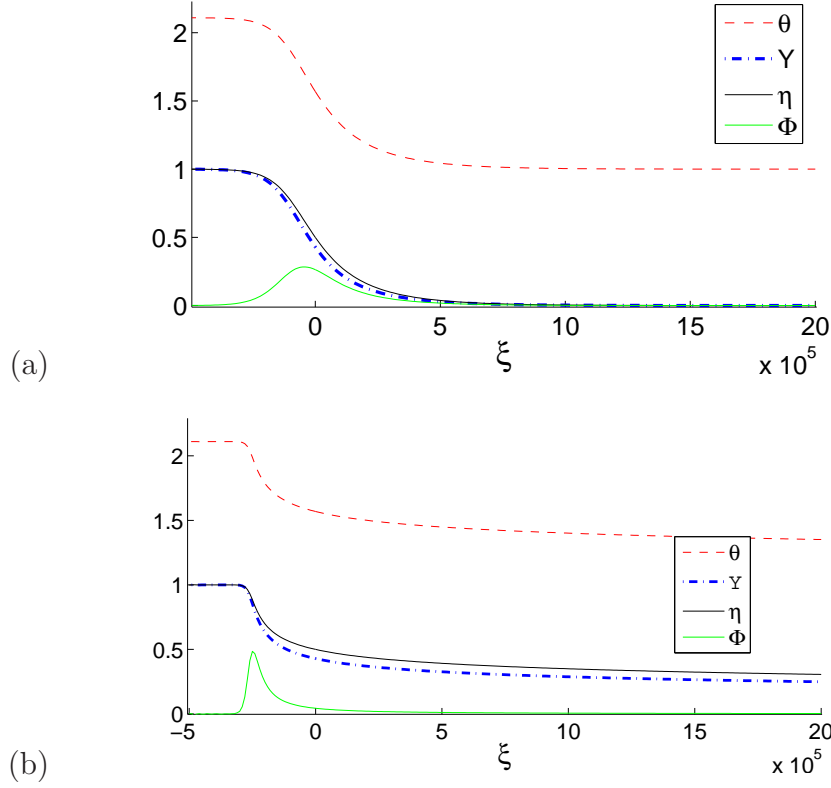
Figure 4.4: Zero-order approximation of the traveling wave (monotone) and the combustion rate Φ (hump) scaled by $2 \cdot 10^7$. In (a) $\gamma = 2.0$ and $\alpha = 1.6 \cdot 10^{-6}$ were used. In (b) the original dimensionless values from Table 2.3 were used.

It is possible to evaluate B explicitly, (see [14]). The equations (4.29) and (4.30) make sense if the Jacobian determinant $\partial(f^\theta, f^Y)/\partial(\theta, Y)$ (denoted $\det(\mathbf{f_x})$ in Chapter 3) does not vanish for appropriate parameters. It can be shown that:

$$\det \begin{bmatrix} \partial_\theta f^\theta & \partial_Y f^\theta \\ \partial_\theta f^Y & \partial_Y f^Y \end{bmatrix} = -V^2 L_e (K + a\mu_g \eta^0) \frac{(\mu + \mu_g - \mu_g \eta^0)(K + q\eta^0)}{K - a\mu_g \eta^0}, \qquad (4.31)$$

where $K = 1 - a(\mu + \mu_g)$. For V given in (4.16) and the parameter values given in Table 2.3 the factors in (4.31) do not vanish and the first order approximation of the combustion wave is well defined. We have plotted the corrections $\eta^1(\eta^0)$, $\theta^1(\eta^0)$ and $Y^1(\eta^0)$ in Figures 4.5 and 4.6. We have shown that the amplitude of the first-order approximation is small. This means that the parameter ϵ is indeed small as described in Propositions 3.1 and 3.2 and that the zero-order approximations shown in Figures 4.4 and 4.3 are good approximations of the combustion wave profile.

28
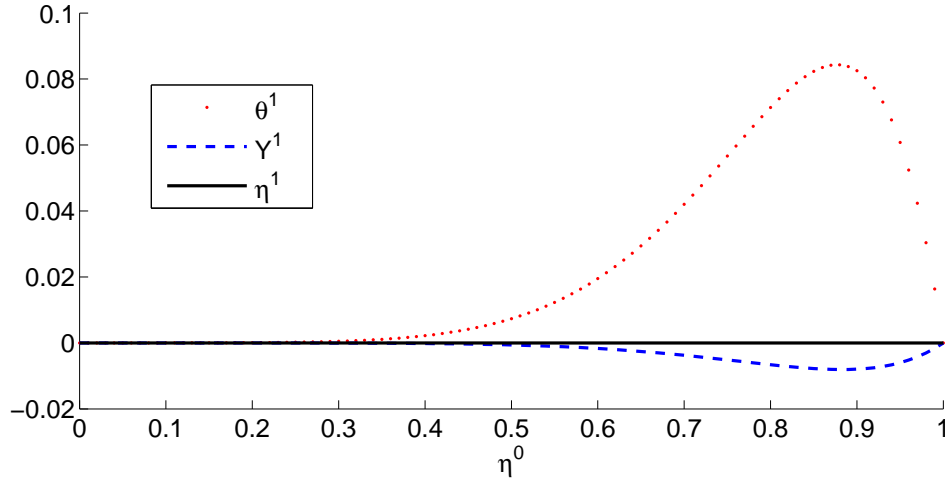
Figure 4.5: The plot represents the first order correction $\eta^1(\eta^0)$, $\theta^1(\eta^0)$ and $Y^1(\eta^0)$ corresponding to zero-order approximation from Figure 4.3. Here we have used the dimensionless parameter values from Table 2.2.
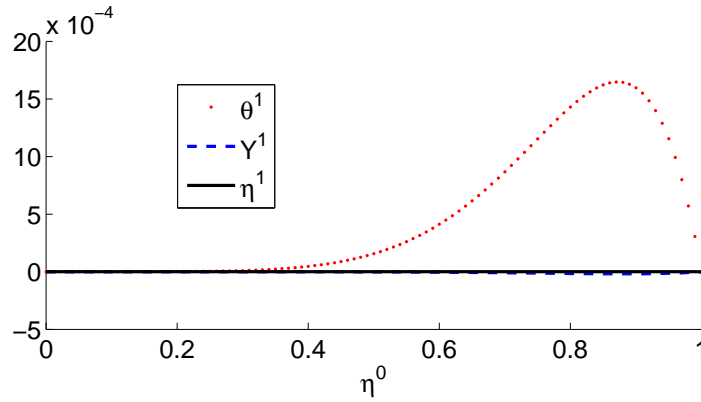
Figure 4.6: The plot represents the first order correction $\eta^1(\eta^0)$, $\theta^1(\eta^0)$ and $Y^1(\eta^0)$ corresponding to zero-order approximation from Figure 4.4. Here we have used the dimensionless parameter values from Table 2.3.

Monotonicity

In order to use Proposition 3.2 we have to verify that $f^\eta\big(\theta^0(\eta^0(\xi)), Y^0(\eta^0(\xi)), \eta^0(\xi)\big)$ is monotone in ξ in the neighborhood of the equilibria. However, the quasi-stationary approximation of the traveling wave solution of (2.16)–(2.19) coincides with the solution of the model solved in Chapter 5. We prove the monotonicity hypotheses in Section 5.3.1.

Explicit formulae of the approximate solution

In Section 4.2.2 we have solved the ODE (4.24) numerically. Here we obtain explicitly an approximation of the solution using the fact that $a << 1$ to modify the exponent:

$$\gamma \frac{1 - a(\mu + \mu_g - \mu_g \eta)}{a(\mu + \mu_g) - 1 - q\eta} \approx \frac{-\gamma}{1 + q\eta}. \tag{4.32}$$

Then we can rewrite the pre-exponential factor as:

$$-\frac{\alpha}{V} \frac{\mu \eta (1 - \eta)}{\mu + \mu_g - \mu_g \eta} = -\frac{\alpha}{V} \frac{(\mu/\mu_g)\eta(1 - \eta)}{\mu/\mu_g + 1 - \eta} = \frac{A\eta(1 - \eta)}{B - \eta}, \tag{4.33}$$

where $A = (-\alpha\mu)/(V\mu_g)$, $B = 1 + \mu/\mu_g$. The ODE for the approximate solution is:

$$\frac{d\eta}{d\xi} = \frac{A\eta(1 - \eta)}{B - \eta} \exp\left(\frac{-\gamma}{1 + q\eta}\right), \quad \eta(0) = 0.5. \tag{4.34}$$

In order to solve it we use the Exponential Integral function, [38]:

$$E_1(x) = \int_x^\infty \frac{\exp(-t)}{t} dt. \tag{4.35}$$

Solving the ODE (4.34):

$$\int_{\bar{\eta}}^\eta \frac{B - \eta}{A\eta(1 - \eta)} \exp\left(\frac{\gamma}{1 + q\eta}\right) d\eta = \frac{1}{A} \int_{\bar{\eta}}^\eta \left(\frac{B}{\eta} + \frac{B - 1}{1 - \eta}\right) \exp\left(\frac{\gamma}{1 + q\eta}\right) d\eta. \tag{4.36}$$

Substituting $x = \gamma/(1 + q\eta)$, $\eta = (\gamma - x)/(qx)$, $d\eta = -\gamma/(qx^2)dx$, $x(\eta) = x$, $\bar{x} = x(\bar{\eta})$ in the RHS of (4.36), it becomes:

$$\frac{B}{A} \int_{\bar{x}}^x \frac{qx}{(\gamma - x)} e^x \frac{-\gamma}{qx^2} dx + \frac{B - 1}{A} \int_{\bar{x}}^x \frac{qx}{(-\gamma + (1 + q)x)} e^x \frac{-\gamma}{qx^2} dx =$$
$$= \frac{-\gamma B}{A} \int_{\bar{x}}^x \frac{e^x}{x(\gamma - x)} dx - \frac{\gamma(B - 1)}{A} \int_{\bar{x}}^x \frac{e^x}{x(-\gamma + (1 + q)x)} dx. \tag{4.37}$$

Now we will calculate both integrals from the right hand side of (4.37) separately. The first one is:

$$\frac{-\gamma B}{A} \int_{\bar{x}}^x \frac{e^x}{x(\gamma - x)} dx = \frac{-\gamma B}{A} \int_{\bar{x}}^x \left(\frac{1}{x} + \frac{1}{\gamma - x}\right) \frac{e^x}{\gamma} dx =$$
$$\frac{-B}{A} \int_{\bar{x}}^x \frac{e^x}{x} dx + \frac{-B}{A} \int_{\bar{x}}^x \frac{e^x}{(\gamma - x)} dx = \frac{-B}{A} \int_{\bar{x}}^x \frac{e^x}{x} dx + \frac{-B}{A} \int_{\gamma - \bar{x}}^{\gamma - x} \frac{e^{\gamma - x}}{x} d(\gamma - x) =$$
$$\frac{-B}{A} \int_{\bar{x}}^x \frac{e^x}{x} dx + \frac{Be^\gamma}{A} \int_{\gamma - \bar{x}}^{\gamma - x} \frac{e^{-x}}{x} dx =$$
$$= \frac{-B}{A}(E_1(-\bar{x}) - E_1(-x)) + \frac{Be^\gamma}{A}(E_1(\gamma - \bar{x}) - E_1(\gamma - x)). \tag{4.38}$$

The second one is:

$$\frac{\gamma(B-1)}{A}\int_{\bar{x}}^{x}\frac{e^x}{x(-\gamma+(1+q)x)}dx = \frac{\gamma(B-1)}{A}\int_{\bar{x}}^{x}\left(\frac{1}{x}-\frac{1+q}{(1+q)x-\gamma}\right)\frac{-e^x}{\gamma}dx =$$

$$\frac{-(B-1)}{A}\int_{\bar{x}}^{x}\frac{e^x}{x}dx + \frac{(B-1)}{A}\int_{\bar{x}}^{x}\frac{(1+q)e^x}{(1+q)x-\gamma}dx = \tag{4.39}$$

$$\frac{-(B-1)}{A}\int_{\bar{x}}^{x}\frac{e^x}{x}dx + \frac{(B-1)}{A}\int_{\bar{x}}^{x}\frac{e^x}{x-\gamma/(1+q)}dx.$$

Define $\bar{K}=\gamma/(1+q)$, (4.39) becomes:

$$\frac{-(B-1)}{A}\int_{\bar{x}}^{x}\frac{e^x}{x}dx + \frac{(B-1)e^{\bar{K}}}{A}\int_{\bar{x}-\bar{K}}^{x-\bar{K}}\frac{e^x}{x}dx = \tag{4.40}$$

$$\frac{-(B-1)}{A}(E_1(-\bar{x})-E_1(-x)) + \frac{(B-1)e^{\bar{K}}}{A}(E_1(\bar{K}-\bar{x})-E_1(\bar{K}-x)). \tag{4.41}$$

Substituting (4.38) and (4.40) into (4.36) we obtain x as function of ξ in the implicit form:

$$\frac{-B}{A}(E_1(-\bar{x})-E_1(-x)) + \frac{Be^{\gamma}}{A}(E_1(\gamma-\bar{x})-E_1(\gamma-x))+$$

$$\frac{(B-1)}{A}(E_1(-\bar{x})-E_1(-x)) - \frac{(B-1)e^{\bar{K}}}{A}(E_1(\bar{K}-\bar{x})-E_1(\bar{K}-x)) = \xi. \tag{4.42}$$

Using the Exponential Integral function, [38], the implicit solution of the ODE (4.34) is:

$$-\frac{1}{A}\left(E_1\left(\frac{-\gamma}{1+q\bar{\eta}}\right)-E_1\left(\frac{-\gamma}{1+q\eta}\right)\right) + \frac{Be^{\gamma}}{A}\left(E_1\left(\frac{\gamma q\bar{\eta}}{1+q\bar{\eta}}\right)-E_1\left(\frac{\gamma q\eta}{1+q\eta}\right)\right)-$$

$$-\frac{(B-1)}{A}\exp(\frac{\gamma}{1+q})\left(E_1\left(\frac{\gamma q(\bar{\eta}-1)}{(1+q)(1+q\bar{\eta})}\right)-E_1\left(\frac{\gamma q(\eta-1)}{(1+q)(1+q\eta)}\right)\right) = \xi. \tag{4.43}$$

Now we notice that not all terms in the solution (4.43) are important. First we combine all constants:

$$\tilde{K} = \frac{1}{A}\left[-E_1\left(\frac{-\gamma}{1+q\bar{\eta}}\right)+Be^{\gamma}E_1\left(\frac{\gamma q\bar{\eta}}{1+q\bar{\eta}}\right)-(B-1)\exp(\frac{\gamma}{1+q})E_1\left(\frac{\gamma q(\bar{\eta}-1)}{(1+q)(1+q\bar{\eta})}\right)\right] \tag{4.44}$$

and eliminate the term $E_1(-\gamma/(1+q\eta))$, as it is small compared to the other ones, obtaining:

$$-Be^{\gamma}E_1\left(\frac{\gamma q\eta}{1+q\eta}\right)+(B-1)\exp(\frac{\gamma}{1+q})E_1\left(\frac{\gamma q(\eta-1)}{(1+q)(1+q\eta)}\right) = (\xi-\tilde{K})A. \tag{4.45}$$

The solution in (4.45) is implicit in η and not very easy to work with directly. We can simplify it utilizing the series expansion of the Exponential Integral function, see [38], and taking the real part, getting the approximation:

$$(\xi-\tilde{K})A = Be^{\gamma}\log\left(\frac{\gamma q\eta}{1+q\eta}\right)-(B-1)\exp(\frac{\gamma}{1+q})\log\left(\frac{\gamma q(\eta-1)}{(1+q)(1+q\eta)}\right). \tag{4.46}$$

We can compare the solution of (4.46) with the numerical solution of (4.24) on Figure 4.7.

31
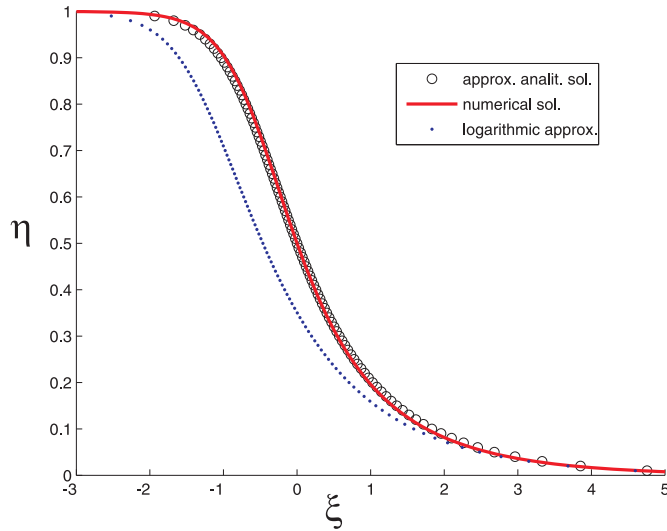
Figure 4.7: The numerical solution of (4.24) (solid), the analytical solution (4.43) of the approximate ODE (4.34) (circles) and the logarithmic approximation (4.46) (dotted). We use $\gamma = 2.0$.

Remark 4.1 *There is another possible simplification. We present it here, however it is not very accurate for the values of the parameters we use. By analyzing the profile of the numerical solution of (4.24) we conclude that the unburned part of the wave (at the right) is much larger that the burned part (at the left). Having this in mind we simplify the pre-exponential coefficient from the right hand side of (4.33). Taking $B \approx 1$ and $\mu \approx \mu_g$, the pre-exponential coefficient becomes $-\alpha\eta/V$. Next we use the simplification (4.32) for the exponential and obtain the simplified ODE:*

$$\frac{d\eta}{d\xi} = -\frac{\alpha\eta}{V} \exp\left(\frac{-\gamma}{1+q\eta}\right), \quad \eta(0) = 0.5. \tag{4.47}$$

We compare the solutions of the ODEs (4.24), (4.34) and (4.47) on Figure 4.8. One can see that the analytical solution (4.43) (circles) coincides with the numerical solution of (4.24) (solid line), while the solution of the simplified equation (4.47) (dotted) is an acceptable approximation to the numerical solution only for positive ξ.

Remark 4.2 *Analogously to (4.34) it is possible to use the Exponential Integral functions and obtain the implicit solution of the simplified ODE (4.47):*

$$\left[E_1(\frac{-2\gamma}{2+q}) - E_1(\frac{-\gamma}{1+q\eta})\right] - e^\gamma \left[E_1(\frac{\gamma q}{2+q}) - E_1(\frac{\gamma q\eta}{1+q\eta})\right] = \frac{\alpha\xi}{V}. \tag{4.48}$$

32
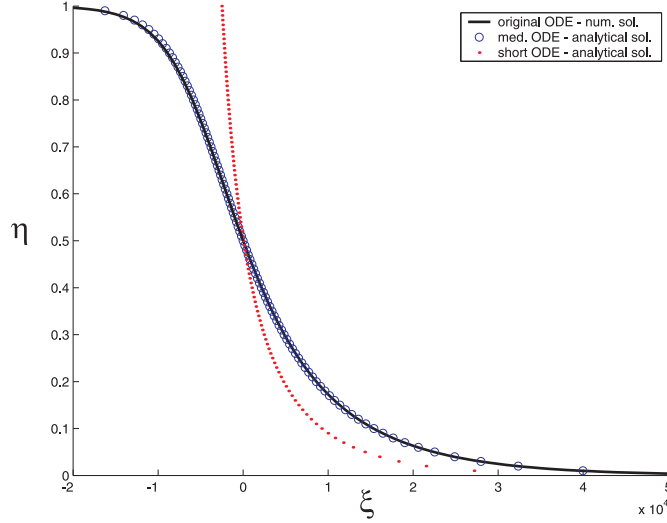
Figure 4.8: The numerical solution of (4.24) (solid), the analytical solution (4.43) of the approximate ODE (4.34) (circles) and the numerical solution of (4.47) (dotted). We use $\gamma = 2.0$.

Making the series expansions, taking the real part of it and combining all the constants into $\tilde{K}$ we get the simpler expression:

$$\left[-\log(\frac{-\gamma}{1+q\eta}) \right] + e^{\gamma} \left[\log(\frac{\gamma q\eta}{1+q\eta}) \right] = \frac{\alpha\xi}{V} - \tilde{K}. \tag{4.49}$$

4.2.3 Physical reasonability

So far we have studied the nondimensional equations and made nondimensional analysis. However, in order to better understand the underlying physical phenomena, it is important to study the dimensional problem. The variables θ, Y and η have been nondimensionalized in a natural way as scaled temperature, oxygen saturation and scaled fuel, respectively. We now investigate the characteristic length of our problem.

In order to obtain the characteristic length of the solution, we first determine the interval $\delta\xi$ where the combustion occurs. From the fuel consumption rate in equation (4.24) we conclude that the reaction occurs close to the region where $\eta \approx 0.5$; from the numerical experiments we conclude that it happens for $0.4 \le \eta \le 0.8$.

We are interested in the approximate length of the combustion wave, thus we use Figure 4.3 and get $\delta\xi \approx 10^3$.

For the parameter values taken from Table 2.3 from (4.46), with some simplifications, we have:

$$\delta\xi \approx \frac{2V}{\alpha}\exp(\frac{\gamma}{1+q}) \approx 10^5.$$ (4.50)

This last approximation is not accurate. However, we are only interested in the approximate length.

To find the values for physical variables we use (2.8) with the characteristic injection speed $v^* = v^i$. We use Table 2.1 and obtain the scaled effective thermal diffusivity $\alpha_s = \tilde{\lambda}/((1-\phi)c_s\rho_s) = 4.3 \cdot 10^{-7}\,[m^2/s]$ and the reference length $l^* = \alpha_s/v^*$. We recover all dimensional variables: temperature $\widetilde{T} = \widetilde{T}_0\theta$, where $\widetilde{T}_0$ is the reservoir temperature; time $\tilde{t} = t^* = \hat{t}\alpha_s/(v^*)^2$; length $\tilde{x} = l^*\hat{x}$.

Next we obtain dimensional values for the characteristic length using two data sets we have. Firstly, we substitute the values of the parameter from Table 2.1 with $v^* = 500\,[m/day]$ and obtain $l^* \approx 7.4 \cdot 10^{-5}\,[m]$, $\widetilde{T} \approx 755.4\,[K]$, $t^* \approx 1.28 \cdot 10^{-2}\,[s]$, $\tilde{x} \approx 0.074\,[m]$. Secondly we use the parameter values from [46] given in Table 2.4 and obtain $l^* \approx 1.26 \cdot 10^{-5}\,[m]$, $\widetilde{T} \approx 787.5\,[K]$, $t^* \approx 3.69 \cdot 10^{-4}\,[s]$, $\tilde{x} \approx 0.126\,[m]$.

Both data set are compatible with experimental data, see [22].

4.3   Wave sequences

In this chapter we concentrate our efforts on the analysis of the combustion wave, however it is important to note that there are other waves in this model. Studied in a hyperbolic framework, i.e., neglecting the diffusion terms, these waves are contact discontinuities. The hyperbolic analysis of these waves coincides for the current model and other model studied in Chapter 5. We expect them to appear in the solution as waves traveling with constant speed given by the hyperbolic theory and with smoothing effect caused by the diffusion. This behavior is observed within the numerical experiments as shown in Chapter 6. For these reasons we postpone the discussion about the wave sequences to Chapter 5.

In Section 5.4 we prove that given the injection conditions all combustion and non combustion wave speeds, all constant states in the wave sequence and the combustion wave propagation speed are uniquely determined.

4.4 Conclusion

In this chapter we look for the traveling wave for the in-situ combustion model studied in [2, 3, 46]. We present the two-terms asymptotic expansion given by $\theta(\xi) = \theta^0(\xi) + \theta^1(\xi)$, $Y(\xi) = Y^0(\xi) + Y^1(\xi)$ and $\eta(\xi) = \eta^0(\xi) + \eta^1(\xi)$, where the zero-order approximations θ^0, Y^0, η^0 are given by formulae (4.22a), (4.22b) and (4.24), respectively, see Fig. 4.4. The first order approximation θ^1, Y^1 and η^1 are given by formulae (4.29) and (4.30), respectively.

This, by itself, is a strong evidence that the combustion wave possesses a traveling wave profile. In Chapter 6 we will present the numerical simulations showing the formation of the traveling wave and compared it to the approximate solution confirming our analysis, see Fig. 6.2.

Moreover, setting to zero the value of a very small parameter (the volumetric heat capacity ratio of the filtration gas a), an explicit formula for the approximate solution was obtained, see Figure 4.7. This formula was used to estimate the characteristic length of the combustion wave.

We conclude that the first order expansion solution of the traveling wave ODE system exists and justifies quasi-mathematically the Riemann solution obtained in [46]. The results discussed in this chapter were published in [19].

Chapter 5

Non-diffusive combustion waves in porous media

5.1 Introduction

In order to model ISC some simplifications are commonly made. For example, the authors of [6] use a one-dimensional model and assume limitless access to fuel and constant gas speed, obtaining a system of two conservation laws. Next, the Lewis number is considered high in the analysis of the stability of the combustion front.

In this chapter we follow the formulation of [14, 19, 46] explained in Chapter 4. However, we utilize the simplification of neglecting diffusion terms (physically it is valid when the gas velocity is very high). We also solve the corresponding Riemann problem and obtain the combustion wave profile. It turns out that it coincides with the zero-order approximation of the combustion wave for the model introduced in Section 2.1 and studied in Chapter 4 by using the singular perturbation technique.

Although we use the system (2.16)-(2.19) to illustrate the result above, the result is valid for more general systems of conservation laws. In fact, the traveling wave solution of the system (2.16)-(2.19) with diffusion and conduction terms removed coincides with the zero-order approximation obtained through the use of the singular perturbation technique for system (2.16)-(2.19). In other words, when applying singular perturbation analysis to find traveling wave solution, we can neglect the diffusion terms.

5.2 Simplified combustion model

We analyze the following simplification of the model (2.16)-(2.19), in which the molecular diffusion and thermal heat conductivity have been neglected:

$$\frac{\partial \theta}{\partial t} + \frac{\partial (a\rho v \theta)}{\partial x} = q\Phi \tag{5.1}$$

$$\phi \frac{\partial (Y\rho)}{\partial t} + \frac{\partial (\rho v Y)}{\partial x} = -\mu\Phi, \tag{5.2}$$

$$\phi \frac{\partial \rho}{\partial t} + \frac{\partial (\rho v)}{\partial x} = \mu_g \Phi, \tag{5.3}$$

$$\frac{\partial \eta}{\partial t} = \Phi, \tag{5.4}$$

$$\rho\theta = 1. \tag{5.5}$$

We use the first order mass action law combined with the usual Arrhenius' law (2.21):

$$\Phi = \alpha Y(1-\eta)e^{-\frac{\gamma}{\theta}}, \text{ for } \theta > 0 \quad \text{and} \quad \Phi = 0, \text{ for } \theta \le 0.$$

Here we focus on the forward combustion front with propagation speed $V > 0$. The boundary conditions for the combustion wave are the same as in (4.1)-(4.2):

$$Y^b = 1, \quad \eta^b = 1, \quad v^b > 0,$$

$$\theta^u = 1, \quad Y^u = 0, \quad \eta^u = 0, \quad v^u > 0;$$

where the superscripts b and u mean *burned* and *unburned*.

The states along such a traveling wave depend only on the moving coordinate $\xi = x - Vt$, i.e, $\theta(x,t) = \hat{\theta}(\xi)$, $Y(x,t) = \hat{Y}(\xi)$ and $\eta(x,t) = \hat{\eta}(\xi)$. Then Eqs. (5.1)–(5.5) are transformed into (5.6)-(5.9), with hats omitted:

$$\frac{d}{d\xi}(av - V\theta) = q\Phi, \tag{5.6}$$

$$\frac{d}{d\xi}\left(\frac{Y(v - \phi V)}{\theta}\right) = -\mu\Phi, \tag{5.7}$$

$$\frac{d}{d\xi}\left(\frac{v - \phi V}{\theta}\right) = \mu_g\Phi, \tag{5.8}$$

$$\frac{d}{d\xi}(V\eta) = -\Phi, \tag{5.9}$$

where Eq. (5.5) was used to eliminate ρ. The boundary conditions for system (5.6)–(5.9) are the conditions (4.1) at $-\infty$ and (4.2) at $+\infty$.

Notice that (5.6)-(5.9) is a first-order ODE system, which can be rewritten in a matrix form as:

$$
\begin{bmatrix}
-V & 0 & 0 & a \\
0 & \dfrac{V\phi - v}{-\theta} & 0 & 0 \\
\dfrac{(V\phi - v)}{\theta^2} + \dfrac{V}{a\theta} & 0 & 0 & 0 \\
0 & 0 & -V & 0
\end{bmatrix}
\begin{bmatrix}
\theta_\xi \\
Y_\xi \\
\eta_\xi \\
v_\xi
\end{bmatrix}
=
\begin{bmatrix}
q \\
-\mu - Y\mu_g \\
\mu_g - \dfrac{q}{a\theta} \\
1
\end{bmatrix}
\Phi.
\tag{5.10}
$$

The matrix on the left-hand side of Eq. (5.10) can be inverted, provided that:

$$
V \neq 0 \equiv \lambda^\eta, \quad V \neq v/\phi \equiv \lambda^Y, \quad V \neq av/(\theta + a\phi) \equiv \lambda^\theta,
\tag{5.11}
$$

We will prove that the ODE system of Eq. (5.10) has a solution with boundary conditions defined by (4.1) and (4.2) for certain values of V.

5.2.1 The Rankine-Hugoniot locus

In order to obtain relations between the boundary conditions (4.1) and (4.2) so that system (5.10) has a solution, we substitute (5.9) into (5.6)-(5.8) obtaining:

$$
\frac{d}{d\xi} \left(av - V\theta + qV\eta \right) = 0,
\tag{5.12}
$$

$$
\frac{d}{d\xi} \left(\frac{(v - \phi V)Y}{\theta} - \mu V\eta \right) = 0,
\tag{5.13}
$$

$$
\frac{d}{d\xi} \left(\frac{v - \phi V}{\theta} + \mu_g V\eta \right) = 0.
\tag{5.14}
$$

This means that the quantities inside the derivatives are constant in ξ, thus their value at some finite ξ is the same as the one at $\xi \to \infty$:

$$
av - V\theta + qV\eta = av^u - V - qV\eta^u,
\tag{5.15}
$$

$$
\frac{vY}{\theta} - \frac{\phi VY}{\theta} - \mu V\eta = v^u Y^u - \phi VY^u - \mu V\eta^u,
\tag{5.16}
$$

$$
\frac{v}{\theta} - \frac{\phi V}{\theta} + \mu_g V\eta = v^u - \phi V + \mu_g V\eta^u.
\tag{5.17}
$$

Next we can take the limit $\xi \to -\infty$ on the left hand side of Eqs. (5.15)-(5.17) and substitute condition (4.1) on the left hand side and condition (4.2) on the right hand side of the resulting

system to obtain:

$$av^u - V = av^b - V\theta^b + qV, \tag{5.18}$$

$$0 = \frac{v^b - \phi V}{\theta^b} - \mu V, \tag{5.19}$$

$$v^u - \phi V = \frac{v^b - \phi V}{\theta^b} + \mu_g V. \tag{5.20}$$

Physically, it is reasonable to assume that we know the Darcy velocity (v^b) of the injected gas (this choice will be useful in Section 5.4), so we have three unknowns θ^b, v^u, V and three equations (5.18)-(5.20). We perform the same analysis as in Section 4.2 to obtain:

$$V = \frac{v^u}{(\mu + \mu_g + \phi)}, \quad \theta^b = \frac{1 + q - a(\mu + \mu_g)}{1 - a\mu} \quad \text{and} \quad v^b = \phi V + \theta^b V \mu.$$

These relations coincide with (4.16).

5.2.2 Combustion wave profile

In this section we use the boundary conditions defined in the introduction of Section 5.2 and the equations (5.12)-(5.14) to obtain θ, Y, v as functions of η and of the parameters, and substitute the result in the equation for η_ξ in (5.10). Then we compare these results to the solutions for the system (2.16)-(2.20) obtained by singular perturbation techniques in Chapter 4.

From equations (5.15)-(5.17) we obtain:

$$av - V\theta = av^u - V - qV\eta, \tag{5.21}$$

$$\frac{(v - \phi V)}{\theta}Y = \mu V\eta, \tag{5.22}$$

$$v = \phi V - \mu_g V \eta\theta + \theta(v^u - \phi V) = \phi V - \mu_g V \eta\theta + V\theta(\mu + \mu_g), \tag{5.23}$$

where we have used (4.16) to obtain (5.23). Substituting v from (5.23) and v^u from (4.16) into (5.21), dividing by V and simplifying, we obtain:

$$\theta = \frac{a(\mu + \mu_g) - 1 - q\eta}{a(\mu + \mu_g - \mu_g\eta) - 1}. \tag{5.24}$$

Using (5.23) in (5.22) we get:

$$Y = \frac{\mu\eta}{\mu + \mu_g - \mu_g\eta}. \tag{5.25}$$

Finally, using (5.24), (5.25) and (2.21) we can rewrite the equation for η_ξ in (5.10) as:

$$\eta_\xi = \frac{\alpha Y(1 - \eta)}{-V}exp\left(\frac{-\gamma}{\theta}\right) = \frac{-\alpha\mu\eta(1 - \eta)}{(\mu + \mu_g - \mu_g\eta)V}\exp\left(\gamma\frac{1 - a(\mu + \mu_g - \mu_g\eta)}{a(\mu + \mu_g) - 1 - q\eta}\right). \tag{5.26}$$

We can solve this ODE with any initial condition $\eta(0) = \eta^0$, where $0 < \eta^0 < 1$ and substitute the result into the equations (5.23), (5.24) and (5.25) for θ, Y, v and obtain the combustion wave profile. Solving these equations with Matlab with initial condition $\eta^0 = 0.5$ we obtain the wave profile shown on the left side of Figure 5.1. The result coincides with the quasi-stationary approximation given in Chapter 4.
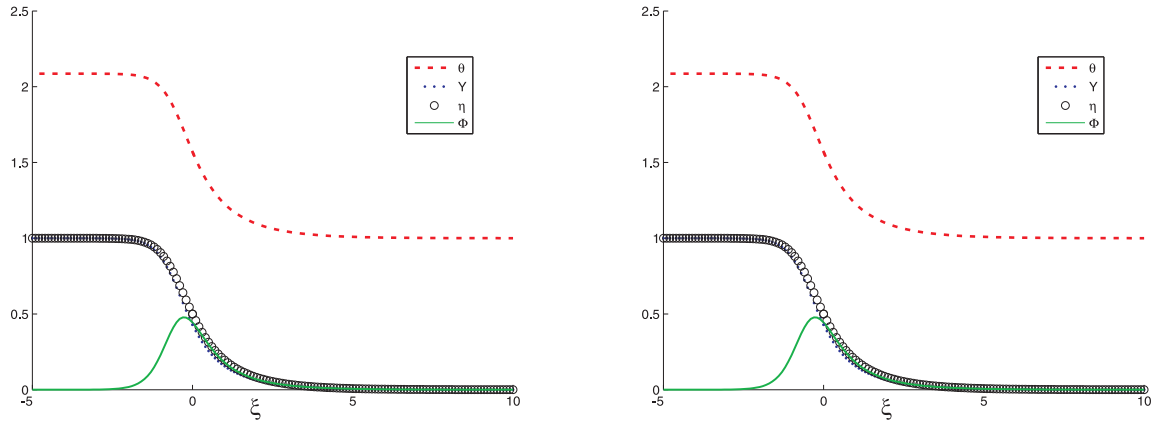
Figure 5.1: On the left: the traveling wave solution of the system (5.26). On the right: the first order approximation of the traveling wave of the system (2.16)-(2.19) from [18]. Variables: θ (segmented line), Y (dotted), η (circles) and combustion rate Φ (solid line) as functions of ξ. We use $\gamma = 2$.

Approximate explicit solution

We have solved the ODE (5.26) numerically, but sometimes it is useful to have an explicit approximation for the solution. However, the traveling wave solution of (5.1)-(5.4) coincides with the quasi-stationary approximation studied in Chapter 4. Thus, the implicit solution of ODE (4.34) using the exponential integral function is (4.45) and its logarithmic approximation is (4.46).

The dimensional solution

In this section, we study the non-dimensional equations and perform non-dimensional analysis, however for applications it is important to know the characteristic values of our solution in actual units. As the traveling wave solution of (5.1)-(5.4) coincides with the quasi-stationary

approximation studied in Chapter 4, the dimensional analysis coincides with that done in Section 4.2.3. The characteristic length of the combustion wave is $\tilde{x} \approx 0.07\,[m]$. This result is compatible with experimental data [22].

5.3 Testing the solution within the combustion wave

In order to solve the linear system (5.10), the restrictions (5.11) need to be satisfied for V. On the other hand our physical model imposes other restrictions related to the boundary conditions (4.1) and (4.2) for the combustion waves. Verifying these restrictions is the goal of this section. We perform this analysis using data from Table 2.3; for the Table 2.2 the calculations are analogous.

5.3.1 Monotonicity

Here we will prove that the solutions $\theta(\xi)$, $Y(\xi)$ and $\eta(\xi)$ of system (5.10) are monotonic in ξ. The combustion rate defined by (2.21) is always positive, thus from (5.10) or (5.26) we see that $\eta(\xi)$ is monotone decreasing.

In order to prove that $\theta(\xi)$ is monotonic we use (5.24) obtaining:

$$\frac{d\theta}{d\eta} = \frac{-q(a(\mu + \mu_g - \mu_g\eta) - 1) + (a(\mu + \mu_g) - 1 - q\eta)a\mu_g}{(a(\mu + \mu_g - \mu_g\eta) - 1)^2} = \frac{(q - a\mu_g)(1 - a(\mu + \mu_g))}{(a(\mu + \mu_g - \mu_g\eta) - 1)^2}. \tag{5.27}$$

The numerator of (5.27) is independent of η and it is positive for the parameter values from Table 2.3 and the denominator is positive. As $\eta(\xi)$ is monotonic, $\theta(\xi)$ is monotone decreasing and thus θ^b from (4.16) satisfies $\theta^b > \theta^u$.

In order to prove the monotonicity of $Y(\xi)$ we use (5.25) to obtain $dY/d\eta$:

$$\frac{dY}{d\eta} = \frac{\mu(\mu + \mu_g - \mu_g\eta) - \mu\eta(-\mu_g)}{(\mu + \mu_g - \mu_g\eta)^2} = \frac{\mu(\mu + \mu_g)}{(\mu + \mu_g - \mu_g\eta)^2}. \tag{5.28}$$

As the numerator of (5.28) is constant in η and the denominator is always positive, the function $Y(\xi)$ is monotonic. As $Y^u < Y^b$ we conclude that $Y(\xi)$ is monotone decreasing.

For the gas speed $v(\eta)$, given by (5.23) we will prove that it is monotonic close to the equilibria. Using (4.16) we obtain that $v^u - \phi V = V(\mu + \mu_g)$. From (5.23) we obtain:

$$\frac{d}{d\eta}(v - \phi V) = V(\mu + \mu_g - \mu_g\eta)\frac{d\theta}{d\eta} - \theta V \mu_g. \tag{5.29}$$

Using (5.27) and substituting the parameter values from Table 2.3 we obtain that $v(\eta)$ is monotonic close to the equilibria corresponding to the burned ($\eta = 1$) and unburned ($\eta = 0$) states.

At this point we have proved that the functions $\theta(\xi)$, $Y(\xi)$, $\eta(\xi)$ are monotonic for $-\infty < \xi < \infty$ and $v(\xi)$ is monotonic close to the equilibria, so they satisfy the boundary conditions given in (4.1) and (4.2). In other words, the wave speed V is physically admissible.

5.3.2   Verifying the characteristic inequalities

In this subsection we want to prove that V defined in (4.16) satisfies the restrictions (5.11). Obviously, V satisfies (5.11a). For (5.11b,c) we will show:

$$\frac{av(\eta)}{a\phi + \theta(\eta)} < V < \frac{v(\eta)}{\phi}. \tag{5.30}$$

In order to verify (5.30) we substitute $v(\eta)$ from (5.23) and verify each of these inequalities separately. For the first one we get:

$$\frac{a(\phi V + \theta V(\mu + \mu_g) - V\theta\mu_g\eta)}{a\phi + \theta(\eta)} < V, \tag{5.31}$$

which is equivalent to:

$$aV(\mu + \mu_g - \mu_g\eta) < 1. \tag{5.32}$$

This inequality is satisfied for the parameter values from Table 2.3.

The second inequality results in:

$$V < \frac{\phi V + \theta V(\mu + \mu_g) - V\theta\mu_g\eta}{\phi}, \tag{5.33}$$

which is equivalent to:

$$\eta < 1 + \frac{\mu}{\mu_g}. \tag{5.34}$$

This inequality is always satisfied as the fuel concentration depth η has values in $[0, 1]$.

Here we conclude that the solution of the system (5.10) for V defined in (4.16) always exists and that V satisfies (5.30) for typical data.

5.4   Non-combustion waves and wave sequences

In the absence of combustion, the source terms representing mass transfer or sensible heat generation containing the factor Φ vanish on the right hand side of system (5.1)–(5.5). Of

course Φ vanishes for $Y \equiv 0$ or $\eta \equiv 1$. We consider smooth solutions and expand the derivatives in the remaining terms in (5.1)-(5.4), manipulate (5.2), (5.3) and finally use (5.5) to eliminate ρ, obtaining:

$$\frac{\partial \theta}{\partial t} + a \frac{\partial v}{\partial x} = 0, \tag{5.35}$$

$$\phi \frac{\partial Y}{\partial t} + v \frac{\partial Y}{\partial x} = 0, \tag{5.36}$$

$$\left(\frac{\theta}{a} + \phi\right) \frac{\partial \theta}{\partial t} + v \frac{\partial \theta}{\partial x} = 0, \tag{5.37}$$

$$\frac{\partial \eta}{\partial t} = 0. \tag{5.38}$$

In increasing order, the characteristic speeds of system (5.35)-(5.38) and the corresponding characteristic vectors are [46]:

$$\lambda^\eta = 0, \qquad (0,0,1,0)^T, \tag{5.39}$$

$$\lambda^\theta = a \frac{v}{\theta + a\phi}, \qquad (1,0,0,\frac{v}{\theta + a\phi})^T, \tag{5.40}$$

$$\lambda^Y = v/\phi, \qquad (0,1,0,0)^T. \tag{5.41}$$

It is easy to see that all characteristic speeds are constant along the integral curves defined by the corresponding characteristic vector fields, which means that all the waves are contact discontinuities; of course, they satisfy the Rankine-Hugoniot conditions for (5.1)-(5.5). The characteristic speed λ^η corresponds to an immobile discontinuity along which only η varies, λ^θ corresponds to a thermal discontinuity along which θ and v vary and λ^Y corresponds to a gas composition discontinuity along which only Y varies.

In Section 5.3.2 we have seen that the wave speeds in (5.39)-(5.41) are all different and satisfy (5.30). Now we will describe the wave sequence in the Riemann solution under conditions (4.1) and (4.2) surrounding the combustion front [46].

We indicate by U the vector containing the variables (θ, Y, η, v). In our case (hot upstream combustion) the thermal wave is slower than the combustion wave $(\lambda^\theta(U^b) < V)$ and there is no temperature change ahead the combustion wave, which means that $\theta^b > \theta^u$. Because of the inequalities $\lambda^\eta < \lambda^\theta < \lambda^Y$, the wave sequence in the Riemann solution consists of an immobile fuel shock, a thermal shock with speed λ^θ and a combustion front with speed V. The gas composition wave with speed λ^Y does not effectively exist due to the complete oxygen consumption assumed in the boundary condition (4.2). We denote this sequence of waves by

43

means of the following convention:

$$U^i \xrightarrow{\lambda^\eta} U^1 \xrightarrow{\lambda^\theta} U^b \xrightarrow{V} U^u. \tag{5.42}$$

The state $U^i = (\theta^i, 1, 0, v^i)$ denotes the injection conditions, $U^1 = (\theta^i, 1, 1, v^i)$ denotes an intermediate state in the burned region, while $U^b = (\theta^b, 1, 1, v^b)$ and $U^u = (\theta^u, 0, 0, v^u)$ are the burned and the unburned states surrounding the combustion front.

We summarize our results in the following theorem, which provides formulae for all the states as well as speeds for combustion and non-combustion waves in the wave sequence (5.42) for the Riemann solution. In this theorem we have fixed the reservoir temperature at $\theta^u = 1$.

Theorem 5.1 *Assume that in the wave sequence for the Riemann solution of (5.1)-(2.21) there is a hot upstream combustion wave with left and right states satisfying (4.1)-(4.2) and $\theta^b > \theta^u$. For given injection conditions $U^i = (\theta^i, 1, 0, v^i)$, with $\theta^i > 0$, $v^i > 0$ and scaled reservoir temperature $\theta^u = 1$, the constant states and the speeds of all waves in the wave sequence (5.42) are uniquely determined.*

Proof. First of all, analogously to [46], the characteristic pair (5.40) corresponds to a contact discontinuity and there is a relationship between the injection conditions U^i and the burned state U^b:

$$a\frac{v^i}{\theta^i + a\phi} = a\frac{v^b}{\theta^b + a\phi}. \tag{5.43}$$

Now we get four independent relationships (4.16) and (5.40) between the parameters θ^b, θ^i, V, v^b, v^u and v^i, so the result of the theorem is to be expected. In Figure 5.2 we see that the speeds and the intermediate states in the wave sequence (5.42) are determined as follows.

Substituting θ^b from (4.16) into (5.43) and simplifying we obtain the burned gas speed v^b as function of v^i and θ^i:

$$v^b = \frac{1 + q + a(\phi - a\phi\mu - \mu - \mu_g)}{(1 - a\mu)(\theta^i + a\phi)} v^i. \tag{5.44}$$

Next we use (5.44) with the equations for v^b from (4.16) in order to obtain the combustion wave speed V as function of v^i and θ^i. Finally, we substitute the resulting V into the first equation in (4.16) and obtain v^u as function of v^i and θ^i. This completes the proof of Theorem 5.1.

5.5   Conclusion

In this chapter we describe an interesting and simple non-diffusive gas-solid co-flow combustion model. We obtain the wave profile and solve the corresponding Riemann problem. Comparing
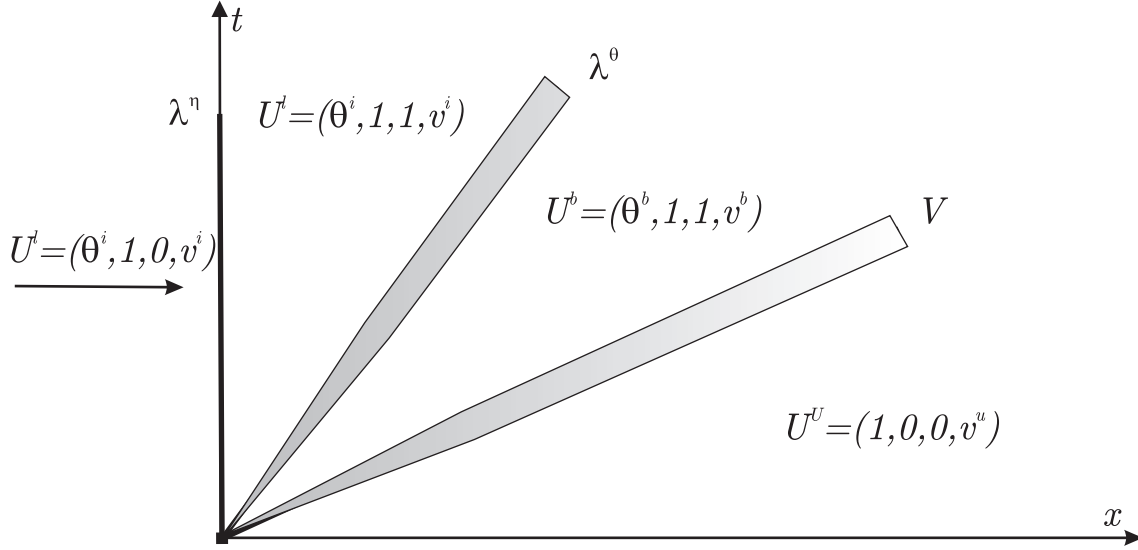
Figure 5.2: Regions separated by immobile, thermal and combustion waves in the Riemann solution. Values of θ, Y, η and v in each region.

these results to the ones obtained previously for the more general model we conclude that the diffusion terms do not affect qualitatively the propagation of the combustion wave.

This property can be generalized in the following way. *Let us assume that it is possible to obtain a traveling wave solution for a system of conservation laws by using the singular perturbation technique as it was done in Chapter 4. In this case the traveling wave solution of the simplified system obtained by neglecting the diffusive terms is a good approximation to the original traveling wave solution.*

The main part of this Chapter was published in [20].

Chapter 6

Numerical methods

6.1   Introduction

When for some reason the explicit solution for the partial differential equations is not obtainable
and we want to understand the behavior of the solution, numerical simulation is the best option.
This is our case: usually, systems of partial differential equations of the Convection-Diffusion-
Reaction type appearing in the physical formulation in Chapter 2 do not have explicit solutions.

Many different numerical methods were developed in order to solve systems of PDEs: Finite
Elements Methods, Boundary Element Methods, Finite Difference Methods and others. As all
the flows we consider in this work are one dimensional, our choice is the Finite Difference
Method.

One of the physical phenomena we want to study is the formation of stable combustion
waves, which may require simulation for long times. Large time steps are required for practical
simulation. Thus we discard all explicit schemes because of CFL condition and focus only on
implicit finite difference schemes with second order accuracy, see [47].

Our main goal here is to simulate numerically the systems of PDEs introduced in Section
2.1 and Chapter 7. In general, they can be written as systems of reaction-convection-diffusion
equations:

$$\frac{\partial}{\partial t}G(W) + \frac{\partial}{\partial x}F(W) = \frac{\partial}{\partial x}\left(H(W)\frac{\partial W}{\partial x}\right) + \Psi(W), \qquad (6.1)$$

depending on the number of equations the model we are simulating possesses the matrix H can
be 4×4 for the model with four equations introduced in Section 2.1, or 3×3 for the simplified
combustion model with three equations that we will introduce in Chapter 7. The vectors W,
G, F, Ψ will be 4×1 or 3×1 respectively.

The system (2.23)-(2.26) with $b = 1$ from Section 2.1 is a particular case of (6.1) with:

$$W = \begin{bmatrix} \theta \\ Y \\ \eta \\ v \end{bmatrix}, \ G = \begin{bmatrix} \theta \\ \phi Y/\theta \\ \phi/\theta \\ \eta \end{bmatrix}, \ F = \begin{bmatrix} av \\ vY/\theta \\ v/\theta \\ 0 \end{bmatrix}, \ H = \begin{bmatrix} 1 & 0 & 0 & 0 \\ 0 & \frac{1}{L_e\theta} & 0 & 0 \\ 0 & 0 & 0 & 0 \\ 0 & 0 & 0 & 0 \end{bmatrix}, \ \Psi = \begin{bmatrix} q \\ -\mu \\ \mu_g \\ 1 \end{bmatrix} \Phi,$$

$$\text{(6.2)}$$

where Φ is given by Arrhenius' law (7.4). The system (7.1)-(7.3) from Chapter 7 is another particular case of (6.1) with

$$W = \begin{bmatrix} T \\ Y \\ \eta \end{bmatrix}, \ G = \begin{bmatrix} T \\ Y \\ \eta \end{bmatrix}, \ F = \begin{bmatrix} aT \\ vY \\ 0 \end{bmatrix}, \ H = \begin{bmatrix} 1 & 0 & 0 \\ 0 & 0 & 0 \\ 0 & 0 & 0 \end{bmatrix}, \ \Psi = \begin{bmatrix} q \\ -\mu \\ -1 \end{bmatrix} \Phi. \quad \text{(6.3)}$$

In this chapter we recall the classical (linear or nonlinear) Crank-Nicolson scheme and show why for the models of the type (2.23)-(2.26) this scheme cannot be applied. Next we introduce the Box scheme and combine it with the Crank-Nicolson scheme to construct two other schemes (called the splitting scheme and the hybrid scheme) which can be used to simulate the models of the type (2.23)-(2.26).

Nonlinear implicit finite difference method require the usage of Newton method in each time step. The detailed analysis of this method, its convergence rate can be found in [26]. For implementation details, see [38].

Notation

We introduce the notation used in this chapter. Following [47], the space direction denoted by x is discretized into M grid points with index $m = 1 \dots M$, where $m = 1$ and $m = M$ correspond to the boundaries of the interval where the calculation takes place. The grid position m corresponds to $x = (m - 1)h$, where h is the grid size. We work with uniform grids (h does not depend on m). Analogously the time is denoted by t with time index denoted by n and the time step is k. However, we consider timestep-adaptative finite difference schemes, so k may change from one grid level to another. Generally we get $k = k(n)$ and the time index n corresponds to $t = \sum_{i=1}^{n} k(i)$.

As all the numerical schemes we analyze are two time levels n and $n+1$ dependent, we simplify the notation and use W_m in place of W_m^n and $\bar{W}_m$ instead of W_m^{n+1}. Another simplification useful for Newton's method is used frequently. The notation $\bar{X}_m^{(l)}$ will mean the iteration l of

Newton's method to find the solution at position m and time $n+1$. There are many functions depending on W evaluated at different grid points. We indicate $F(\bar{W}_m)$ by $\bar{F}_m$, $G(\bar{W}_{m+1}^{(l)})$ by $\bar{G}_{m+1}^{(l)}$ and so on. Finally, the derivatives in W of function F at point $(\bar{W}_m^{(l)})$ is indicated by $(D_W\bar{F})_m^{(l)}$.

6.1.1   Crank-Nicolson method

The Crank-Nicolson finite difference scheme is centered at position $(m, n+1/2)$ and uses a six point discretization, see Figure 6.1 for its stencil. Following [47], we discretize the system (6.1) as:

$$\frac{1}{k}\left(\bar{G}_m - G_m\right) + \frac{1}{4h}\left(\bar{F}_{m+1} - \bar{F}_{m-1} - F_{m-1} + F_{m+1}\right) =$$
$$\frac{1}{4h^2}\left[(\bar{H}_{m+1} + \bar{H}_m)(\bar{W}_{m+1} - \bar{W}_m) - (\bar{H}_m + \bar{H}_{m-1})(\bar{W}_m - \bar{W}_{m-1})\right] +$$
$$\frac{1}{4h^2}\left[(H_{m+1} + H_m)(W_{m+1} - W_m) - (H_m + H_{m-1})(W_m - W_{m-1})\right] +$$
$$\frac{1}{2}\left(\bar{\Psi}_m + \Psi_m\right). \tag{6.4}$$
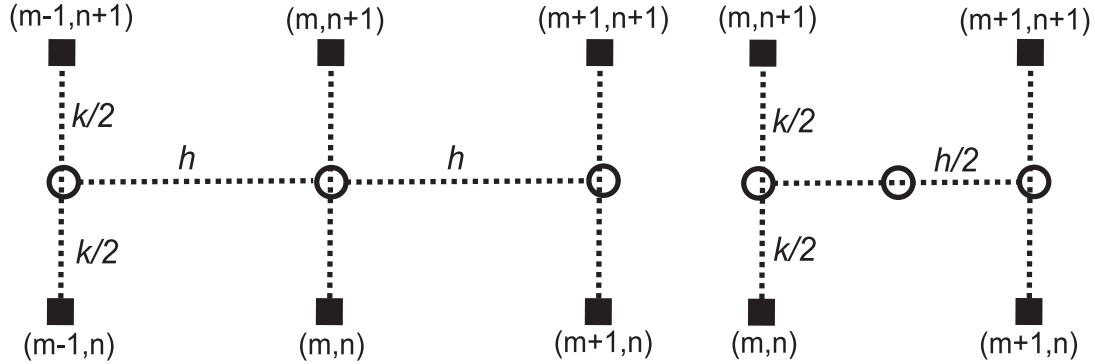
Figure 6.1: Black squares - stencil for the Crank-Nicolson scheme on the left and for the Box scheme on the right. We indicate auxiliary points with circles.

Using $\lambda = k/h$ and $\mu = k/h^2$ we rewrite (6.4):

$$\left(\bar{G}_m - G_m\right) + \frac{\lambda}{4}\left(\bar{F}_{m+1} - \bar{F}_{m-1} - F_{m-1} + F_{m+1}\right) =$$
$$\frac{\mu}{4}\left[(\bar{H}_{m+1} + \bar{H}_m)(\bar{W}_{m+1} - \bar{W}_m) - (\bar{H}_m + \bar{H}_{m-1})(\bar{W}_m - \bar{W}_{m-1})\right] +$$
$$\frac{\mu}{4}\left[(H_{m+1} + H_m)(W_{m+1} - W_m) - (H_m + H_{m-1})(W_m - W_{m-1})\right] +$$
$$\frac{k}{2}\left(\bar{\Psi}_m + \Psi_m\right). \tag{6.5}$$

48

In the general case H, F, G and Ψ are non-linear functions of W. In order to solve these equations we use Newton's method, which consists in linearizing H, F, G and Ψ for the time $(n + 1)$ over an approximate solution $\bar{W}^{(l)}$. The next approximation is defined by $\bar{W}^{(l+1)} = \bar{W}^{(l)} + \Delta W^{(l)}$; we will use $\Delta W^{(l)}$ as the unknown rather than $W^{(l)}$:

$$\bar{G}_m^{(l+1)} = \bar{G}_m^{(l)} + (D_W \bar{G})_m^{(l)} \Delta W_m^{(l)}, \quad \bar{G}_{m+1}^{(l+1)} = \bar{G}_{m+1}^{(l)} + (D_W \bar{G})_{m+1}^{(l)} \Delta W_{m+1}^{(l)}, \tag{6.6}$$

and proceed similarly for F, H and Ψ. In order to simplify notation we will write ΔW instead of $\Delta W^{(l)}$. Linearizing we rewrite (6.5) as:

$$\left(\bar{G}_m^{(l)} + (D_W \bar{G})_m^{(l)} \Delta W_m - G_m \right) +$$
$$\tfrac{\lambda}{4} \left(\bar{F}_{m+1}^{(l)} + (D_W \bar{F})_{m+1}^{(l)} \Delta W_{m+1} - \bar{F}_{m-1}^{(l)} - (D_W \bar{F})_{m-1}^{(l)} \Delta W_{m-1} - F_{m-1} + F_{m+1} \right) =$$
$$\tfrac{\mu}{4} (\bar{H}_{m+1}^{(l)} + (D_W \bar{H})_{m+1}^{(l)} (\Delta W_{m+1}) + \bar{H}_m^{(l)} + (D_W \bar{H})_m^{(l)} (\Delta W_m))$$
$$(\bar{W}_{m+1}^{(l)} + \Delta W_{m+1} - \bar{W}_m^{(l)} - \Delta W_m) -$$
$$\tfrac{\mu}{4} (\bar{H}_m^{(l)} + (D_W \bar{H})_m^{(l)} (\Delta W_m) + \bar{H}_{m-1}^{(l)} + (D_W \bar{H})_{m-1}^{(l)} (\Delta W_{m-1}))$$
$$(\bar{W}_m^{(l)} + \Delta W_m - \bar{W}_{m-1}^{(l)} - \Delta W_{m-1}) +$$
$$\tfrac{\mu}{4} \left[(H_{m+1} + H_m)(W_{m+1} - W_m) - (H_m + H_{m-1})(W_m - W_{m-1}) \right] +$$
$$\tfrac{k}{2} \left(\bar{\Psi}_m^{(l)} + (D_W \bar{\Psi})_m^{(l)} \Delta W_m + \Psi_m \right). \tag{6.7}$$

One has to notice that $D_W \bar{H}$ is a tri-linear form. For example, $(D_W \bar{H})_m^{(l)} (\Delta W_m) \cdot \bar{W}_m^{(l)}$ is a vector, and $(D_W \bar{H})_m^{(l)} (\Delta W_m) \cdot \bar{W}_m^{(l)}$ is written as $\langle (D_W \bar{H})_m^{(l)}, \cdot, \bar{W}_m^{(l)} \rangle \Delta W_m$ when necessary. Using this notation we rewrite the system (6.7) as:

$$\left[-\tfrac{\lambda}{4}(D_W \bar{F})_{m-1}^{(l)} - \tfrac{\mu}{4}(\bar{H}_m^{(l)} + \bar{H}_{m-1}^{(l)}) + \tfrac{\mu}{4}\langle (D_W \bar{H})_{m-1}^{(l)}, \cdot, (\bar{W}_m^{(l)} - \bar{W}_{m-1}^{(l)}) \rangle \right] \Delta W_{m-1} +$$
$$\left[(D_W \bar{G})_m^{(l)} + \tfrac{\mu}{4}(\bar{H}_m^{(l)} + \bar{H}_{m+1}^{(l)} + \bar{H}_m^{(l)} + \bar{H}_{m-1}^{(l)}) - \right.$$
$$\left. \tfrac{\mu}{4}\langle (D_W \bar{H})_m^{(l)}, \cdot, (\bar{W}_{m+1}^{(l)} - 2\bar{W}_m^{(l)} + \bar{W}_{m-1}^{(l)}) \rangle - \tfrac{k}{2}(D_W \bar{\Psi})_m \right] \Delta W_m +$$
$$\left[\tfrac{\lambda}{4}(D_W \bar{F})_{m+1}^{(l)} - \tfrac{\mu}{4}(\bar{H}_m^{(l)} + \bar{H}_{m+1}^{(l)}) - \tfrac{\mu}{4}\langle (D_W \bar{H})_{m+1}^{(l)}, \cdot, (\bar{W}_{m+1}^{(l)} - \bar{W}_m^{(l)}) \rangle \right] \Delta W_{m+1} = \tag{6.8}$$
$$-(\bar{G}_m^{(l)} - G_m) - \tfrac{\lambda}{4}(\bar{F}_{m+1}^{(l)} - \bar{F}_{m-1}^{(l)} + F_{m+1} - F_{m-1}) +$$
$$\tfrac{\mu}{4} \left[(\bar{H}_{m+1}^{(l)} + \bar{H}_m^{(l)})(\bar{W}_{m+1}^{(l)} - \bar{W}_m^{(l)}) - (\bar{H}_m^{(l)} + \bar{H}_{m-1}^{(l)})(\bar{W}_m^{(l)} - \bar{W}_{m-1}^{(l)}) \right] +$$
$$\tfrac{\mu}{4} \left[(H_{m+1} + H_m)(W_{m+1} - W_m) - (H_m + H_{m-1})(W_m - W_{m-1}) \right] + \tfrac{k}{2} \left[\bar{\Psi}_m^{(l)} + \Psi_m \right].$$

The system (6.8) ia s block tridiagonal linear system of the form:

$$
\begin{bmatrix}
B_2 & C_2 & & & 0 \\
 & \ddots & & & \\
 & A_m & B_m & C_m & \\
 & & \ddots & & \\
0 & & & A_{M-1} & B_{M-1}
\end{bmatrix}_{(M-2)\times(M-2)}
\begin{bmatrix}
\Delta W_2 \\
\vdots \\
\Delta W_m \\
\vdots \\
\Delta W_{M-1}
\end{bmatrix}_{M-2}
=
\begin{bmatrix}
T_2 \\
\vdots \\
T_m \\
\vdots \\
T_{M-1}
\end{bmatrix}_{M-2}.
\qquad (6.9)
$$

Assuming the coefficient matrix is nonsingular, this system can be solved with the method explained in Section 6.1.4 were the blocks are given by:

$$
A_m = \left[-\tfrac{\lambda}{4}(D_W \bar{F})^{(l)}_{m-1} - \tfrac{\mu}{4}(\bar{H}^{(l)}_m + \bar{H}^{(l)}_{m-1}) + \tfrac{\mu}{4}\langle (D_W \bar{H})^{(l)}_{m-1}, \cdot, (\bar{W}^{(l)}_m - \bar{W}^{(l)}_{m-1})\rangle \right], \qquad (6.10)
$$

$$
B_m = \left[(D_W \bar{G})^{(l)}_m + \tfrac{\mu}{4}(\bar{H}^{(l)}_{m-1} + 2\bar{H}^{(l)}_m + \bar{H}^{(l)}_{m+1}) - \right.
$$
$$
\left. \tfrac{\mu}{4}\langle (D_W \bar{H})^{(l)}_m, \cdot, (\bar{W}^{(l)}_{m+1} - 2\bar{W}^{(l)}_m + \bar{W}^{(l)}_{m-1})\rangle - \tfrac{k}{2}(D_W \bar{\Psi})_m \right], \qquad (6.11)
$$

$$
C_m = \left[\tfrac{\lambda}{4}(D_W \bar{F})^{(l)}_{m+1} - \tfrac{\mu}{4}(\bar{H}^{(l)}_m + \bar{H}^{(l)}_{m+1}) - \tfrac{\mu}{4}\langle (D_W \bar{H})^{(l)}_{m+1}, \cdot, (\bar{W}^{(l)}_{m+1} - \bar{W}^{(l)}_m)\rangle \right], \qquad (6.12)
$$

$$
T_m = -(\bar{G}^{(l)}_m - G_m) - \tfrac{\lambda}{4}(\bar{F}^{(l)}_{m+1} - \bar{F}^{(l)}_{m-1} + F_{m+1} - F_{m-1}) +
$$
$$
\tfrac{\mu}{4}\left[(\bar{H}^{(l)}_{m+1} + \bar{H}^{(l)}_m)(\bar{W}^{(l)}_{m+1} - \bar{W}^{(l)}_m) - (\bar{H}^{(l)}_m + \bar{H}^{(l)}_{m-1})(\bar{W}^{(l)}_m - \bar{W}^{(l)}_{m-1}) \right] + \qquad (6.13)
$$
$$
\tfrac{\mu}{4}\left[(H_{m+1} + H_m)(W_{m+1} - W_m) - (H_m + H_{m-1})(W_m - W_{m-1}) \right] + \tfrac{k}{2}\left[\bar{\Psi}^{(l)}_m + \Psi_m \right].
$$

The terms T_2 and T_{M-1} are a somewhat different: in order to obtain T_2 one has to substitute W_1, H_1 by W_l, H_l and for T_{M-1} one has to substitute W_M, H_M by W_r, H_r respectively. The terms W_1, H_1 and W_r, H_r are left and right Dirichlet boundary conditions.

Newton's method is applied to the system (6.9) until $||\Delta W|| < \epsilon_C/||W||$, where ϵ_C is a tolerance value; here we use the Euclidean norm $||\cdot||$.

Stability and accuracy

Usually, it is difficult to show stability of finite difference schemes for non-linear systems. In [47] it was shown that Crank-Nicolson scheme is stable when applied to certain linear partial differential equations with constant coefficients. One has to notice that is not our case. Also in [47] one can find that this scheme has second order of accuracy in space and in time.

6.1.2 Box scheme

As it will be shown in Section 6.2, the classical Crank-Nicolson scheme as described in Section 6.1.1 cannot be applied to the system (2.23)-(2.26) because of the nature of equation (2.25) in the context of whole system. We are saying that v is not an evolutionary variable, i.e., the equation we have for v does not provide its time derivative. The ensuing difficulty is explained in detail in Section 6.2.1. To solve this difficulty, we use the second order accuracy Box scheme for the following kind of equation, see [33, 42]:

$$\frac{\partial}{\partial t}G(W) + \frac{\partial}{\partial x}F(W) = \Psi(W). \tag{6.14}$$

For the solution of the equation (6.14) we will use an implicit box scheme centered at the point $(m + 1/2, n + 1/2)$, see Figure 6.1, right. This scheme can be solved almost explicitly. Following the notation introduced in Section 6.1 and taking into account the right stencil in Figure 6.1 we see that (6.14) at position $(m + 1/2, n + 1/2)$ can be approximated by:

$$\frac{1}{2}\left(\left.\frac{\partial G(W)}{\partial t}\right|_m^{n+1/2} + \left.\frac{\partial G(W)}{\partial t}\right|_{m+1}^{n+1/2} \right) + \frac{1}{2}\left(\left.\frac{\partial F(W)}{\partial x}\right|_{m+1/2}^n + \left.\frac{\partial F(W)}{\partial x}\right|_{m+1/2}^{n+1} \right) = $$
$$= \frac{1}{4}\left(\left.\Psi\right|_m^n + \left.\Psi\right|_{m+1}^n + \left.\Psi\right|_m^{n+1} + \left.\Psi\right|_{m+1}^{n+1} \right). \tag{6.15}$$

Approximating the derivatives we obtain a second order accuracy scheme:

$$\frac{1}{2k}\left(\bar{G}_m + \bar{G}_{m+1} - G_m - G_{m+1} \right) + \frac{1}{2h}\left(\bar{F}_{m+1} - \bar{F}_m - F_m + F_{m+1} \right) = $$
$$\frac{1}{4}\left(\bar{\Psi}_{m+1} + \bar{\Psi}_m + \Psi_m + \Psi_{m+1} \right). \tag{6.16}$$

Looking at Figure 6.1 one realizes that the system (6.16) with boundary conditions at the left can be solved at time level $(n + 1)$ from left to right. That is why we construct Newton's method for solving system (6.16) at the point $(m + 1, n + 1)$. The iteration using Newton's method is analogous to that presented in Section 6.1.1, i.e., $\bar{W}^{(l+1)} = \bar{W}^{(l)} + \Delta W$; we start the iteration with $\bar{W}_{m+1}^{(0)} = W_{m+1}$. Let us assume that we know the iterate solution $\bar{W}_{m+1}^l$ for time $(n + 1)$ and the solution $\bar{W}_m$ at $(m, n + 1)$, then we can linearize the equation (6.16) around $\bar{W}_{m+1}^{(l)}$, obtaining:

$$\frac{1}{2k}\left(\bar{G}_m + \bar{G}_{m+1}^{(l)} + (D_W\bar{G})_{m+1}^{(l)}\Delta W_{m+1} - G_m - G_{m+1} \right) + $$
$$\frac{1}{2h}\left(\bar{F}_{m+1}^{(l)} + (D_W\bar{F})_{m+1}^{(l)}\Delta W_{m+1} - \bar{F}_m - F_m + F_{m+1} \right) = \tag{6.17}$$
$$\frac{1}{4}\left(\bar{\Psi}_{m+1}^{(l)} + (D_W\bar{\Psi})_{m+1}^{(l)}\Delta W_{m+1} + \bar{\Psi}_m + \Psi_m + \Psi_{m+1} \right).$$

System (6.17) can be rewritten as follows, with $\lambda = k/h$:

$$\left((D_W \bar{G})^{(l)}_{m+1} + \lambda (D_W \bar{F})^{(l)}_{m+1} - \tfrac{k}{2}(D_W \bar{\Psi})^{(l)}_{m+1} \right) \Delta W_{m+1} = \tfrac{k}{2}\left(\bar{\Psi}^{(l)}_{m+1} + \bar{\Psi}_m + \Psi_m + \Psi_{m+1} \right)$$

$$- \left(\bar{G}_m + \bar{G}^{(l)}_{m+1} - G_m - G_{m+1} \right) - \lambda \left(\bar{F}^{(l)}_{m+1} - \bar{F}_m - F_m + F_{m+1} \right).$$

(6.18)

We emphasize that the Box scheme is valid only if the left boundary condition is given. In such a case it is implicit, however it can be solved by solving many small systems, so it is computationally advantageous.

In [33], general stability of this scheme for linear equation is proved and some implementation particularities are discussed. A more detailed discussion of application of the Box scheme to system (6.14) can be found in [34].

6.1.3 Boundary conditions

In this section we show two possibilities for boundary conditions and discuss it implementation. In our simulations we need to use both Dirichlet and Neumann boundary conditions.

Dirichlet B.C.

The Dirichlet condition consists in defining the value of the depending variable on the boundary. Numerically for the system of the form (6.1) or (6.14) this condition corresponds to:

$$W(x_1) = W_L; \quad W(x_M) = W_R,$$

(6.19)

where W_L and W_R are given values. Thus we have $M - 2$ unknowns and thus at each Newton's iteration we need to solve the linear system of $M - 2$ equations, where the boundary conditions will appear only in the first and the last blocks of the block matrix in Newton's method (6.9).

Neumann B.C.

The Neumann boundary condition consists of defining flow condition at the boundary of the domain of interest (e.g at the points x_1 and x_M). For the one-dimensional numerical schemes it will be

$$\frac{\partial W}{\partial x}(x_1) = \dot{W}_L; \quad \frac{\partial W}{\partial x}(x_M) = \dot{W}_R,$$

where $\dot{W}_L$ and $\dot{W}_R$ are given values. In order to use Neumann boundary conditions numerically we use the **ghost point method**. It consists of creating one ghost (fictitious) point for each

boundary, indicated by x_0 at the left and x_{M+1} at the right. Now we calculate the value of $W(x_0)$ and $W(x_{M+1})$ at each time step so that the discretization gives the value of derivatives automatically. For example, if we use the Crank-Nicolson scheme the derivatives are, with second order accuracy:

$$\frac{\partial W}{\partial x}(x_1) = \frac{W(x_2) - W(x_0)}{2h} = \dot{W}_L; \quad \frac{\partial W}{\partial x}(x_M) = \frac{W(x_{M+1}) - W(x_{M-1})}{2h} = \dot{W}_R. \quad (6.20)$$

Thus the function value at the ghost point x_{M+1} is $W(x_{M+1}) = 2h\dot{W}_R + W(x_{M-1})$. The procedure for the point x_0 is analogous. This method is easy to implement because in Newton's method we can use the same matrices as for Dirichlet boundary conditions. The only difference will be the dimension of the problem, which is M instead of $M - 2$.

Finally one has to notice that the same problem can use different boundary conditions for the left and right sides.

6.1.4 Solution of the block tridiagonal system

We will apply the standard LU decomposition to solve the following system with the assumption that $\det B_m \neq 0$ for $m = 1, 2, \ldots, M$,

$$\begin{bmatrix} B_1 & C_1 & 0 & \cdots & 0 \\ A_2 & B_2 & C_2 & \cdots & 0 \\ 0 & \ddots & \ddots & \ddots & \vdots \\ 0 & \cdots & A_{M-1} & B_{M-1} & C_{M-1} \\ 0 & \cdots & 0 & A_M & B_M \end{bmatrix} \begin{bmatrix} X_1 \\ \vdots \\ \vdots \\ X_M \end{bmatrix} = \begin{bmatrix} T_1 \\ \vdots \\ \vdots \\ T_M \end{bmatrix}. \quad (6.21)$$

This system is equivalent to:

$$\begin{bmatrix} \bar{B}_1 & C_1 & 0 & \cdots & 0 \\ 0 & \bar{B}_2 & C_2 & \cdots & 0 \\ 0 & \ddots & \ddots & \ddots & \vdots \\ 0 & \cdots & 0 & \bar{B}_{M-1} & C_{M-1} \\ 0 & \cdots & 0 & 0 & \bar{B}_M \end{bmatrix} \begin{bmatrix} X_1 \\ \vdots \\ \vdots \\ X_M \end{bmatrix} = \begin{bmatrix} \bar{T}_1 \\ \vdots \\ \vdots \\ \bar{T}_M \end{bmatrix}, \quad (6.22)$$

where

$$\bar{B}_1 = B_1, \quad \bar{T}_1 = T_1, \quad (6.23)$$

and for $1 < m < M$:

$$\bar{B}_m = B_m - A_m \bar{B}_{m-1}^{-1} C_{m-1}, \quad \bar{T}_m = T_m - A_m \bar{B}_{m-1}^{-1} T_{m-1}. \quad (6.24)$$

The system (6.22) can be solved by backward substitution:

$$\bar{B}_M X_M = \bar{T}_M, \tag{6.25}$$

and for $1 < m < M$ we have:

$$\bar{B}_m X_m = \bar{T}_m - C_{m-1} \bar{T}_{m-1}. \tag{6.26}$$

6.2 Limitations of the Crank-Nicolson scheme

In this section we explain why the Crank-Nicolson scheme cannot be applied directly to the system of equations (2.23)-(2.26). In the next section we propose an alternative scheme for this system.

6.2.1 Application to the physical model

In order to apply the Crank-Nicolson scheme to the system (2.23)-(2.26) we need to find the blocks A_m, B_m and C_m given in (6.10)-(6.13) with W, G, F, H and Ψ from (6.2). The derivatives $D_W G$ and $D_W F$ are:

$$D_W G = \begin{bmatrix} 1 & 0 & 0 & 0 \\ -\phi Y/\theta^2 & \phi/\theta & 0 & 0 \\ -\phi/\theta^2 & 0 & 0 & 0 \\ 0 & 0 & 1 & 0 \end{bmatrix}, \quad D_W F = \begin{bmatrix} 0 & 0 & 0 & a \\ -vY/\theta^2 & v/\theta & 0 & Y/\theta \\ -v/\theta^2 & 0 & 0 & 1/\theta \\ 0 & 0 & 0 & 0 \end{bmatrix}. \tag{6.27}$$

The derivative of H is a trilinear form, so we can obtain a formula when it is applied on a vector $U = (U_1, U_2, U_3, U_4)^T$:

$$\langle D_W H, V, U \rangle = \begin{bmatrix} 0 & 0 & 0 & 0 \\ 0 & -\frac{1}{L_e \theta^2} V_1 & 0 & 0 \\ 0 & 0 & 0 & 0 \\ 0 & 0 & 0 & 0 \end{bmatrix} \begin{bmatrix} U_1 \\ U_2 \\ U_3 \\ U_4 \end{bmatrix} = \begin{bmatrix} 0 & 0 & 0 & 0 \\ -\frac{1}{L_e \theta^2} U_2 & 0 & 0 & 0 \\ 0 & 0 & 0 & 0 \\ 0 & 0 & 0 & 0 \end{bmatrix} \begin{bmatrix} V_1 \\ V_2 \\ V_3 \\ V_4 \end{bmatrix}, \tag{6.28}$$

where $V = (V_1, V_2, V_3, V_4)^T$, so we will use the notation $\langle D_W H, \cdot, U \rangle$ to mean

$$\langle D_W H, \cdot, U \rangle = \begin{bmatrix} 0 & 0 & 0 & 0 \\ -\frac{1}{L_e \theta^2} U_2 & 0 & 0 & 0 \\ 0 & 0 & 0 & 0 \\ 0 & 0 & 0 & 0 \end{bmatrix}. \tag{6.29}$$

Substituting (6.2) and (6.27)-(6.29) into (6.10)-(6.13) we obtain:

$$A_m = \begin{bmatrix} -\frac{\mu}{2} & 0 & 0 & \frac{\lambda a}{4} \\ \frac{\lambda v_{m-1}^{(l)} Y_{m-1}^{(l)}}{4(\theta_{m-1}^{(l)})^2} - \frac{\mu(Y_m^{(l)}-Y_{m-1}^{(l)})}{4L_e(\theta_{m-1}^{(l)})^2} & \frac{-\lambda v_{m-1}^{(l)}}{4(\theta_{m-1}^{(l)})^2} - \frac{\mu}{4L_e}\left(\frac{1}{\theta_m^{(l)}}+\frac{1}{\theta_{m-1}^{(l)}}\right) & 0 & \frac{-\lambda Y_{m-1}^{(l)}}{4\theta_{m-1}^{(l)}} \\ \frac{\lambda v_{m-1}^{(l)}}{4(\theta_{m-1}^{(l)})^2} & 0 & 0 & \frac{-\lambda}{4\theta_{m-1}^{(l)}} \\ 0 & 0 & 0 & 0 \end{bmatrix}, \qquad (6.30)$$

$$B_m = \begin{bmatrix} 1+\mu & 0 & 0 & 0 \\ B_{11} & B_{12} & 0 & 0 \\ -\frac{\phi}{(\theta_m^{(l)})^2} & 0 & 0 & 0 \\ 0 & 0 & 1 & 0 \end{bmatrix} - \frac{k\alpha e^{-\gamma/\theta^{(l)}}}{2}\begin{bmatrix} \frac{qY(1-\eta)\gamma}{\theta^2} & q(1-\eta) & -qY & 0 \\ -\frac{\mu Y(1-\eta)}{\theta^2} & -\mu(1-\eta) & -\mu Y & 0 \\ \frac{\mu_g Y(1-\eta)}{\theta^2} & \mu_g(1-\eta) & \mu_g Y & 0 \\ \frac{Y(1-\eta)}{\theta^2} & (1-\eta) & -Y & 0 \end{bmatrix}^{(l)}_m, \qquad (6.31)$$

where

$$B_{11} = -\frac{\phi Y_m^{(l)}}{(\theta_m^{(l)})^2} + \frac{\mu(Y_{m-1}^{(l)} - 2Y_m^{(l)} + Y_{m+1}^{(l)})}{4L_e(\theta_m^{(l)})^2}, \quad B_{12} = \frac{\phi}{\theta_m^{(l)}} + \frac{\mu}{4L_e}\left(\frac{1}{\theta_{m-1}^{(l)}} + \frac{2}{\theta_m^{(l)}} + \frac{1}{\theta_{m+1}^{(l)}}\right), \quad (6.32)$$

$$C_m = \begin{bmatrix} -\frac{\mu}{2} & 0 & 0 & \frac{\lambda a}{4} \\ -\frac{\lambda v_{m+1}^{(l)} Y_{m+1}^{(l)}}{4(\theta_{m+1}^{(l)})^2} + \frac{\mu(Y_{m+1}^{(l)}-Y_m^{(l)})}{4L_e(\theta_{m+1}^{(l)})^2} & \frac{\lambda v_{m+1}^{(l)}}{4\theta_{m+1}^{(l)}} - \frac{\mu}{4L_e}\left(\frac{1}{\theta_m^{(l)}}+\frac{1}{\theta_{m+1}^{(l)}}\right) & 0 & \frac{\lambda Y_{m+1}^{(l)}}{4\theta_{m+1}^{(l)}} \\ -\frac{\lambda v_{m+1}^{(l)}}{4(\theta_{m+1}^{(l)})^2} & 0 & 0 & \frac{\lambda}{4\theta_{m+1}^{(l)}} \\ 0 & 0 & 0 & 0 \end{bmatrix}. \qquad (6.33)$$

Also

$$T_m = \begin{bmatrix} \theta_m - \theta_m^{(l)} \\ \phi\left(\frac{Y_m}{\theta_m} - \frac{Y_m^{(l)}}{\theta_m^{(l)}}\right) \\ \phi\left(\frac{1}{\theta_m} - \frac{1}{\theta_m^{(l)}}\right) \\ \eta_m - \eta_m^{(l)} \end{bmatrix} - \frac{\lambda}{4}\begin{bmatrix} a(v_{m+1}^{(l)} - v_{m-1}^{(l)} + v_{m+1} - v_{m-1}) \\ \left(\frac{v_{m+1}^{(l)}Y_{m+1}^{(l)}}{\theta_{m+1}^{(l)}}\right) - \left(\frac{v_{m-1}^{(l)}Y_{m-1}^{(l)}}{\theta_{m-1}^{(l)}}\right) + \left(\frac{v_{m+1}Y_{m+1}}{\theta_{m+1}}\right) - \left(\frac{v_{m-1}Y_{m-1}}{\theta_{m-1}}\right) \\ \left(\frac{v}{\theta}\right)_m + \left(\frac{v}{\theta}\right)_{m+1} \\ 0 \end{bmatrix} + $$
$$\frac{k}{2}\begin{bmatrix} q \\ -\mu \\ \mu_g \\ 1 \end{bmatrix}(\bar{\Phi}_m^{(l)} + \Phi_m) + \frac{\mu}{4}\begin{bmatrix} T_1 \\ T_2 \\ 0 \\ 0 \end{bmatrix}, \qquad (6.34)$$

where

$$T_1 = 2(\theta_{m-1} - 2\theta_m + \theta_{m+1}) + 2(\theta_{m-1}^{(l)} - 2\theta_m^{(l)} + \theta_{m+1}^{(l)}), \qquad (6.35)$$

$$T_2 = \frac{1}{L_e} \left(\frac{1}{\theta_{m+1}} + \frac{1}{\theta_m} \right) (Y_{m+1} - Y_m) - \left(\frac{1}{\theta_m} + \frac{1}{\theta_{m+1}} \right) (Y_m - Y_{m-1}) +$$
$$\frac{1}{L_e} \left(\frac{1}{\theta_{m+1}} + \frac{1}{\theta_m} \right)^{(l)} (Y_{m+1} - Y_m)^{(l)} - \left(\frac{1}{\theta_m} + \frac{1}{\theta_{m+1}} \right)^{(l)} (Y_m - Y_{m-1})^{(l)}. \tag{6.36}$$

Now we notice that the last column of the matrix B_m in (6.31) vanishes, so B_m is singular and the methods described in Section 6.1.4 cannot be applied here. This problem occurs because the original system (2.23)-(2.26) is not "complete" as a system of conservation laws, i.e., there is no time evolution term for v. We believe this problem cannot be circumvented by considering other finite difference schemes similar to the Crank-Nicolson scheme.

6.3   The hybrid finite difference scheme

In this section we describe a numerical method for the solution of the system (2.23)-(2.26). The solution of this system through finite differences presents two difficulties.

First, we need to obtain the long time profile of the combustion wave, which can take a long simulation time to form. Explicit schemes can only use very small time steps because of the CFL restriction. Implicit schemes allow for larger time steps and may be unconditionally stable, but are computationally more expensive. As the quality of the solution is tied to its stability, we choose to solve the system implicitly. We avoided making any compromise between speed and accuracy by performing our simulations using a high performance parallel solver for the large linear systems to be solved, see details in [28].

Second, the system (2.23)-(2.26) does not possess any evolution term for the variable v, which represents the gas speed. This particularity does not allow the usage of any implicit symmetric three-point finite difference scheme, such as Crank–Nicolson, as has been shown in Section 6.2. The equation (2.25) requires the Box scheme.

Instead of using the Box scheme on the whole system, we can use a hybrid scheme which consists in applying the Crank–Nicolson discretization on equations (2.23), (2.24), (2.26) and the Box discretization on (2.25). The resulting scheme is fully implicit.

The notation used in this section is different from that used in the rest of this chapter. This is so because here we follow the notation used in the documentation of the software for simulations of systems similar to (2.23)-(2.26) developed in the Fluid Dynamics Laboratory at IMPA [29]. We apologize to the reader for the inconvenience.

The equations (2.23), (2.24) and (2.26) can be written as a system of three equations of the

form:

$$\frac{\partial h(u)}{\partial t} + \frac{\partial f(u)}{\partial x} = \frac{\partial}{\partial x}\left(g(u)\frac{\partial u}{\partial x}\right) + q(u), \tag{6.37}$$

where the 4-component variable u and the functions h, f, g, h are equivalent to the variable W and functions G, F, H, Ψ from (6.1) respectively. On the other hand, equation (2.25) can be written as:

$$\frac{\partial \tilde{h}(u)}{\partial t} + \frac{\partial \tilde{f}(u)}{\partial x} = \tilde{q}(u). \tag{6.38}$$

We denote with tilde the function that follow the Box scheme discretization, and functions without tilde follows the Crank-Nicolson discretization. So for (6.37), we use the Crank-Nicolson discretization analogous to (6.4):

$$\frac{h_i^{n+1}}{k} + \frac{f_{i+1}^{n+1} - f_{i-1}^{n+1}}{4h} -$$

$$\frac{1}{4h^2}\left((g_{i+1}^{n+1} + g_i^{n+1})u_{i+1}^{n+1} - (g_{i+1}^{n+1} + 2g_i^{n+1} + g_i^{n+1})u_i^{n+1} + (g_i^{n+1} + g_{i-1}^{n+1})u_{i-1}^{n+1}\right) - \frac{q_i^{n+1}}{2}$$

$$= \frac{h_i^n}{k} - \frac{f_{i+1}^n - f_{i-1}^n}{4h} +$$

$$\frac{1}{4h^2}\left((g_{i+1}^n + g_i^n)u_{i+1}^n - (g_{i+1}^n + 2g_i^n + g_i^n)u_i^n + (g_i^n + g_{i-1}^n)u_{i-1}^n\right) + \frac{q_i^n}{2}. \tag{6.39}$$

For (6.38), we use the Box scheme analogous to (6.16):

$$\frac{\tilde{h}_{i+1}^{n+1} + \tilde{h}_i^{n+1}}{2k} + \frac{\tilde{f}_{i+1}^{n+1} - \tilde{f}_i^{n+1}}{2h} - \frac{q_{i+1}^{n+1} + q_i^{n+1}}{4} = \frac{\tilde{h}_{i+1}^n + \tilde{h}_i^n}{2k} - \frac{\tilde{f}_{i+1}^n - \tilde{f}_i^n}{2h} + \frac{\tilde{q}_{i+1}^n + \tilde{q}_i^n}{4}. \tag{6.40}$$

We group the LHS and RHS terms into the functions $\mathcal{F}$ (corresponding to time step $n+1$) and y (corresponding to time step n) respectively, obtaining:

$$\mathcal{G} = 0, \tag{6.41}$$

where

$$\mathcal{G}(u_1^n, \ldots, u_M^n, u_1^{n+1}, \ldots, u_M^{n+1}) \equiv \mathcal{F}(u_1^{n+1}, \ldots, u_M^{n+1}) - y(u_1^n, \ldots, u_M^n). \tag{6.42}$$

Now Newton's method for solving the problem (6.41) can be written in the form analogous to (6.9) with δu corresponding to ΔW as:

$$u^{(l+1)} = u^{(l)} + \delta u, \quad \text{where} \quad \left[\frac{\partial \mathcal{G}(u)}{\partial u}\right]_{u^{(l)}} \delta u = -\mathcal{G}(u^{(l)}). \tag{6.43}$$

We need to calculate the matrix $\frac{\partial \mathcal{G}(u)}{\partial u}$. Inspecting (6.39)-(6.40) we see that it is a system with block tridiagonal form with blocks of 4 lines, see [29] for details. The first three lines of each

block involve the matrices:

$$C_i = \frac{\partial \mathcal{G}_i}{\partial u_{i+1}} = \frac{f'_{i+1}}{4h} - \frac{g'_{i+1}(u_{i+1} - u_i) + g_{i+1} + g_i}{4h^2};$$

$$A_i = \frac{\partial \mathcal{G}_i}{\partial u_i} = \frac{h'_i}{k} - \frac{g'_i(u_{i+1} - 2u_i + u_{i-1}) - g_{i+1} - 2g_i - g_{i-1}}{4h^2} - \frac{q'_i}{2};$$

(6.44)

$$B_i = \frac{\partial \mathcal{G}_i}{\partial u_{i-1}} = -\frac{f'_{i-1}}{4h} - \frac{g'_{i-1}(u_{i-1} - u_i) + g_i + g_{i-1}}{4h^2},$$

where we denote h', f', g' and q' the matrices dh/du, df/du, dg/du and dq/du. The last line of each block has a different form:

$$\tilde{C}_i = \frac{\partial \tilde{\mathcal{G}}_i}{\partial u_{i+1}} = \frac{\tilde{h}'_{i+1}}{2k} + \frac{\tilde{f}'_{i+1}}{2h} - \frac{\tilde{q}'_{i+1}}{4};$$

$$\tilde{A}_i = \frac{\partial \tilde{\mathcal{G}}_i}{\partial u_i} = \frac{\tilde{h}'_i}{2k} - \frac{\tilde{f}'_i}{2h} - \frac{\tilde{q}'_i}{4};$$

(6.45)

$$\tilde{B}_i = \frac{\partial \tilde{\mathcal{G}}_i}{\partial u_{i-1}} = 0.$$

All the blocks are calculated for the generic l-th iteration of Newton's method to obtain the solution at time step (n+1). For the system (2.23)-(2.25) we recall that:

$$u = \begin{bmatrix} \theta \\ Y \\ \eta \\ v \end{bmatrix}, \ h = \begin{bmatrix} \theta \\ \phi Y/\theta \\ \eta \\ \phi/\theta \end{bmatrix}, \ f = \begin{bmatrix} av \\ vY/\theta \\ 0 \\ v/\theta \end{bmatrix}, \ g = \begin{bmatrix} 1 & 0 & 0 & 0 \\ 0 & \frac{1}{L_e\theta} & 0 & 0 \\ 0 & 0 & 0 & 0 \\ 0 & 0 & 0 & 0 \end{bmatrix}, \ q = \begin{bmatrix} q \\ -\mu \\ 1 \\ \mu_g \end{bmatrix} \Phi. \ (6.46)$$

If we put the line numbers as $[\cdot]$, schematically the blocks A, B and C will be:

$$C_i = \begin{bmatrix} \cdots & C_i^{[1]} & \cdots \\ \cdots & C_i^{[2]} & \cdots \\ \cdots & C_i^{[3]} & \cdots \\ \cdots & \tilde{C}_i^{[4]} & \cdots \end{bmatrix}, \quad A_i = \begin{bmatrix} \cdots & A_i^{[1]} & \cdots \\ \cdots & A_i^{[2]} & \cdots \\ \cdots & A_i^{[3]} & \cdots \\ \cdots & \tilde{A}_i^{[4]} & \cdots \end{bmatrix}, \quad B_i = \begin{bmatrix} \cdots & B_i^{[1]} & \cdots \\ \cdots & B_i^{[2]} & \cdots \\ \cdots & B_i^{[3]} & \cdots \\ \cdots & \tilde{B}_i^{[4]} & \cdots \end{bmatrix},$$

where the indices [1], [2], [3] corresponds to each of the three lines in (6.44) and the index [4] correspond to (6.45).

6.3.1 Inicialization particularities

Equation (2.25) has to be taken into account to initialize the variable v at time zero. In this section, we show a simple way to initialize the variable v using a one time step discretization.

For example, we can use a central-space forward-time scheme. In this case equation (2.25) gives:

$$\frac{\phi}{k}\left(\frac{1}{\theta_m^1} - \frac{1}{\theta_m^0}\right) + \frac{1}{2h}\left(\frac{v_{m+1}^0}{\theta_{m+1}^0} - \frac{v_{m-1}^0}{\theta_{m-1}^0}\right) = \mu_g \Phi_m^0. \tag{6.47}$$

Assuming that the temperature at the first time step do not change much we consider $\theta_m^1 = \theta_m^0$, obtaining:

$$\frac{v_{m+1}^0}{\theta_{m+1}^0} - \frac{v_{m-1}^0}{\theta_{m-1}^0} = 2h\mu_g \Phi_m^0 = 2h\mu_g \alpha Y_m^0 (1 - \eta_m^0) \exp(-\gamma/\theta_m^0). \tag{6.48}$$

Thus, we can initialize v^0 to be compatible with the data θ^0, Y^0 and η^0 as functions of x.

6.3.2 Application to the physical model

In the current version of software the function $g(u)$ in (6.37) corresponding to the viscosity term has to be constant. Fortunately the only component of g that is not constant for the model we are considering corresponds to the term $g_{2,2} = \rho/L_e$. Using (2.20) we transform it into $g_{2,2} = 1/(\theta L_e)$. As the function θ varies in small interval $1 < \theta < \theta^b$, in our simulations we use $1/(\theta^b L_e) \leq g_{2,2} \leq 1/(L_e)$. We made simulations for $g_{2,2}$ equal to the maximum and the minimum value in the previous inequality. Since the results of these simulations were visually indistinguishable we make $g_{2,2}$ constant, corresponding to $\theta = (1 + \theta^b)/2$.

As explained, we consider $g' = 0$ and $g_i = g_{i+1} = g_{i-1} = g$. Thus for the lines $r = 1, 2, 3$ (corresponding to (2.23), (2.24), (2.26)):

$$C_i^{[r]} = \frac{f_{i+1}^{[r]'}}{4h} - \frac{g^{[r]}}{2h^2}; \qquad A_i^{[r]} = \frac{h_i^{[r]'}}{k} - \frac{q_i^{[r]'}}{2}; \qquad B_i^{[r]} = -\frac{f_{i-1}^{[r]'}}{4h} - \frac{g^{[r]}}{2h^2}. \tag{6.49}$$

For the line 4 (corresponding to (2.25)):

$$C_i^{[4]} = \frac{h_{i+1}^{[4]'}}{2k} + \frac{f_{i+1}^{[4]'}}{2h} - \frac{q_{i+1}^{[4]'}}{4}; \qquad A_i^{[4]} = \frac{h_i^{[4]'}}{2k} - \frac{f_i^{[4]'}}{2h} - \frac{q_i^{[4]'}}{4}; \qquad B_i^{[4]} = 0. \tag{6.50}$$

The matrices used above are:

$$h' = \begin{bmatrix} 1 & 0 & 0 & 0 \\ -\phi Y/\theta^2 & \phi/\theta & 0 & 0 \\ -\phi/\theta^2 & 0 & 0 & 0 \\ 0 & 0 & 1 & 0 \end{bmatrix}, \quad f' = \begin{bmatrix} 0 & 0 & 0 & a \\ -vY/\theta^2 & v/\theta & 0 & Y/\theta \\ -v/\theta^2 & 0 & 0 & 1/\theta \\ 0 & 0 & 0 & 0 \end{bmatrix}. \tag{6.51}$$

For the combustion rate we use $\Upsilon = \alpha \exp(-\gamma/\theta)$ (then $\Phi = Y(1 - \eta)\Upsilon$):

$$q' = \begin{bmatrix} q\gamma(1-\eta)Y/\theta^2 & q(1-\eta) & -qY & 0 \\ -\mu\gamma(1-\eta)Y/\theta^2 & -\mu(1-\eta) & \mu Y & 0 \\ \gamma(1-\eta)Y/\theta^2 & (1-\eta) & -Y & 0 \\ \mu_g\gamma(1-\eta)Y/\theta^2 & \mu_g(1-\eta) & -\mu_g Y & 0 \end{bmatrix} \Upsilon. \tag{6.52}$$

For y, in Newton's method all functions are calculated at the time n, we use the equation (6.53) for $r = 1, 2, 3$ and the equation (6.54) for $r = 4$:

$$y^{[r]} = \frac{h_i^{[r]}}{k} - \frac{f_{i+1}^{[r]} - f_{i-1}^{[r]}}{4h} + \frac{q_i^{[r]}}{2}, \tag{6.53}$$

$$y^{[3]} = \frac{\tilde{h}_{i+1}^{[4]} + \tilde{h}_i^{[4]}}{2k} - \frac{\tilde{f}_{i+1}^{[4]} - \tilde{f}_i^{[4]}}{2h} + \frac{\tilde{q}_{i+1}^{[4]} + \tilde{q}_i^{[4]}}{4}. \tag{6.54}$$

Our simulations for the parameter values taken from Table 2.3 can be seen in Figures 6.2 and 6.3. Notice that for this choice of parameter values we are inside the region where ϵ is small as plotted in Figure 4.2. We studied the interval $[0, 10^4]$ with 10^3 grid points and the activation energy constant $\gamma = 2.0$. The initial data for the simulation is shown on the left side of Figure 6.2. Figure 6.3 shows the profile of the numerical solution of the system (2.23)-(2.26) at time $t = 2 \cdot 10^7$. We observe the presence of the thermal wave (the small increment in the variable θ corresponding to the temperature near $\xi = 2000$) and the combustion wave. The thermal and combustion waves shown in Figure 6.3 appear in the Riemann solution of the system (2.23)-(2.26) as schematically represented in Figure 5.2. On the right side of Figure 6.2 we show the combustion wave taken from Figure 6.3 on the same scale as the quasi-stationary approximation (4.24). This Figure shows reasonable agreement between the simulated combustion wave and that obtained by using singular perturbation technique. The discrepancy between two waves is not caused by the difference between the zero order approximation and the exact solution because in this case the correction parameter from (4.21) is $\epsilon \approx 10^{-4}$. We speculate that the discrepancy is due to the long time that the solution requires to converge to its traveling form.

The simulation of the system (2.23)-(2.26) with parameter values taken from Table 2.2 for different initial data are plotted in Figures 6.4 and 6.5. In these simulations we use fixed time step length equal to 1, thus the number of time steps indicated in each figure coincides with the dimensionless time of the simulation. Analogously to Figure 6.3 one observes the formation of the thermal and combustion waves.
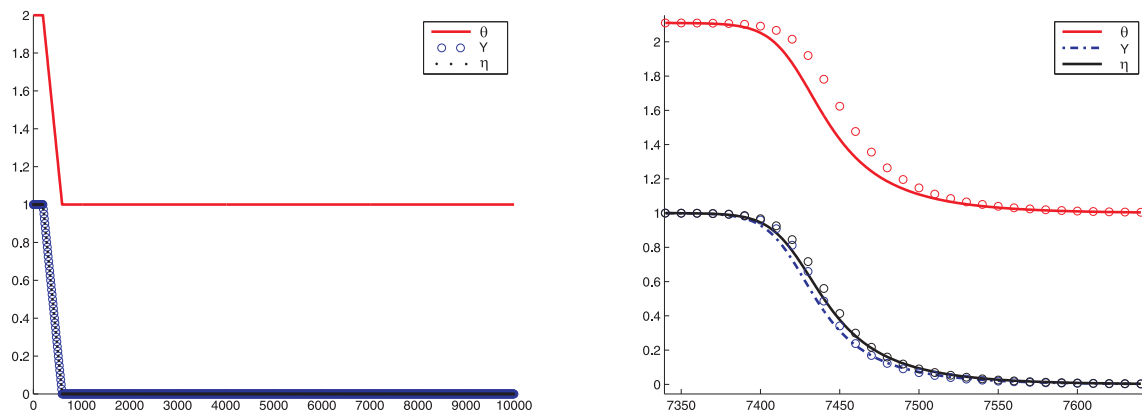
Figure 6.2: In this simulation using the hybrid scheme we use initial data as shown on the left. On the right we compare the combustion wave profile at time $t = 2 \cdot 10^7$ obtained through the numerical simulation from Figure 6.3 (circles) with the semi-analytical one obtained solving (4.24) (lines). Here we use parameter values from Table 2.3.
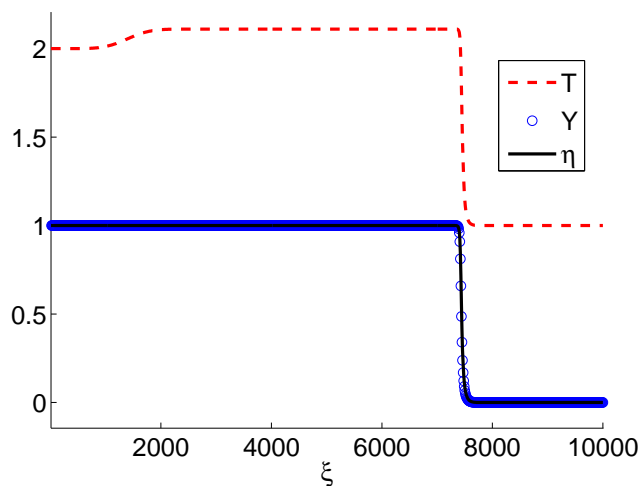
Figure 6.3: Numerical simulation using the hybrid method for system (2.23)-(2.26) at dimensionless time $t = 2 \cdot 10^7$ showing the formation of thermal and combustion waves (Y and η coincide). The initial data is plotted on the left side in Figure 6.2. Here we use parameter values from Table 2.3, except $\gamma = 2$.

61

The parameter θ^b (temperature of the combustion wave) allows an easy comparison between the semi-analytical solution and the numerical simulation. We find its exact value by solving the corresponding Riemann problem, obtained in second equation in (4.16), substituting the parameter values from Table 2.2; it is $\theta^b = 2.0651$. Of course, this value coincides with that obtained by using the zero order approximation as plotted in Figure 4.3 (from the output data we obtain $\theta^b = 2.0651$).

Observing Figures 6.4 and 6.5 one can see that the combustion wave profile requires a long time to stabilize, this is why we performed two simulations. The first one (plotted in Figure 6.4) started with the initial data for the variable θ as 2. This simulation yields a combustion wave temperature equal to 2.069. The second (plotted in Figure 6.4) started with the initial data for the variable θ as 2.5. This simulation yields a combustion wave temperature equal to 2.07. As we see the numerical simulation supports the theoretical result with relative error close to 0.2%.

6.4   Conclusions

In this chapter we developed a hybrid finite difference scheme to solve numerically the system (2.23)–(2.26), which cannot be solved by the Crank-Nicolson scheme.

The combustion wave profile obtained numerically was compared to the zero-order approximation of the analytical solution from Chapter 4 in Figure 6.2 showing good agreement and supporting the usage of singular perturbation method.

The simulations plotted in Figures 6.4 and 6.5 show the formation of the thermal and combustion waves as predicted theoretically through the solution of corresponding Riemann problem illustrated in Figure 5.2. Finally, the value for the combustion temperature θ^b obtained solving the Riemann problem agrees well with the value obtained by numerical simulations.

The results discussed in this Chapter were published in part in [16, 17].
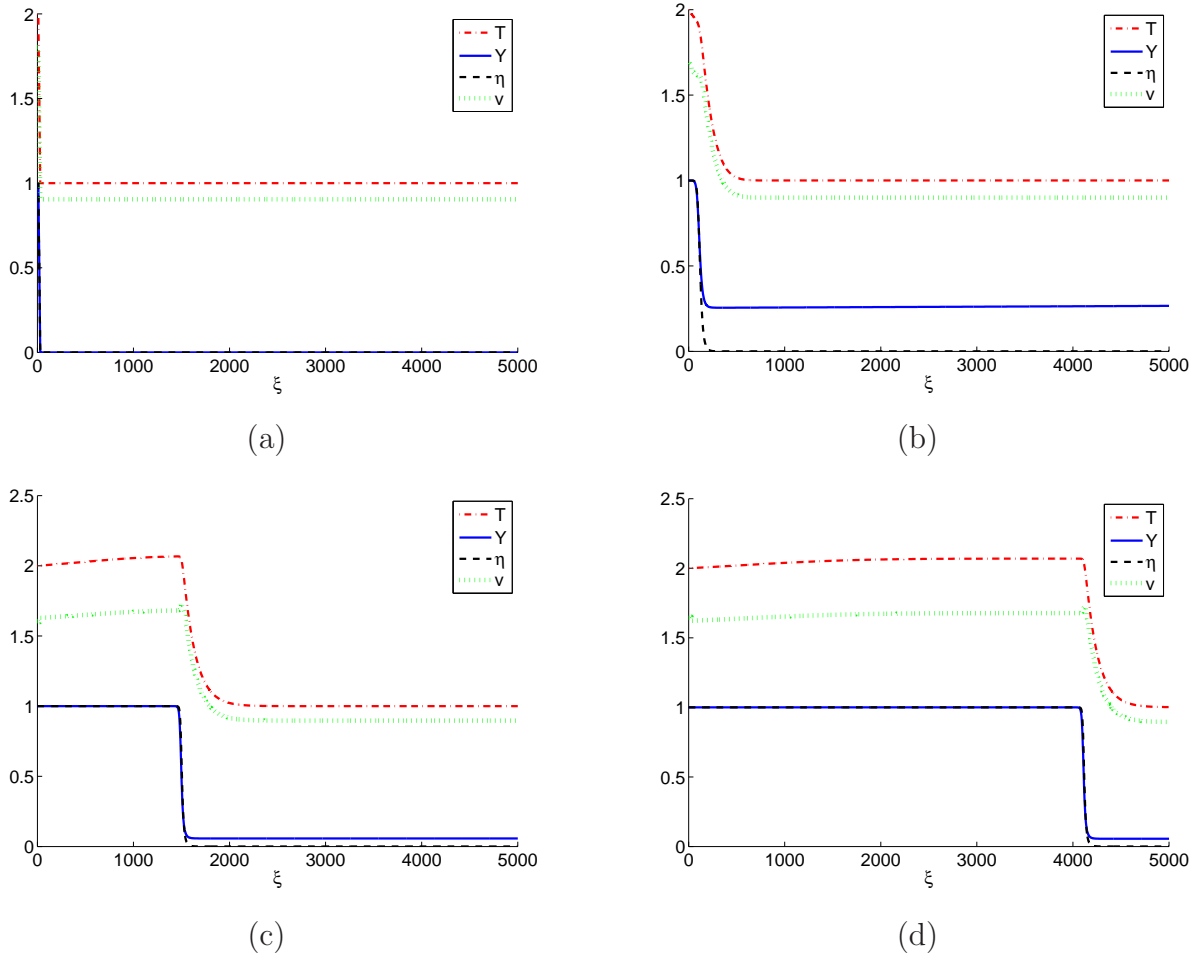
Figure 6.4: Numerical simulation using the hybrid method for system (2.23)-(2.26) with parameter values from Table 2.2 showing the formation of thermal and combustion waves. Figures (a) - initial data, (b) - after 30.000 time steps, (c) - after 200.000 time steps and (d) - after 510.000 time steps. Initial value for the variable θ at the injection end was taken as 2, the thermal wave is almost indistinguishable because of the diffusion effect. Notice that the combustion wave has a thin reaction layer where all the oxygen and fuel are consumed and thick thermal layer where only thermal conduction occurs. Compare with Figure 6.5.
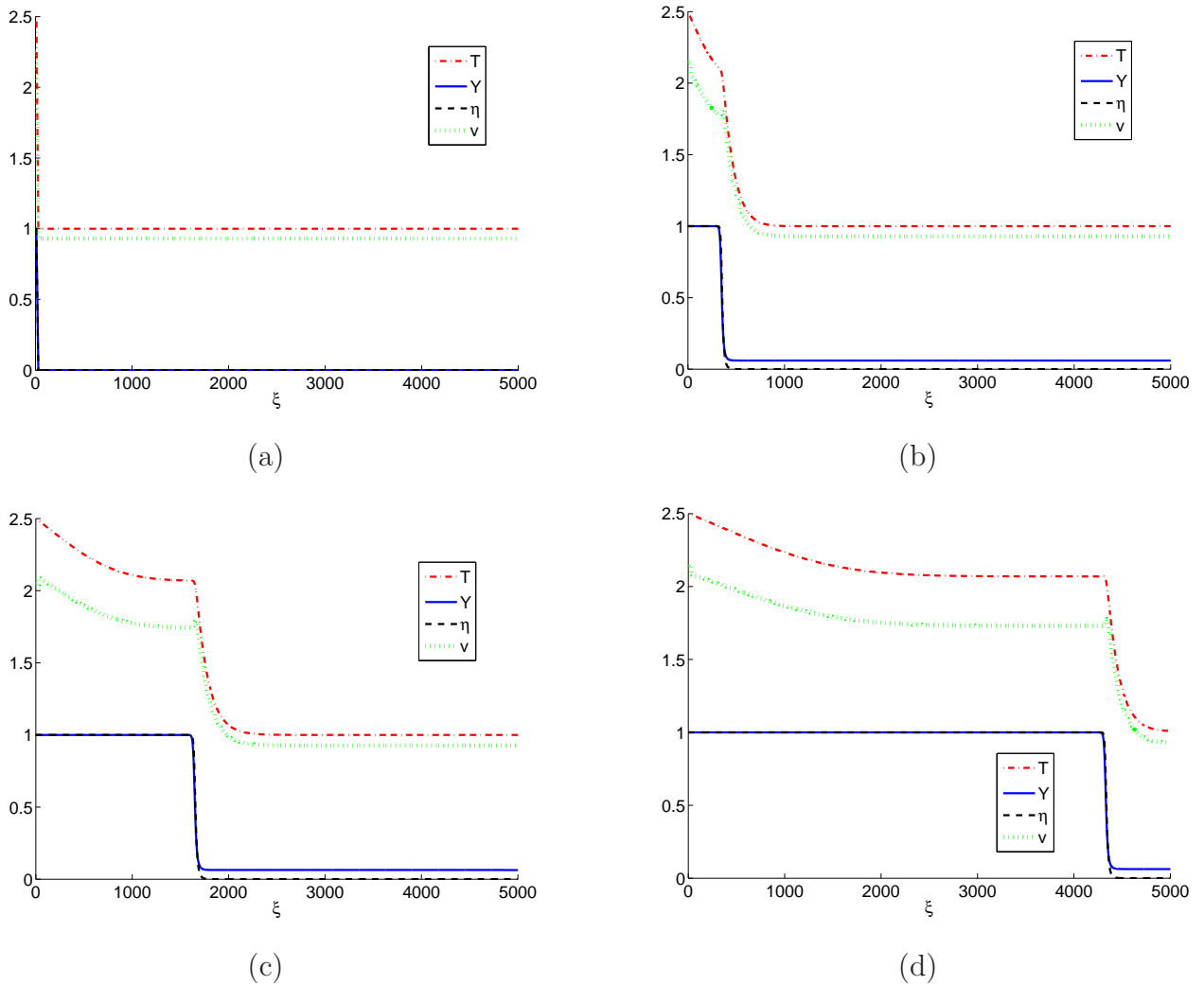
Figure 6.5: Numerical simulation using the hybrid method for system (2.23)-(2.26) with parameter values from Table 2.2 showing the formation of thermal and combustion waves. Figures (a) - initial data, (b) - after 50.000 time steps, (c) - after 200.000 time steps and (d) - after 510.000 time steps. Initial value for the variable θ at the injection end was taken as 2.5, the thermal wave is smooth due the diffusion effect. Notice that the combustion wave has a thin reaction layer where all the oxygen and fuel are consumed and thick thermal layer where only thermal conduction occurs. Compare with Figure 6.4.

Chapter 7

Stability analysis of combustion waves

In this chapter we introduce a simplified model for gas-solid combustion, which can be obtained from (2.16)-(2.20). There are reasons to do so. (1) We do not know how to perform the stability analysis of system (2.16)-(2.20). (2) Other simplifications described in Remark 7.2 have been subject to mathematical analysis, yet they are not physical as they consider infinite supply of oxygen and absolute zero temperature inside the reservoir, our simpler model is more physical. (3) As shown in Chapter 6, the numerical simulations for system (2.16)-(2.20) are not easy. Most importantly, the simplified model is more likely to be amenable to analysis.

The simplifications we will perform consist in considering the Lewis number so high that $1/L_e$ can be replaced by 0. Instead of the ideal gas law (2.20) we assume that ρ is constant. It follows that the gas speed $v > 0$ is also constant. We introduce by $c = av$. Thus the system (2.16)-(2.20) can be rewritten as follows. The dependent variables are temperature θ, oxygen fraction Y and fuel $\chi = 1 - \eta$, where η is the dimensionless fuel depth defined in Section 2.1:

$$\frac{\partial \theta}{\partial t} + c\frac{\partial \theta}{\partial x} = \frac{\partial^2 \theta}{\partial x^2} + q\Phi, \tag{7.1}$$

$$\frac{\partial Y}{\partial t} + v\frac{\partial Y}{\partial x} = -\mu\Phi, \tag{7.2}$$

$$\frac{\partial \chi}{\partial t} = -\Phi. \tag{7.3}$$

The combustion rate is described by Arrhenius' law:

$$\Phi = KY\chi e^{-\gamma/\theta}. \tag{7.4}$$

In Chapters 4 and 5 we find the combustion wave profile in the form of traveling wave for certain ISC models. In Chapter 6 we present numerical evidence that these waves exist

supporting our analysis. However, stability analysis of the combustion waves is such a delicate issue that a mathematical study is necessary. Unfortunately, the system (2.16)-(2.20) is difficult to work with, that is why in this chapter we present our efforts towards proving the stability of the combustion wave using the simplified model.

In Section 7.1 we apply the singular perturbation method to obtain the combustion wave profile for the simple model. In Section 7.2 we provide heuristic calculation for the continuous spectrum of the perturbation around the approximate solution obtained in Section 7.1. Finally, in Section 7.3 we summarize all we did in this chapter.

Remark 7.1 (Non-combustion waves) *It is easy to perform the analysis of the hyperbolic behavior of the system (7.1)-(7.3) as we did in Section 5.4. The characteristic speeds and corresponding characteristic modes of the resulting system are:*

$$
\begin{aligned}
\lambda_\theta &= c; \quad (1, 0, 0)^T; \\
\lambda_Y &= v; \quad (0, 1, 0)^T; \\
\lambda_\chi &= 0; \quad (0, 0, 1)^T.
\end{aligned}
\tag{7.5}
$$

We can see that the Riemann problem possesses three non-combustion contact waves. The slowest one is an immobile fuel wave $\lambda_\chi = 0$, the intermediate one is a thermal wave with speed $\lambda_\theta = c$ and the fastest one is the oxygen composition wave with speed $\lambda_Y = v$.

Remark 7.2 (Simplest model) *There is another possible way to simplify the model (2.16)-(2.20). We can make the previously mentioned simplifications except the Lewis number is not considered large. Another simplification is to assume infinite availability of fuel (equivalently one can consider infinite availability of oxygen). In this case the variables are θ - temperature and Y - concentration of oxygen. There are two constants L_e - Lewis number, β - reaction rate:*

$$
\frac{\partial \theta}{\partial t} = \frac{\partial^2 \theta}{\partial x^2} + Y e^{-1/\theta},
\tag{7.6}
$$

$$
\frac{\partial Y}{\partial t} = \frac{1}{L_e} \frac{\partial^2 Y}{\partial x^2} - \beta Y e^{-1/\theta}.
\tag{7.7}
$$

This model has the following difficulty. The associated ODE system for traveling wave possesses only two equilibria, one for $Y = 0$ and another for $\theta = 0$. From the physical point of view considering $\theta = 0$, or equivalently 0^oK, does not make sense. However this model is amenable to detailed mathematical analysis, see [6, 25].

7.1 Co-flow combustion traveling wave

Of course the singular perturbation analysis as performed in Chapter 4 for the traveling wave in the physical model is applicable to the simplified model (7.1)-(7.4) discussed here. Next we obtain the zero-order approximation of the traveling wave solution of the system (7.1)-(7.3) and compare it to the numerical solution.

7.1.1 Rankine-Hugoniot condition

Analogously to Chapter 4 we solve the Riemann problem with the following boundary conditions for the combustion wave:

$$\text{Left:} \quad \theta_-, \quad Y_- = 1, \quad \chi_- = 0; \tag{7.8}$$

$$\text{Right:} \quad \theta_+, \quad Y_+ = 0, \quad \chi_+ = 1. \tag{7.9}$$

Let us assume that the variables θ, Y and χ from (7.1)-(7.3) depend only on $\xi = x - Vt$, i.e., with some abuse of notation we write $\theta = \theta(\xi) = \theta(x - Vt)$, etcetera. The traveling wave associated to (7.1) reads:

$$\begin{cases} -V\dot\theta + c\dot\theta = \ddot\theta + q\Phi \\ -V\dot Y + v\dot Y = -\mu\Phi \\ -V\dot\chi = -\Phi. \end{cases} \tag{7.10}$$

Here the dot represents derivatives with respect to ξ. After one time integration we have:

$$\dot\theta + V\theta - c\theta + qV\chi + K_1 = 0; \tag{7.11}$$

$$-VY + vY + \mu V\chi + K_2 = 0; \tag{7.12}$$

$$\dot\chi = \frac{1}{V}\Phi. \tag{7.13}$$

Substituting the left boundary conditions (7.8) into (7.11)-(7.12) one obtains

$$\begin{aligned} (V - c)\theta_- + K_1 &= 0; \\ (v - V) + K_2 &= 0. \end{aligned} \tag{7.14}$$

Substituting the right boundary conditions (7.9) into (7.11)-(7.12) we get

$$\begin{aligned} (V - c)\theta_+ + qV + K_1 &= 0; \\ \mu V + K_2 &= 0. \end{aligned} \tag{7.15}$$

From (7.14)-(7.15):

$$K_1 = (c - V)\theta_-; \quad K_2 = V - v; \quad V = \frac{v}{1 + \mu}; \quad \theta_- = \theta_+ + \frac{qv}{v - c(1 + \mu)}, \tag{7.16}$$

where the last two equations correspond to the Rankine-Hugoniot relations. Notice that from the third equation of (7.16) follows that $V > 0$.

7.1.2 Approximate profile for the combustion wave

Substituting (7.16) into (7.11)-(7.13) one obtains the following system of two differential equations and one algebraic equation describing the traveling wave solution:

$$\begin{cases} \dot{\theta} = (c - V)(\theta - \theta_-) - qV\chi; \\ \dot{\chi} = \frac{1}{V}\Phi; \\ Y = 1 - \chi. \end{cases} \tag{7.17}$$

As we already know, the zero-order approximation of the system (7.17) is $(\theta_0(\chi_0), Y_0(\chi_0), \chi_0)$, such that:

$$\begin{cases} (c - V)(\theta_0 - \theta_-) - qV\chi_0 = 0; \\ Y_0 = 1 - \chi_0; \\ \dot{\chi}_0 = \frac{1}{V}\Phi(\theta_0, Y_0, \chi_0), \end{cases} \tag{7.18}$$

where $\chi_0 = \chi_0(\xi)$ and $\tilde{\chi} = \chi_0(0)$. This system provides equations for θ_0 and Y_0 in terms of χ_0 and an implicit equation for χ_0 in terms of ξ:

$$\begin{cases} \theta_0(\xi) = \theta_- + \frac{qV\chi_0(\xi)}{c - V}; \\ Y_0(\xi) = 1 - \chi_0(\xi); \\ \frac{K\xi}{V} = \int_{\tilde{\chi}}^{\chi_0} \exp\left(\frac{\gamma(c - V)}{(c - V)\theta_- + qV\chi}\right) \frac{d\chi}{\chi(1 - \chi)}. \end{cases} \tag{7.19}$$

Defining

$$A = \frac{\theta_-}{\gamma}, \quad B = \frac{qV}{\gamma(c - V)}, \quad \tilde{x} = \frac{1}{A + B\tilde{\chi}}, \quad x_0 = \frac{1}{A + B\chi_0} \tag{7.20}$$

the last equality can be written as:

$$\frac{K\xi}{V} = e^{\frac{1}{A}}\left(E_1\left(\frac{1}{A} - \tilde{x}\right) - E_1\left(\frac{1}{A} - x_0\right)\right) - e^{\frac{1}{A+B}}\left(E_1\left(\frac{1}{A+B} - \tilde{x}\right) - E_1\left(\frac{1}{A+B} - x_0\right)\right). \tag{7.21}$$

The equations (7.20) and (7.21) define $\chi_0 = \chi_0(\xi)$ implicitly.

7.1.3 Numerical simulations

In this section we apply the Crank-Nicolson scheme with adaptative time step as described in Section 6.1.1 to simulate the simplified combustion model given by the system (7.1)-(7.3) with combustion rate (7.4). For the details about implementation see [28]. In this simulation we use up to 10.000 grid points and to control numerical oscillations we add a small fixed diffusion term in (7.2). We use the parameter values $c = 0.2$, $q = 0.9$, $v = 1.2$, $K = 10^{-4}$, $\mu = 2$ and $\gamma = 4$.

The initial data for the simulation is shown on left side of Figure 7.1. We show the profile of the numerical solution of the system (7.1)-(7.3) at time $t = 2 \cdot 10^7$ on the right side in Figure 7.1. The formation of the thermal wave (near $\xi = 5 \cdot 10^6$) and the combustion wave (near $\xi = 8 \cdot 10^6$) are clearly visible. These waves were predicted by hyperbolic analysis in Remark 7.1. Immediately after the thermal wave we see a small elevation in the variable θ: it is a transient (not numerical) effect which disappears with time.
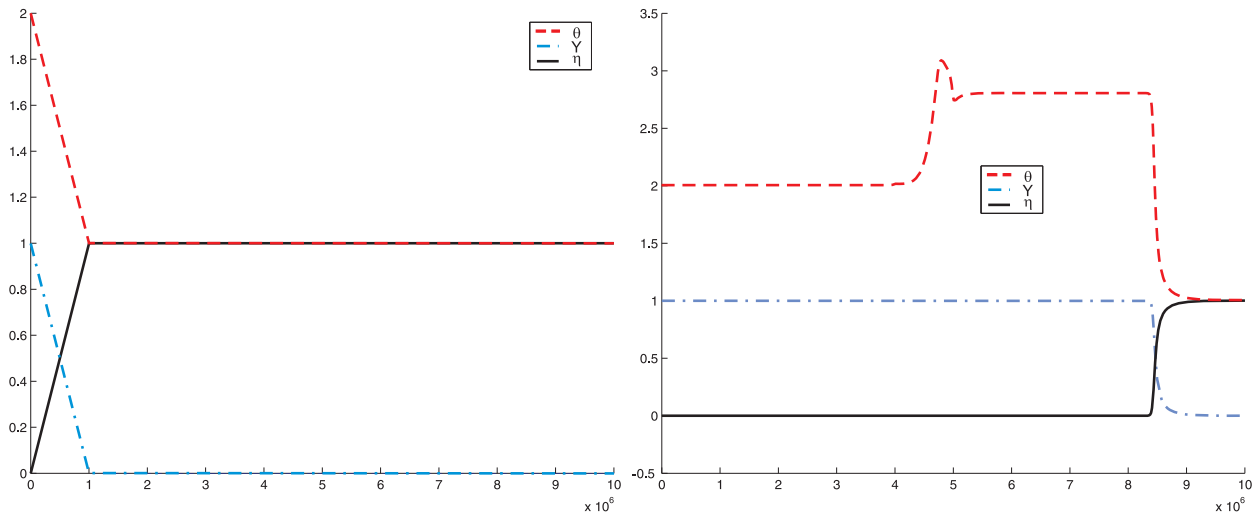
Figure 7.1: Numerical simulation using the Crank-Nicolson scheme with adaptative time step for the system (7.1)-(7.3) with the parameter values $c = 0.2$, $q = 0.9$, $v = 1.2$, $K = 10^{-4}$, $\mu = 2$ and $\gamma = 4$. The initial data is plotted on the left. Simulation results after $2 \cdot 10^7$ time units showing the formation of thermal and combustion waves are plotted on the right.

On the left side in Figure 7.2 we show the quasi-stationary approximation of the combustion wave profile obtained by numerical integration of (7.19) with $\tilde{\chi} = 0.5$. On the right side in Figure 7.2 we plot the combustion wave taken from Figure 7.1 on the same scale as the quasi-
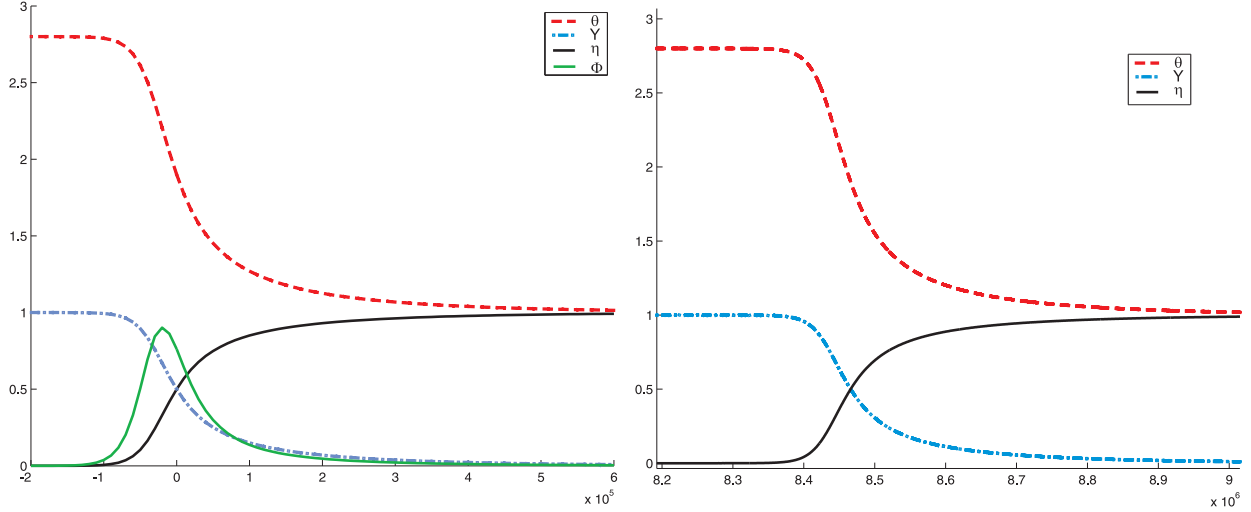
Figure 7.2: Singular perturbation approximation (7.19) on the left and the combustion wave profile obtained by Crank-Nicolson simulation from Figure 7.1 on the right. Both plots are on the same scale. We use parameter values $c = 0.2$, $q = 0.9$, $v = 1.2$, $K = 10^{-4}$, $\mu = 2$ and $\gamma = 4$.

stationary approximation. Both plots are visually indistinguishable.

7.2 Perturbations of the approximate traveling wave

Let us consider the system (7.1)-(7.3) in traveling wave coordinates:

$$\begin{cases} \partial_t\theta - V\partial_\xi\theta + c\partial_\xi\theta = \partial_{\xi\xi}\theta + q\Phi \\ \partial_t Y - V\partial_\xi Y + v\partial_\xi Y = -\mu\Phi \\ \partial_t\chi - V\partial_\xi\chi = -\Phi. \end{cases} \tag{7.22}$$

We can rewrite this system as:

$$\partial_t U + L_\xi(U) = \Psi(U), \tag{7.23}$$

where $U = (\theta, Y, \chi)^T$, L_ξ is a linear second order differential operator in ξ and Ψ is a general source term. Now we recall that the singular perturbation for the solution U of the system (7.23) yields $U = U_0 + \epsilon U_* + O(\epsilon^2)$, where U_0 and U_* do not depend on t. Thus (7.23) can be rewritten as:

$$\epsilon\partial_t U_* + L_\xi(U_0) + \epsilon L_\xi(U_*) = \Psi(U_0) + \epsilon\Psi_U(U_0)U_* + O(\epsilon^2). \tag{7.24}$$

70

Now we rename the first order approximation of the solution $U_1 = \epsilon U_*$ obtaining:

$$\partial_t U_1 + L_\xi(U_0) + L_\xi(U_1) = \Psi(U_0) + \Psi_U(U_0)U_1 + O(|U_1|^2). \tag{7.25}$$

We can rewrite it as:

$$(\partial_t + L_\xi - \Psi_U(U_0))U_1 = \Psi(U_0) - L_\xi(U_0) + O(|U_1|^2). \tag{7.26}$$

Notice that since the zero-order approximation $U_0(\xi)$ satisfies the boundary conditions (7.8) and (7.9), then $U_1(\xi)$ is a correction term; this correction term satisfies:

$$\lim_{\xi \to \pm\infty} U_1(\xi) = 0. \tag{7.27}$$

In what follows we replace the RHS of (7.26) by zero (this is equivalent to assuming that the zero-order approximation satisfies the system (7.22)).

Remark 7.3 *Notice that, as (7.24) shows, the RHS of (7.26) is not zero. In fact the zero-order solution does not satisfy the system (7.22) exactly. However the singular perturbation in Chapter 4 was derived by expanding the system (7.1) as power series in ϵ and then equating all terms with the same order in ϵ. If this analysis is valid, the right hand side of (7.26) has order ϵ^2, so we neglect it relative to the left hand side, which has order ϵ.*

Neglecting the $O(\epsilon^2)$ terms and using $U = U_0 + U_1$, (7.22) in (7.26), where the right hand side of equation (7.26) is replaced by zero, one obtains:

$$\begin{cases} \partial_t \theta_1 - V\partial_\xi \theta_1 + c\partial_\xi \theta_1 = \partial_{\xi\xi}\theta_1 + q\Phi_\theta \theta_1 + q\Phi_Y Y_1 + q\Phi_\chi \chi_1 \\ \partial_t Y_1 - V\partial_\xi Y_1 + v\partial_\xi Y_1 = -\mu\Phi_\theta \theta_1 - \mu\Phi_Y Y_1 - \mu\Phi_\chi \chi_1 \\ \partial_t \chi_1 - V\partial_\xi \chi_1 = -\Phi_\theta \theta_1 - \Phi_Y Y_1 - \Phi_\chi \chi_1. \end{cases} \tag{7.28}$$

The functions Φ_θ, Φ_Y and Φ_χ depend on χ_0:

$$\Phi_\theta = \frac{\gamma Y_0 \chi_0}{\theta_0(\chi_0)^2}\Upsilon(\chi_0); \quad \Phi_Y = \chi_0\Upsilon(\chi_0); \quad \Phi_\chi = Y_0(\chi_0)\Upsilon(\chi_0); \quad \Upsilon(\chi_0) = K\exp\left(\frac{-\gamma}{\theta_0(\chi_0)}\right). \tag{7.29}$$

where Φ_θ, Φ_Y and Φ_χ are functions of ξ using $\chi_0 = \chi_0(\xi)$ that is given implicitly by equations (7.20)-(7.21). The functions $\theta_0(\chi_0)$ and $Y_0(\chi_0)$ are given in (7.19).

7.2.1 Constructing the evolution operator

Now we assume that our variables (θ_1, Y_1, χ_1) depend on t and ξ in the following way:

$$(\theta_1(t,\xi), Y_1(t,\xi), \chi_1(t,\xi)) = e^{\lambda t}(\hat{\theta}_1(\xi), \hat{Y}_1(\xi), \hat{\chi}_1(\xi)), \tag{7.30}$$

where we are looking for real λ. In the following we will omit the hats, keep the subscript 1, and substitute (7.30) into system (7.28), obtaining the eigenvalue ODE problem:

$$\begin{cases} \lambda\theta_1 + (c-V)d_\xi\theta_1 = d_{\xi\xi}\theta_1 + q\Phi_\theta\theta_1 + q\Phi_Y Y_1 + q\Phi_\chi\chi_1 \\[2mm] \lambda Y_1 + (v-V)d_\xi Y_1 = -\mu\Phi_\theta\theta_1 - \mu\Phi_Y Y_1 - \mu\Phi_\chi\chi_1 \\[2mm] \lambda\chi_1 - V d_\xi\chi_1 = -\Phi_\theta\theta_1 - \Phi_Y Y_1 - \Phi_\chi\chi_1, \end{cases} \tag{7.31}$$

with the boundary conditions defined by (7.27). The second order system above can be reduced to a first order system by introducing the variable $\theta_1' = d_\xi\theta_1$:

$$\begin{cases} d_\xi\theta_1' = \lambda\theta_1 + (c-V)\theta_1' - q\Phi_\theta\theta_1 - q\Phi_Y Y_1 - q\Phi_\chi\chi_1 \\[2mm] d_\xi\theta_1 = \theta_1' \\[2mm] d_\xi Y_1 = \dfrac{\lambda V}{V-v} + \dfrac{\mu}{V-v}(q\Phi_\theta\theta_1 + q\Phi_Y Y_1 + q\Phi_\chi\chi_1) \\[2mm] d_\xi\chi_1 = \dfrac{\lambda}{V}\chi_1 + \dfrac{1}{V}(q\Phi_\theta\theta_1 + q\Phi_Y Y_1 + q\Phi_\chi\chi_1). \end{cases} \tag{7.32}$$

In order to simplify notation we drop the subindex 0, so we write Y, θ, χ instead of $Y_0(\xi)$, $\theta_0(\xi)$, $\chi_0(\xi)$. Thus the system (7.32) can be rewritten as:

$$d_\xi \begin{bmatrix} \theta_1' \\ \theta_1 \\ Y_1 \\ \chi_1 \end{bmatrix} = \begin{bmatrix} (c-V) & \lambda - \frac{q\gamma\Phi}{\theta^2} & -q\chi\Upsilon & -qY\Upsilon \\[2mm] 1 & 0 & 0 & 0 \\[2mm] 0 & \frac{\mu\gamma\Phi}{\theta^2(V-v)} & \frac{\mu\chi\Upsilon + \lambda}{V-v} & \frac{\mu Y\Upsilon}{V-v} \\[2mm] 0 & \frac{\gamma\Phi}{\theta^2 V} & \frac{\chi\Upsilon}{V} & \frac{Y\Upsilon + \lambda}{V} \end{bmatrix} \begin{bmatrix} \theta_1' \\ \theta_1 \\ Y_1 \\ \chi_1 \end{bmatrix}. \tag{7.33}$$

From the general ODE theory we know that given any initial condition the system (7.33) possesses a unique solution for all ξ. In order to perform the analysis of the boundary value problem we calculate the solution of the ODE in three subregions. First we analyze the limit cases: $\xi > M$ and $\xi < -M$, for some large $M > 0$. Then we study the behavior of U_1 for $-M < \xi < M$.

7.2.2 Left limit case

First let us consider the case $\xi < -M$. If M is large enough, in the interval $(-\infty, -M)$ the operator (7.33) can be approximated using the left boundary condition (7.8) $(Y \to 1, \chi \to 0)$ obtaining:

$$d_\xi \begin{bmatrix} \theta_1' \\ \theta_1 \\ Y_1 \\ \chi_1 \end{bmatrix} = \begin{bmatrix} c - V & \lambda & 0 & -q\Upsilon_- \\ 1 & 0 & 0 & 0 \\ 0 & 0 & \dfrac{\lambda}{V-v} & \dfrac{\mu\Upsilon_-}{V-v} \\ 0 & 0 & 0 & \dfrac{\Upsilon_- + \lambda}{V} \end{bmatrix} \begin{bmatrix} \theta_1' \\ \theta_1 \\ Y_1 \\ \chi_1 \end{bmatrix}, \tag{7.34}$$

where $\Upsilon_- = K\exp(-\gamma\theta_-^{-1})$. We rename the matrix in (7.34) as A_- and diagonalize it using $D_- = \Lambda_-^{-1} A_- \Lambda_-$, where:

$$D_- = \begin{bmatrix} \dfrac{\lambda}{V-v} & 0 & 0 & 0 \\ 0 & \dfrac{\Upsilon_- + \lambda}{V} & 0 & 0 \\ 0 & 0 & \dfrac{1}{2}(c - V - \Delta) & 0 \\ 0 & 0 & 0 & \dfrac{1}{2}(c - V + \Delta) \end{bmatrix}, \quad \Delta = \sqrt{(V-c)^2 + 4\lambda},$$

$$\Lambda_- = \begin{bmatrix} 0 & \dfrac{\Upsilon_- + \lambda}{V} & \dfrac{c - V - \Delta}{2} & \dfrac{c - V + \Delta}{2} \\ 0 & 1 & 1 & 1 \\ 1 & \Delta_1 & 0 & 0 \\ 0 & \Delta_2 & 0 & 0 \end{bmatrix}, \quad \text{with}$$

$$\Delta_1 = -\frac{\mu(cV(\Upsilon_- + \lambda) - (\Upsilon_+\lambda)^2 - V^2\Upsilon_-)}{qV(\Upsilon_- V - \Upsilon_- v - v\lambda)}, \quad \Delta_2 = -\frac{\mu(cV(\Upsilon_- + \lambda) - (\Upsilon_+\lambda)^2 - V^2\Upsilon_-)}{q\Upsilon_- V^2}.$$

Thus the general solution of (7.34) is:

$$[\theta_1'(\xi),\, \theta_1(\xi),\, Y_1(\xi),\, \chi_1(\xi)]^T = \Lambda_-^{-1}\exp(D_-\xi)\,\Lambda_-\,B_-, \tag{7.35}$$

where $B^- = [B_1^-, \ldots, B_4^-]^T$ is a vector of real constants to be determined later. As the matrix Λ_- is constant in ξ and has full rank, we define the vector of constants $C_- = [C_1^-, \ldots, C_4^-]^T = \Lambda_- B_-$ and rewrite (7.35) as:

$$[\theta_1'(\xi),\, \theta_1(\xi),\, Y_1(\xi),\, \chi_1(\xi)]^T = \Lambda_-^{-1}\exp(D_-\xi)\,C_-, \tag{7.36}$$

where C_- needs to be determined later.

The boundary condition (7.27) implies:

$$\lim_{\xi \to \pm\infty} \theta_1'(\xi) = 0, \quad \lim_{\xi \to \pm\infty} \theta_1(\xi) = 0, \quad \lim_{\xi \to \pm\infty} Y_1(\xi) = 0, \quad \lim_{\xi \to \pm\infty} \chi_1(\xi) = 0. \tag{7.37}$$

Therefore we look for solutions θ_1', θ_1, Y_1 and χ_1 that decay to 0 as $\xi \to -\infty$. Notice that the matrix Λ_-^{-1} in (7.36) is constant in ξ. Then θ_1', θ_1, Y_1 and χ_1 are linear combinations of the elements of the vector $\exp(D_-\xi)\, C_-$, so we just need to analyze the behavior of this vector as ξ tends to $-\infty$:

$$\exp(D_-\xi)\, C_- =$$
$$\left[C_1^- \exp\left(\frac{\lambda}{V-v}\xi\right), \ \ C_2^- \exp\left(\frac{\Upsilon_- + \lambda}{V}\xi\right), \ \ C_3^- \exp\left(\frac{c-V-\Delta}{2}\xi\right), \ \ C_4^- \exp\left(\frac{c-V+\Delta}{2}\xi\right) \right]^T.$$
$$\tag{7.38}$$

The analysis is quite simple: if the sign of the coefficient of ξ (which is an eigenvalue) inside the exponent is positive, the solution decays as $\xi \to -\infty$ and the corresponding coefficient C_j represents one degree of freedom for the solution (i.e., C_j does not need to vanish). If the sign is negative, the corresponding coefficient C_j must be zero. In the case when the coefficient of ξ is zero we cannot conclude anything.

From the third equation of (7.16) we get $V - v < 0$. It follows that if $\lambda < 0$ then C_1^- is a free parameter, and if $\lambda > 0$ then $C_1^- = 0$. If $\lambda > -\Upsilon_-$ then C_2^- is a free parameter, and if $\lambda < -\Upsilon_-$ then $C_2^- = 0$. For two last eigenvalues the analysis is more delicate. The eigenvalues are real only if $\lambda > -(V-c)^2/4$, let us consider this situation first. Based on the results for the physical model studied in Chapter 4, we may assume $c < V$, thus for the eigenvalue corresponding to C_3^- to be positive it is necessary that $c - V - \Delta > 0$, as $c < V$ and $\Delta > 0$ we conclude that $C_3^- = 0$ for all $\lambda > -(V-c)^2/4$. If $\lambda \leq -(V-c)^2/4$ we need the real part of the eigenvalue to be positive, however $\mathcal{R}e(\Delta) = 0$ in this case and as $c < V$ we get $C_3^- = 0$. An analogous analysis yields $C_4^- = 0$ for $\lambda < 0$, and C_4^- is a free parameter for $\lambda > 0$.

We can associate the constants C_j^- to the degrees of freedom that the system (7.34) possesses when the boundary conditions (7.37) at $-\infty$ are imposed. Schematically we can represent the number of degrees of freedom or the nonzero constants C_j^- for different regions of λ in Figure 7.3.
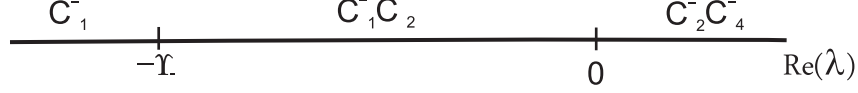
Figure 7.3: Schematic representation of the degrees of freedom in different regions of λ for $\xi \to -\infty$.

7.2.3 Right limit case

Now we consider the case $\xi > M$. If M is large enough the operator (7.33) can be approximated in the interval (M, ∞) using the right boundary conditions (7.9), obtaining:

$$
d_\xi \begin{bmatrix} \theta_1' \\ \theta_1 \\ Y_1 \\ \chi_1 \end{bmatrix} = \begin{bmatrix} c - V & \lambda & -q\Upsilon_+ & 0 \\ 1 & 0 & 0 & 0 \\ 0 & 0 & \dfrac{\mu\,\Upsilon_+ + \lambda}{V - v} & 0 \\ 0 & 0 & \dfrac{\Upsilon_+}{V} & \dfrac{\lambda}{V} \end{bmatrix} \begin{bmatrix} \theta_1' \\ \theta_1 \\ Y_1 \\ \chi_1 \end{bmatrix},
\tag{7.39}
$$

where $\Upsilon_+ = K \exp(-\gamma\theta_+^{-1})$. We denote the matrix in (7.39) by A_+ and diagonalize it using $D_+ = \Lambda_+^{-1} A_+ \Lambda_+$, where:

$$
D_+ = \begin{bmatrix} \dfrac{\lambda}{V} & 0 & 0 & 0 \\ 0 & \dfrac{\mu\Upsilon_+ + \lambda}{V - v} & 0 & 0 \\ 0 & 0 & \dfrac{1}{2}(c - V - \Delta) & 0 \\ 0 & 0 & 0 & \dfrac{1}{2}(c - V + \Delta) \end{bmatrix}, \quad \Delta = \sqrt{(V - c)^2 + 4\lambda},
$$

$$
\Lambda_+ = \begin{bmatrix} 0 & \dfrac{\mu\Upsilon_+ + \lambda}{V - v} & \dfrac{c - V - \Delta}{2} & \dfrac{c - V + \Delta}{2} \\ 0 & 1 & 1 & 1 \\ 0 & \Delta_3 & 0 & 0 \\ 1 & \Delta_4 & 0 & 0 \end{bmatrix}, \quad \text{with}
$$

$$
\Delta_3 = \frac{(V - v)(\lambda(c - v) + \mu\Upsilon_+(c - V)) - (\mu\Upsilon_+ + \lambda)^2}{q\Upsilon_+(v - V)^2},
$$

$$
\Delta_4 = \frac{(v - V)(\lambda(v - c) + \mu\Upsilon_+(V - c)) - (\mu\Upsilon_+ + \lambda)^2}{q(v - V)(V\mu\Upsilon_+ + \lambda v)}.
$$

Analogously to the left limit case the solution of (7.39) is given by:

$$
[\theta_1'(\xi), \theta_1(\xi), Y_1(\xi), \chi_1(\xi)]^T = \Lambda_+^{-1} \exp(D_+\xi)\, \Lambda_+ B_+,
\tag{7.40}
$$

75
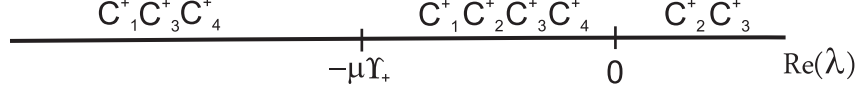
Figure 7.4: Schematic representation of the degrees of freedom in different regions of λ for $\xi \to \infty$.

where $B^+ = [B_1^+, \ldots, B_4^+]^T$ is a vector of real constants to be determined later. As the matrix Λ_+ is constant in ξ and has full rank, we define the vector of constants $C_+ = [C_1^+, \ldots, C_4^+]^T = \Lambda_+ B_+$ and rewrite (7.35) as:

$$[\theta_1'(\xi),\ \theta_1(\xi),\ Y_1(\xi),\ \chi_1(\xi)]^T = \Lambda_+^{-1} \exp(D_+\xi)\, C_+, \tag{7.41}$$

where C_+ needs to be determined later.

Because of the boundary conditions (7.37) we want θ_1', θ_1, Y_1 and χ_1 to decay to 0 as $\xi \to \infty$. Then θ_1', θ_1, Y_1 and χ_1 are linear combinations of the terms of the vector $\exp(D_+\xi)C_+$ and we just need to analyze the behavior of this vector as ξ tends to $-\infty$:

$$\exp(D_+\xi)C_+ =$$
$$\left[C_1^+ \exp\left(\frac{\lambda\xi}{V}\right),\ C_2^+ \exp\left(\frac{\mu\Upsilon_+ + \lambda}{V - v}\xi\right),\ C_3^+ \exp\left(\frac{c - V - \Delta}{2}\xi\right),\ C_4^+ \exp\left(\frac{c - V + \Delta}{2}\xi\right) \right]^T.$$
$$\tag{7.42}$$

In this case we need the coefficients of ξ (eigenvalues) to be negative. If $\lambda < 0$ then C_1^+ is a free parameter, and if $\lambda > 0$ then $C_1^+ = 0$. Since $V - v < 0$ it follows that if $\lambda > -\mu\Upsilon_+$ then C_3^+ is a free parameter, and if $\lambda < -\mu\Upsilon_+$ then $C_3^+ = 0$. For two last eigenvalues the analysis is similar. When $\lambda > -(V - c)^2/4$ it follows that Δ is real and thus $c - V - \Delta < 0$ and C_3^+ is a free parameter. If When $\lambda \leq -(V - c)^2/4$ we need the real part of the eigenvalue corresponding to C_3^+ to be negative. As in this case $\mathcal{Re}(\Delta) = 0$ and $c < V$ this always happens and C_3^+ is a free parameter for all λ. An analogous analysis results that if $\lambda < 0$, then C_4^+ is a free parameter and if $\lambda > 0$ then $C_4^+ = 0$.

We associate the constants C_i^+ to the degrees of freedom that the system possesses and represent them schematically in Figure 7.4.

7.2.4 Solutions that match the limit cases

Now we can show evidence that the system (7.33) possesses a solution for all ξ. Since all functions involved are smooth we expect that there is some real number M, such that for
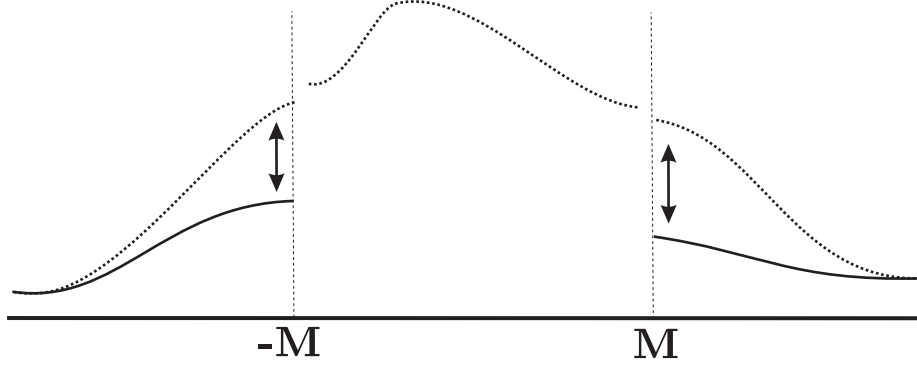
76

Figure 7.5: Schematic representation of matching three types of solutions in the intervals $(-\infty, -M]$, $[-M, M]$ and $[M, \infty]$.
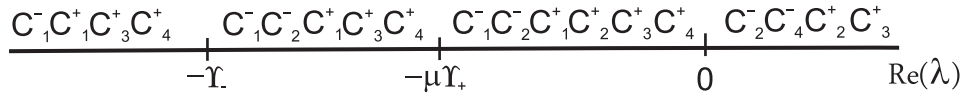
Figure 7.6: Schematic representation of the degrees of freedom in different regions of λ.

$|\xi| > M$ the solution of the system is close to the solutions of the limit cases described before. According to the general ODE theory we know that the system (7.33) possesses a fundamental matrix (the solutions of this ODE forms a basis at any ξ) in the interval $[-M, M]$, see [45]. So we need this solution to match the solutions obtained from the limit cases as shown on Figure 7.5. In order to do the match we perform the following heuristic analysis. We need to match the solutions for the limit cases in ξ in the 4D space of states $(\theta', \theta, Y, \chi)$. So we need to match 4 components of the vector U_1. In Figure 7.6 we combine Figures 7.3 and 7.4 to show schematically how many degrees of freedom the system (7.33) possesses.

The system (7.33) is autonomous, thus the solutions are obtained up to some constant and we need to fix the value at some point ξ for at least one variable θ', θ, Y or χ. So we need to use one degree of freedom to fix this constant. Thus we need five free parameters (or degrees of freedom) to match together the solutions at different ξ-intervals. As represented in Figure 7.6, this happens only inside the interval $[-\Upsilon_-, 0]$. Inside the interval $[-\mu\Upsilon_+, 0]$ we get one extra free parameter. We conjecture that it is associated with the geometric multiplicity of eigenvalues. Taking these facts into account we can expect that the spectrum of (7.33) is the interval $[-\Upsilon_-, 0]$ and that it has geometric multiplicity 2 in the interval $[-\mu\Upsilon_+, 0]$.

7.3 Conclusions

In this chapter we have introduced the gas-solid combustion model described by the system (7.1)-(7.3), which is a simplification of the physical model (2.16)-(2.20). However, this system still possesses the same wave sequence as the original one. We solve the Riemann problem for (7.1)-(7.3) with boundary conditions (7.8), (7.9) and use Singular Perturbation method in order to obtain an approximation of the combustion wave profile.

Next, we have performed some heuristic calculations and we state a conjecture about the operator governing the evolution of perturbations around the combustion wave profile. The conjecture is that this operator possesses the spectrum $[-\Upsilon_-, 0]$, i.e., it satisfies a necessary condition for stability of the combustion wave profile. For the solution obtained with the Singular Perturbation technique the spectrum has geometric multiplicity of two in the interval $[-\mu\Upsilon_+, 0]$, see Figure 7.6. Unfortunately, we cannot conclude anything about the point 0 of the spectrum. Of course, numerical simulations support the stability conjecture.

Chapter 8

Introduction to reaction kinetics

The main purpose of this work is to study certain models for the combustion wave occurring during the ISC process. However, the input of the combustion models requires many data, which can be found scattered in the literature. The reaction rate R_c of coke combustion with oxygen is usually given by:

$$R_c = k_c C_g^m \exp\left(\frac{-E}{RT}\right) \quad [1/s], \tag{8.1}$$

where m is the reaction order, C_g is the ratio of the oxygen partial pressure and atmospheric pressure, E is the activation energy, R is the ideal gas constant. The coefficient k_c is given by:

$$k_c = \eta A_g \tilde{k}_c \, [1/s], \tag{8.2}$$

where η is an efficiency factor, $A_g \, [m^2/kg - coke]$ - specific surface area, $\tilde{k}_c \, [kg/m^2 s]$ is the frequency factor of the reaction.

This chapter serves two purposes. First we want to give a rationale for meaning of coefficients in equations (8.1), (8.2) and secondly we want to obtain a uniform basis for a comprehensive data set. For more details see [15].

Remark 8.1 (gas transfer effects) *The reaction inside the particle produces other gases that are expelled out of the particle. Thus the concentration of oxygen in the bulk gas layer C_g and the concentration of oxygen on the particle surface C_s can be different due to external mass-transfer limitations. This effect slows down the reaction rate. In [22, 44] this correction is neglected, in our analysis we also neglect it.*

8.1 Specific surface area

In the literature it is often assumed that carbon based fuel has a porous structure. In order to react, the oxygen present in the air has to contact the fuel present inside this porous structure. A porous coke particle has a specific *external* surface area, which is of the order of the inverse particle diameter. However, the larger contact area is within the particle. It is also referred as the *internal* surface area. The internal surface area can be one to several hundreds square meters per gram. It is clear that in such a case we can also consider that the oxygen is dissolving inside the coke particle as the space available to the oxygen will be of the order of molecular size. We will ignore these complications and talk about internal and external surface.

In the literature there is a concept of **catalytical** (reacting) surface of the particle as the surface where the reaction occurs: it contains the internal and external surface areas. The catalytical surface area A_g of the particle is obtained by injecting nitrogen close to the boiling point in a sample of fuel and fitting it to a BET isotherm (using BET method) [13]. It can be found in the literature [22, 44] for different materials in units of square meters of surface area per kilogram of fuel.

During the reaction the surface area can change, see [35]. Here we are not considering this possibility by assuming that the catalytical surface area remains constant.

8.2 Order of reaction

The carbon-containing molecules on the particle surface are geometrically distributed in some way. In order to react, oxygen has to be absorbed onto the catalytical surface of the particle. To take the Langmuir absorption into account we have to approximate the reaction rate in a concentration range of interest as being proportional to the oxygen concentration to some fractional power and by introduce **the order of reaction**. Following [36], we define the order of reaction in the following way. If the rate of reaction can be expressed by an empirical differential equation that contains a factor of the form $k[A]^\alpha[B]^\beta \ldots$, where $[A]$, $[B]$, etc., are the reactant concentrations, α and β are constant exponents (independent of concentration and time) and k is a (rate) coefficient independent of $[A]$, $[B]$, etc., then the reaction is said to be of order α with respect to A, of order β with respect to B, ... , and of total order $m = \alpha + \beta + \ldots$. In general the exponents α, β, ... can be positive or negative, integer or not. It is also possible to consider the order α, etc., of the reaction to depend on time and to change

with the concentration ranges.

There are two common ways to use the reaction order. One considers all the elementary reactions that appear during the combustion. In this case the elementary reaction orders coincide with the integer stoichiometric coefficients, however, one needs to know all the elementary reactions that occur in the combustion and put them into the system of conservation laws describing the physical model. Even in ideal cases this is rather complex. As the composition of petroleum coke can vary, the elementary reactions can vary substantially. Moreover the resulting system of conservation laws is very difficult to work with. Finally, using this formulation it is not clear how the geometrical properties of the particle pores mentioned before influence the elementary reaction orders.

That is why in this text we consider the experimentally obtained reaction order. In the case of combustion we are interested in, the coke changes slowly. Thus we consider only the reaction order corresponding to the oxygen concentration (rate between the oxygen pressure on the surface and reference pressure, in our case atmospheric pressure) on the catalytical surface. It coincides with the total reaction order and we denote it by m. This quantity is dimensionless and its range is usually $0.3 \leq m \leq 1$ for coke combustion, [44].

8.3   Distribution of petroleum coke in the porous media

Let us consider the reservoir under the effects of the thermal wave when the water has already evaporated and the reservoir is filled with oil and gas. We indicate the surface tension forces between oil and rock, oil and gas, gas and rock by F_{OR}, F_{OG} and F_{GR}, the adherence force that attracts oil to rock surface by F_A and the contact angle by θ. Figure 8.1 indicates the tension forces with the corresponding subscripts acting on the three-phase contact line. The surface force balance equation (Young law) is written as $F_{RG} - F_{OR} = F_{OG} \cos(\theta)$, or equivalently:

$$\cos(\theta) = \frac{F_{RG} - F_{OR}}{F_{OG}} \equiv K_\theta. \tag{8.3}$$

We recall that the surface tension γ is defined as derivative of the Gibbs free energy G with respect to the surface area A:

$$\gamma = \left(\frac{\partial G}{\partial A}\right)_{P,T,n}, \tag{8.4}$$

where the subscript P, T, n means that the derivative is taken at constant pressure, temperature and molar concentration. For a displacement Δx perpendicular to a three phase contact line

of length l we obtain:

$$\gamma = \frac{dG}{ldx} = \frac{F}{l}, \tag{8.5}$$

where F is the resulting surface tension force. As the three phase contact line is the same for oil and gas we can rewrite (8.3) for surface tensions:

$$\cos(\theta) = \frac{\gamma_{RG} - \gamma_{OR}}{\gamma_{OG}} \equiv K_\theta. \tag{8.6}$$

One can interpret this law as resulting from the minimum energy principle. Using (8.3) we see that during the evaporation process some possibilities can occur. If $\gamma_{RG} > \gamma_{OR} + \gamma_{OG}$ the petroleum coke covers the sand grains. Assume that all the sand grains are spherical and have the same radius R. It is now possible to estimate the thickness of the coke layer δ around the grain for the situation of interest to us, see Figure 8.1. From the experimental data we get the average particle radius R, coke density inside the porous media $\rho_f^0\,[kg-coke/m^3-porous\ media]$ and coke density $\rho_{coke}\,[kg-coke/m^3-coke]$. Thus, the ratio between ρ_f^0 and ρ_{coke} is equal to the fraction of volume occupied by coke in each particle inside porous medium:

$$\frac{4\pi R^2 \delta}{4/3\pi R^3}(1-\phi) = \frac{\rho_f^0}{\rho_{coke}}. \tag{8.7}$$

We get the approximate thickness of the coke layer:

$$\delta = \frac{\rho_f^0 R}{3(1-\phi)\rho_{coke}}\,[m]. \tag{8.8}$$

Taking values $R = 6.7 \cdot 10^{-5}\,[m]$, $\rho_f^0 = 20\,[kg/m^3]$ from Table 8.3, $\phi = 0.3$ from Table 2.1 and $\rho_{coke} = 500\,[kg/m^3][1]$, we get $\delta \approx 1.28 \cdot 10^{-6}\,[m]$.

If $\gamma_{RC} < \gamma_{OR} + \gamma_{OG}$, the oil may form a globule encompassing various grains before cracking and this has profound influence on the effectiveness factor discussed below.

8.4   Effectiveness factor

It has often been stated that the molar mass of consumed carbon and the amount of released energy during the reaction in high temperature oxidation mode (combustion) depend on the consumed molar mass of oxygen but not on the nature of the carbon-containing material [44]. This is why it is important to know how the oxygen diffuses into the carbon-containing particles.

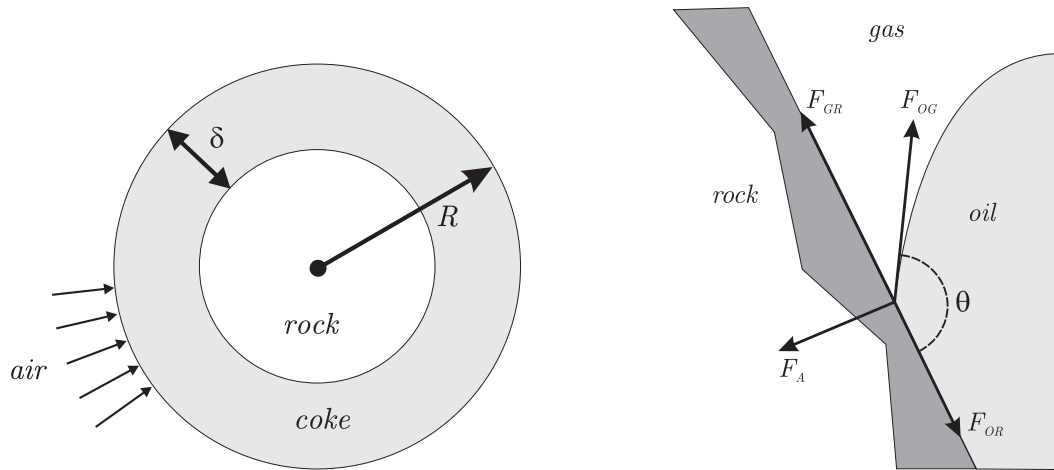[1]Value taken from the site http://www.simetric.co.uk/si_materials.htm

Figure 8.1: Left: schematic representation of the porous media particle. Right: surface tension forces in the porous media and the contact angle.

The ratio between the real reaction rate and the idealized one with complete gas access inside and outside the particle is called the effectiveness factor, see [8].

There are two main effects responsible for the effectiveness factor. The first of them tends to decrease the effectiveness factor; it is related to the entrance of oxygen into the particle. We explain this factor in more detail later. The second one tends to increase the effectiveness factor; The effectiveness factor is enhanced by temperature effects inside the particle as the coke oxidation reaction is exothermic. All of this depends on diffusion rates, characteristic pores size and particle size. The correct way of defining and estimating the effectiveness factor taking into account both effects is still under discussion, see [48]. Also in [48] some examples of materials with effectiveness factor greater than 1 can be found.

In this text we follow the references [8, 22, 44] and neglect the thermal part of the effectiveness factor. Some reasons for doing so are: the layer occupied by the fuel is thin (as described in Section 8.3 if $\gamma_{RC} > \gamma_{OR} + \gamma_{GC}$) and if the oil spreads over the grain, then the temperature inside this layer can be considered homogeneous; certain experiments with petroleum coke (see [49]) indicate that the thermal effect is negligible for gas diffusion inside small particles; there is no comprehensive theory on this effect.

Following [8], we introduce the effectiveness factor in a generally accepted way by using the Thiele modulus. This method is based on the hypothesis that the displacement of oxygen occurs only due to diffusion and that the oxygen leaves the system only because of the reaction. Then

it is assumed that the particles have some well defined shape (spherical, flat, long cylindrical, etc.) and the effectiveness factor is obtained form the balance equation of the reacting oxygen diffusing through the particle. In this case the factor is always smaller than 1.

8.4.1 Effectiveness factor for flat particles

Consider a "flat particle" as an infinite layer $0 \leq x \leq L$ on the yz plane in xyz space. We assume that the oxygen enters the flat particle from the side $x = 0$. We consider the first order chemical reaction with constant (average) reaction rate $k"$ [35], where the double prime indicates a reaction rate per unit surface area. We also assume that the diffusion coefficient D is constant. Thus, the balance equation for the oxygen concentration $c(x,t)$ inside the particle is:

$$\frac{\partial c}{\partial t} + v \frac{\partial c}{\partial x} = D \frac{\partial^2 c}{\partial^2 x} - k" A_g c \quad \left[\frac{kg_{air}}{m_p^3 s} \right], \tag{8.9}$$

where $A_g \, [m_p^2/kg]$ is the catalytical surface area of the particle, with m_p indicated unit length inside the pore. We define the boundary conditions for the oxygen concentration to c_0 at $x = 0$ and in such way that there is no mass flux at $x = L$. Next we assume that the displacement of oxygen inside the particle occurs only due to diffusion ($v \ll D$) and look for stationary solutions ($c(x,t) = c(x)$) of (8.9):

$$D \frac{d^2}{dx^2} c = k" A_g c, \quad c(0) = c_0; \quad \frac{dc}{dx}(L) = 0. \tag{8.10}$$

The solution of (8.10) is

$$c(x) = c_1 \sinh(\sqrt{\alpha} x) + c_2 \cosh(\sqrt{\alpha} x). \tag{8.11}$$

where $\alpha = k" A_g / D$. Using the boundary conditions we obtain the solution:

$$c(x) = c_0 \frac{\cosh(\sqrt{\alpha}(L - x))}{\cosh(\sqrt{\alpha} L)}. \tag{8.12}$$

In order to study the oxygen flux trough the particle boundary we introduce:

$$C(t) = \int_0^L c(x,t) dx \tag{8.13}$$

as the total amount of oxygen in the system per unit surface area. Using (8.9) we obtain the total accumulation of the oxygen inside the particle:

$$\frac{dC(t)}{dt} = \int_0^L \frac{\partial c(x,t)}{\partial t} dx = D \int_0^L \frac{\partial^2 c}{\partial x^2} dx - k" A_g \int_0^L c \, dx = D \left. \frac{\partial c}{\partial x} \right|_0^L - k" A_g \int_0^L c \, dx, \tag{8.14}$$

where the terms on the right hand side represent oxygen flux through the boundary and the consumption of oxygen due to the reaction inside the layer. If we consider stationary solution of (8.9), the accumulation term on the left hand side of (8.14) vanishes and the flux of the oxygen through the boundary is equal to the consumption rate of oxygen inside the pore:

$$W_R = D \left. \frac{\partial c(x)}{\partial x} \right|_0^L = -Dc_0\sqrt{\alpha} \left. \frac{\sinh(\sqrt{\alpha}(L-x))}{\cosh(\sqrt{\alpha}L)} \right|_0^L = Dc_0\sqrt{\alpha} \frac{\sinh(\sqrt{\alpha}L)}{\cosh(\sqrt{\alpha}L)}. \tag{8.15}$$

In order to obtain the "ideal" oxygen flux through the partice surface $x = 0$, we imagine that the concentration of oxygen is constant inside the particle, $c(x) = c_0$. For the stationary solution of (8.14) the flux of oxygen to the particle in this case:

$$W_0 = k" A_g \int_0^L c_0 x dx = Lk" A_g c_0, \tag{8.16}$$

We want to compare the flux W_0 with the oxygen flux W_R obtained from (8.14). Following [8], we define the effectiveness factor η as the ratio:

$$\eta = \frac{W_R}{W_0} = \frac{Dc_0\sqrt{\alpha}}{Lk" A_g c_0} \frac{\sinh(\sqrt{\alpha}L)}{\cosh(\sqrt{\alpha}L)} = \frac{\sinh \varphi}{\varphi \cosh \varphi} \quad [\cdot], \tag{8.17}$$

where dimensionless parameter $\varphi = L\sqrt{k" A_g/D}$ is the **Thiele modulus**. In order to obtain its value we consider L to be the coke layer thickness δ given in (8.8) and approximate the reaction rate $k"$ by $\tilde{k}_c \exp(-E/(RT))$. The values of the frequency factor $\tilde{k}_c$ and specific surface area A are given in Table 8.3. The temperature T and the diffusion coefficient are considered to be constant in the ranges $700 \leq T \leq 1300$ and $10^{-14} \leq D \leq 10^{-8} \, [m^2/s]$. The corresponding effectiveness factors are close to 1.0 as presented in Table 8.1.

Table 8.1: Effectiveness factor for the flat particles of petroleum coke for different temperatures and diffusion coefficients, based on data from Table 8.3 for [44]

$D \backslash T$	$700^0 C$	$900^0 C$	$1100^0 C$	$1300^0 C$
10^{-8}	1.0000	1.0000	1.0000	1.0000
10^{-10}	1.0000	1.0000	1.0000	1.0000
10^{-12}	1.0000	1.0000	1.0000	1.0000
10^{-14}	1.0000	1.0000	0.9999	0.9982

8.4.2 Effectiveness factor for spherical particles

We consider homogeneous spherical particle of fuel with radius R. Let us assume that the oxygen on the external surface has concentration $c(r) = c_0$ and some constant concentration as the center $c(0) = c_L$. Analogously to the flat particle case we assume that oxygen transport occurs only by diffusion and that the reaction is of first order, so that the oxygen balance equation is:

$$D \frac{1}{r^2} \frac{d}{dr} \left(r^2 \frac{dc(r)}{dr} \right) = -k'' A_g c(r). \tag{8.18}$$

This equation can be solved using the boundary conditions $c(0) = c_L$, $c(r) = c_0$ specified above using substitution $r \to f = rc(r)$:

$$c(r) = c_0 \frac{R}{r} \frac{\sinh(r\sqrt{k''A_g/D})}{\sinh(R\sqrt{k''A_g/D})}. \tag{8.19}$$

The oxygen flux trough the surface of the particles:

$$W_R = 4\pi R^2 D \left. \frac{dc}{dr} \right|_{r=R} = 4\pi R D c_0 \left(1 - \varphi \coth \varphi \right), \tag{8.20}$$

where $\varphi = R\sqrt{k''A_g/D}$ is the Thiele modulus. We can estimate the ideal flux as the maximum oxygen consumed if the (catalytical) surface were completely exposed to the reaction:

$$W_0 = \frac{4\pi R^3}{3} k'' A_g c_0. \tag{8.21}$$

We find the effectiveness factor ([8]):

$$\eta = \frac{W_R}{W_0} = \frac{3}{\varphi^2}(\varphi \coth \varphi - 1). \tag{8.22}$$

Analogously to flat particle case we approximate the reaction rate k'' by $\tilde{k}_c \exp(-E/(RT))$. The values of the frequency factor k_c, specific surface area A and particle radius R are given in Table 8.3. The temperature T and the diffusion coefficient D are considered to be constant in the ranges $700 \le T \le 1300$ and $10^{-14} \le D \le 10^{-8}$. Typical values for coal are $D = 10^{-11} \, [m^2/s]$, see [41] and $T < 1100 \, [K]$, see [8]. The corresponding effectiveness factors are close to 1 as presented in Table 8.2.

8.5 Activation energy and frequency factor

Finally, the quantity most interesting to us is the **observed (true) reaction rate**, which represents the quantity of carbon consumed by the reaction per current carbon concentration

Table 8.2: Effectiveness factor for the spherical particles of petroleum coke for different temperatures and diffusion coefficients. Data from Table 8.3 for [44]

$D \setminus T$	700^0C	900^0C	1100^0C	1300^0C
10^{-8}	1.0000	1.0000	1.0000	1.0000
10^{-10}	1.0000	1.0000	0.9999	0.9999
10^{-12}	1.0000	0.9999	0.9898	0.8364
10^{-14}	1.0000	0.9870	0.5679	0.1586

per time unit, denoted by $R_c\,[1/s]$. The definition of the observed reaction rate varies from text to text. For example in [22, 44] it is defined as the consumption rate of carbon mass per unit time per external surface area of the particle. On the other side in [39] it is defined per particle volume instead of per surface area.

The observed reaction rate depends on all particle properties explained above, thus in [44] the concept of **intrinsic reaction rate (reactivity)** is introduced. It is the reaction rate that occurs if all the carbon containing molecules inside the particle were to contact the oxygen at total concentration. The intrinsic reaction rate, indicated by R_i, is defined in terms of carbon mass per catalytical surface area per unit time:

$$R_i = \tilde{k}_c \exp\left(\frac{-E}{RT}\right) \quad [\frac{kg}{m^2s}]. \tag{8.23}$$

The probability that after collision of molecules the reaction occurs is given by Arrhenius' law, which contains the **activation energy** in the exponential. The activation energy is indicated by $E\,[J/mole]$ and it is the energy necessary to "start" the reaction.

Following [22, 44], the intrinsic reaction rate is similar for combustion of any material containing carbon (e.g: coal, graphite, diamond). In this text we use the intrinsic reaction rates originating from several experiments, [43, 44, 49, 39].

Specimens of carbon produced from different original materials, or in different ways from the same material, are found to burn at very different rates under otherwise similar conditions. The speed at which an individual carbon particle of given size or mass burns depends on the rate of oxygen transfer from the bulk gas to the particle, and on the particle reactivity. This reactivity depends on (i) the extent and accessibility to oxygen of the pores within the particle, and on (ii) the rate of chemical reaction between oxygen and the pore surface. The latter factor, when properly defined, may be termed the intrinsic reactivity of carbon. In this section we

Table 8.3: Translating intrinsic reactivity coefficient into nondimensional reaction rate.

Source	$2R\,[m]$	$\sigma_a\,[\frac{kg}{m^3}]$	$A_g\,[\frac{m^2}{kg}]$	$\tilde{k}_c\,[\frac{kg}{m^2 s}]$	$E_A\,[\frac{J}{mole}]$	η	m	C_g^{ini}	$\eta_f^{res}\,[\frac{kg}{m^3}]$	$k_c\,[\frac{10^6}{s}]$
[2]	-	1950	7050	1.44	73500	1	1	1.0	20	0.0102
[43]	$6.7\cdot10^{-5}$	1730	-	200	76150	1	1	0.20	17	-
[44]	$1.3\cdot10^{-5}$	-	1000	3050	179400	1	1	0.20	-	3.05
[49]	$2.9\cdot10^{-3}$	1640	900	2216.7	167000	1	0.59	0.21	-	1.995
[49]	$9\cdot10^{-4}$	1660	1000	2216.7	159000	1	0.6	0.21	-	2.217
[49]	$2.2\cdot10^{-4}$	-	1600	2216.7	159000	1	0.59	0.21	-	3.547

summarize the results for intrinsic reactivity from different sources.

- In [44], based on the analysis of 33 different experiments from 23 papers it was shown that the intrinsic reactivity of carbon R_i obeys the Arrhenius' law with some average activation energy $E = 43[kcal/mole] \approx 179.4[kJ/mole]$ and the corresponding frequency factor was $\tilde{k}_c = 3050\,[kg/m^2/s]$. The activation energies were spread through the interval of $30 - 70[kcal/mole]$. These results were explained theoretically in [22].

- Some work investigating ISC, for example [2, 46], use an activation energy of $17[kcal/mole]$, however there are few volatile mixtures of coal that possess such a small activation energy.

- The values for frequency factor and activation energy in [44] were obtained by analyzing the slope and displacement of the linear approximation for the intrinsic reactivity data plotted as $\log(R_i)$ against $10^4/T$. This method can generate many errors in the parameters of our interest; the data for petroleum coke is parallel but at some distance from the linear approximation obtained using the least squares method onto all other carbon data. We took only the data for petroleum coke and using the least squares method obtained the frequency factor $\tilde{k}_c = 12100\,[kg/m^2 s]$ and activation energy $E = 159.5\,[kJ/mole]$. The standard deviation for the activation energy was $R^2 = 0.98$. We note that the expectation of k_c, $E(k_c)$, is larger than $\exp(E(ln(k_c)))$. In view of the small variance of the petroleum coke data we neglect this effect.

- In [49], the intrinsic reactivity of petroleum coke was studied and the parameter values were $\tilde{k}_c = 2216.7\,[kg/m^2 s]$ and $E_A = 158.6[kJ/mole]$.

We summarize the results in Table 8.3.

Remark 8.2 *In [39, 43, 49] the experiments were made with petroleum coke provided by a commercial aluminium producer and prepared by the CSIRO (Australian Commonwealth Sci-*

entific and Research Organization) Division of Fossil and Fuels, the results were compared with other experiments and the data for coke looks well defined.

8.6   The balance law equation

Now we are able to formulate the combustion rate of solid fuel R_S in terms of molar mass of fuel per cubic meter of porous media:

$$R_S = \eta A_g \tilde{k}_c \rho_m \left(\frac{P_{O_2}}{P_{atm}} \right)^m \exp\left(\frac{-E}{RT} \right) \quad [\frac{mole}{m^3 \, s}], \tag{8.24}$$

where $\rho_m \, [mole/m^3]$ is **molar density** of fuel in porous media. We define the dimensionless oxygen concentration $C_g = P_{O_2}/P_{atm}$ and scale it as $C_g = Y C_g^{ini}$, where C_g^{ini} is the initial dimensionless concentration of oxygen.

We need the reaction rate in terms of *moles of fuel per cubic meters of porous medium per second*. First, we define the "dimensionless" reaction rate coefficient:

$$k_c = \eta A_g (C_g^{ini})^m \tilde{k}_c \, [1/s], \tag{8.25}$$

and formulate the balance equation in terms of molar mass:

$$\frac{\partial \rho_m}{\partial t} = -k_c \rho_m Y^m \exp\left(-E/RT \right) \quad [\frac{mole}{m^3 s}]. \tag{8.26}$$

In order to nondimensionalize (8.26) we follow [2] and define the dimensionless value for specific molar density η in such way that $\eta = 1 - \rho_m/\rho_m^0$, where ρ_m^0 is the initial fuel concentration in the porous medium. We rewrite (8.26) as:

$$\frac{\partial \eta}{\partial t} = k_c (1 - \eta) Y^m \exp\left(-E/RT \right) \quad [s^{-1}]. \tag{8.27}$$

If we follow [2] and consider $m = 1$, the equation (8.27) coincides with (2.4):

$$\frac{\partial \eta}{\partial t} = k_c (1 - \eta) Y \exp\left(-E/RT \right) \quad [s^{-1}]. \tag{8.28}$$

We summarize the relevant constants in Table 8.3.

Remark 8.3 *In Table 2.1 we give the initial fuel concentration as $\rho_f^0 = 19.2182 \, [kg/m^3]$ in order to obtain ρ_m^0 we use the effective molecular weight of coke M_f from Table 2.1 and obtain $\rho_m^0 = \rho_f^0 \cdot (M_f)^{-1} \approx 4.51 \, [mole/m^3]$.*

Bibliography

[1] S.A. Abu-Khamsin, E. Brigham, and H.J. Ramey, Jr. Reaction kinetics of fuel formation for in-situ combustion. *SPE Reservoir Engeneering*, SPE 15736-PA, 1988.

[2] I.Y. Akkutlu and Y.C. Yortsos. The dynamics of in-situ combustion fronts in porous media. *J. of Combustion and Flame*, 134:229–247, 2003.

[3] I.Y. Akkutlu and Y.C. Yortsos. Steady-state propagation of in-situ combustion fronts with sequential reactions. *SPE International Petroleum Conference in Mexico, Puebla, Mexico*, 2004. SPE 91957.

[4] A.P. Aldushin, I.E. Rumanov, and B.J Matkowsky. Maximal energy accumulation in a superadiabatic filtration combustion wave. *J. of Combustion and Flame*, 118:76–90, 1999.

[5] H.R. Baily and B.K. Larkin. Conduction-convection in underground combustion. *Petroleum Trans. AIME*, 217:321–331, 1960.

[6] S. Balasuriya, G.A. Gottwald, J. Hornibrook, and S. Lafortune. High Lewis number combustion wavefronts: a perturbative melnikov analysis. *SIAM J. on App. Math.*, 67(2):464–486, 2007.

[7] A.L. Benham and F.H. Poettmann. The thermal recovery process – an analysis of laboratory combustion data. *Petroleum Trans. AIME*, 213:406–408, 1958.

[8] R.B. Bird, W.E. Stewart, and E.N. Lightfoot. *Transport Phenomena*. Wiley, New York, 2nd edition, 2002.

[9] T.C. Boberg. *Thermal Methods of Oil Recovery*. An Exxon Monograph Series, 1988.

[10] I.S. Bousaid and H.J. Ramey Jr. Oxidation of crude oil in porous media. *SPE Journal*, pages 137–148, June 1968. SPE 1937.

[11] J. Bruining, A.A. Mailybaev, and D. Marchesin. Filtration combustion in wet porous medium. in preparation, 2009.

[12] J. Bruining, A.A. Mailybaev, and D. Marchesin. Filtration combustion with pyrolysis in porous medium. in preparation, 2009.

[13] E. Brunauer and PH Emmett. Teller. *J. Am. Chem. Soc*, 60:309, 1938.

[14] G. Chapiro. Singular perturbation applied to combustion waves in porous media (in portuguese). Master's thesis, IMPA, 2005.

[15] G. Chapiro, J. Bruining, and D. Marchesin. Chemistry of coke combustion transmuted into mathematics. in preparation, 2009.

[16] G. Chapiro, G. Hime, A. A. Mailybaev, D. Marchesin, and A.J. Souza. Global asymptotic effects of the structure of combustion waves in porous media. In *To appear in the proceedings of 12th International Conference on Hyperbolic Problems: Theory, Numerics, Applications*, 2009. College Park, USA.

[17] G. Chapiro, G. Hime, and D. Marchesin. Numerical simulation of combustion waves in porous media. In *Proceedings of XXIX CILAMCE*, November, 4-7, 2008. Maceió, Brasil.

[18] G. Chapiro, A. A. Mailybaev, D. Marchesin, and A.J. Souza. Long time asymptotic solution for forward filtration combustion. In preparation, 2009.

[19] G. Chapiro, A. A. Mailybaev, D. Marchesin, and A.J. Souza. Singular perturbation in combustion waves for gaseous flow in porous media. In *Proceedings of XXVI CILAMCE*, October, 19-21, 2005. Guarapari, Brasil.

[20] G. Chapiro and D. Marchesin. Non-diffusive combustion waves in insulated porous media. *BJPG*, 2(2):18–28, 2008.

[21] G. Chapiro, D. Marchesin, and A.J. Souza. Asymptotic expansions for combustion fronts in porous media. In *Proceedings of CMNE/CILAMCE*, June, 13-15, 2007. Porto, Portugal.

[22] H.R. Essenhigh. *Fundamentals of Coal Combustion, as chapter in "Chemistry of Coal Utilization", Secondary supplementary volume*. Willey-Interscience publication, New York, 1981.

[23] N. Fénichel. Geometric singular perturbation theory for ordinary differential equations. *Journal of Differential Equations*, 31:53–98, 1979.

[24] C.F. Gates and H.J. Ramey Jr. Field Results of South Belridge Thermal Recovery Experiment. *Petroleum Transactions, AIME*, 213:236–244, 1958. SPE 1179-G.

[25] A. Ghazaryan, Y. Latushkin, S. Schecter, and A. J. Souza. Stability of gasless combustion fronts in one-dimensional solids. *Submitted to Archive for Rational Mechanics and Analysis*, 2009.

[26] G.H. Golub and C.F. Van Loan. *Matrix computations*. Johns Hopkins University Press, 1996.

[27] B. He, Q. Chen, L.M. Castanier, and A.R. Kovscek. Improved in-situ combustion performance with metallic salt additives. *SPE Western Regional Meeting*, 2005. SPE 93901-MS.

[28] G. Hime. Parallel solution of nonlinear balance systems. Master's thesis, LNCC. Brazil, 2007.

[29] G Hime and D Marchesin. Nitro: a parallel solver of nonlinear balance systems. Technical report, IMPA, 2009.

[30] S. Johnson, R. *Singular Perturbation Theory, mathematical analytical techniques with applications to engineering*. Springer, New York, 2005.

[31] C.K.R.T. Jones. Geometric singular perturbation theory in dynamical systems. *Lecture Notes in Math., Springer, Berlin*, 1609:44–118, 1995.

[32] M. Kumar and A.M. Garon. An experimental investigation of the fireflooding combustion zone. *Soc. Pet. Eng. Res. Eng.*, 6(1):55–61, 1991.

[33] Morton K.W. and Mayers D.F. *Numerical Solutions of Partial Differential Equations*. Cambridge University Press, 2nd edition, 2005.

[34] Mitchell S. L., Morton K. W., and Spence A. Analysis of box schemes for reactive flow problems. *SIAM Journal on Scientific Computing*, 27(4):1202–1225, 2006.

[35] O. Levenspiel. *Chemical reaction engineering*. Wiley, New York, 3rd edition, 1999.

[36] A. D. McNaught and A. Wilkinson. *online version of the IUPAC Compendium of Chemical Terminology.* Royal Society of Chemistry, Cambridge, UK, 2nd edition, 1997.

[37] M. Prats. *Thermal Recovery.* SPE of AIME, 1982.

[38] W.H. Press at al. *Numerical recipes in C: the art of scientific computing.* Cambridge University Press, 1992.

[39] W. Rybak. Intrinsic reactivity of petroleum coke under ignition conditions. *Fuel*, 67, 1988.

[40] D. A. Schult, A. Bayliss, and B. J. Matkowsky. Traveling waves in natural counterflow filtration combustion and their stability. *SIAM J. Appl. Math*, 58(3):806–852, 1998.

[41] N. Siemons, K.H.A.A. Wolf, and J. Bruining. Interpretation of carbon dioxide diffusion behavior in coals. *International Journal of Coal Geology*, 72(3-4):315–324, 2007.

[42] J. D. M. Silva. Esquemas numéricos para filtração em meios porosos (in portuguese). Master's thesis, IMPA, 2007.

[43] I.W. Smith. Kinetics of combustion of size-graded pulverized fuels in the temperature range 1200-2270 k. *Combustion and Flame*, 17:303–314, 1971.

[44] I.W. Smith. The intrinsic reactivity of carbons to oxygen. *Fuel*, 57(7):409–414, 1978.

[45] J. Sotomayor. *Lições de equações diferenciais ordinárias.* IMPA, Rio de Janeiro, Brasil, 1979.

[46] A. J. Souza, D. Marchesin, and I. Y. Akkutlu. Wave sequences for solid fuel adiabatic in-situ combustion in porous media. *Comp. Appl. Math*, 25(1):27–54, 2006.

[47] C. Strikwerda, J. *Finite Difference Schemes and Partial Differencial Equations.* Wadsworth & Brooks, 1989.

[48] E.M. Tavera. Analytical expression for the non-isothermal effectiveness factor: the nth-order reaction in a slab geometry. *Chemical Engineering Science*, 60:907–916, 2005.

[49] R.J. Tyler. Intrinsic activity of petroleum coke to oxygen. *Fuel*, 65:235, 1986.

[50] W.R. Wasow. *Asymptotic expansions for ordinary differential equations.* Dover, 1987.